Universidad de Alcalá

PROGRAMA DE DOCTORADO EN TECNOLOGÍAS DE LA INFORMACIÓN Y COMUNICACIONES

Aeroelastic Wing Flutter Testing and Analysis

Tesis Doctoral presentada por:
Sami ABOU-KEBEH LLANO

Directores:
Dr. Roberto GIL PITA
Dr. Manuel ROSA ZURERA

Escuela Politécnica Superior
Departmento de Teoría de la Señal y Comunicaciones

Alcalá de Henares
9 de Junio de 2022

"Si sigues aumentando la velocidad siempre acabas llegando a flutter. El problema aparece si tu avión te permite alcanzar esa velocidad."

Carlos Maderuelo.

Abstract

The integration of new underwing stores in an aircraft modifies the characteristics of mass distribution (center of gravity) and moment of inertia of the wing. This effect, in addition to to the contribution of aerodynamic loads, causes the vibration modes and frequencies to vary with the dynamic pressure (a function of flight speed and altitude). This strongly non-linear phenomenon implies that, under certain conditions of dynamic pressure, the coupling in frequency (self-sustaining resonance) of two or more modes of vibration initially orthogonal to each other occurs, an aeroelastic phenomenon known as "flutter", which will lead to the loss of the aircraft and the life of the pilot unless the flight conditions change. Thus, the integration of new underwing stores requires carrying out a series of processes that will lead to a new flight envelope, within which it is guaranteed that the aircraft can fly safely. This study requires carrying out theoretical calculations to predict flutter conditions and subsequent validation through flight tests, known as "envelope expansion". Carrying out this task safely requires highly qualified and specialized means and personnel, and this implies extraordinarily high costs, which leads to companies specialized in carrying out these tests to guarding data and results as an industrial secret, and among other things it is very difficult to find validated methods to process flight data and extract vibration parameters at different dynamic pressures.

Among the different published methods to identify flutter test flight vibration parameters, the vast majority have been verified only with theoretical models, with the fact that many of them give results that are inconsistent with each other or, when validated with real data, yield inconsistent results. For this reason, the main objective was to develop fast, robust and coherent techniques, capable of returning repetitive and consistent results in real time. The author had access to a flutter flight test database, courtesy of the Spanish Air Force, and has authorization from the Air Force Communications Office to use and publish results derived from his research on those data.

This thesis will present a research dedicated to developing two data processing methods for flutter flight tests, in particular on data from a "Sine-Dwell" type excitation, one based on a mathematical model and optimization techniques, and another based on deep learning techniques. The development of both techniques, is based on a first verification of different techniques documented in the bibliography by different authors, as well as on the training of different neural networks; Multilayer perceptrons, deep neural networks and convolutional neural networks. Once a comparison baseline was available, a classical technique was selected (based on a theoretical model and optimization), according to the bibliographic source validated with real data from flutter flight tests, and one of the trained neural networks. Based on the lessons learned, an innovative technique was developed based on the classical model of theoretical model and optimization, verification with synthetic data and comparison of the three previously selected techniques. Finally, the three techniques were validated with real data from flutter flight tests.

The results obtained are highly satisfactory, reaching the initially planned objectives. The techniques presented have been verified with synthetic data, compared with previously independently validated bibliographic models and validated in this study with real data. The results are consistent with expectations. The speed of the process allows the analysis of data in real time, increases the situational awareness of the test director and facilitates decision-making to continue or stop the test, in dangerous conditions, with greater safety.

Resumen

La integración de nuevas cargas subalares en una aeronave modifica las características de distribución de masa (centro de gravedad) y momento de inercia del ala. Este efecto, sumado a la contribución de las cargas aerodinámicas, produce que los modos y frecuencias propias de vibración varíen con la presión dinámica (función de la velocidad de vuelo y altitud). Este fenómeno fuertemente no lineal implica que, bajo determinadas condiciones de presión dinámica, se produzca el acoplamiento en frecuencia (resonancia autosostenida) de dos o más modos de vibración inicialmente ortogonales entre sí. El fenómeno aeroelástico anterior se conoce como "flameo" ("flutter" en inglés), que salvo cambio de las condiciones de vuelo, llevará a la pérdida de la aeronave y la vida del piloto. Por otra parte, la integración de nuevas cargas subalares requiere llevar a cabo una serie de procesos que conducirán a una nueva envolvente de vuelo, dentro de la cual se garantice que la aeronave puede volar con seguridad. Este estudio requiere llevar a cabo cálculos teóricos para predecir las condiciones de flameo y una posterior validación mediante ensayos en vuelo, conocido como "expandir la envolvente". Ejecutar esta tarea con seguridad requiere unos medios y personal altamente cualificados y especializado, cuyos costes derivados son extraordinariamente elevados. Como consecuencia, las empresas especializadas llevan a cabo estos ensayos y guardan los resultados como secreto industrial. Todo lo anterior justifica que sea muy complicado encontrar métodos validados para procesar datos de vuelos y extraer los parámetros de vibración a distintas presiones dinámicas.

Entre los distintos métodos publicados para identificar parámetros de vibración de vuelos de ensayos de flameo, la gran mayoría han sido verificados únicamente con modelos teóricos, dándose el caso de que muchos de ellos dan resultados incongruentes entre sí o que al ser validados con datos reales arrojan resultados incoherentes. Por este motivo, el objetivo principal era desarrollar técnicas robustas, coherentes y repetitivas para procesar datos de vuelo de flameo. El autor del presente estudio ha tenido acceso a una base de datos de ensayos en vuelo de flameo, cortesía del Ejército del Aire de España, y cuenta con autorización de la Oficina de Comunicaciones del Ejército del Aire para publicar resultados de su investigación sobre esos datos.

La presente tesis desarrolla dos métodos de procesado de datos de ensayos en vuelo de flameo específicos sobre datos procedentes de una excitación tipo "Sine-Dwell". El primero está basado en un modelo matemático y en técnicas de optimización. El segundo en técnicas de aprendizaje profundo. El desarrollo de ambas técnicas se inicia con una primera verificación de distintas técnicas documentadas en la literatura científica, seguidos por el entrenamiento de las siguientes redes neuronales; De perceptrón multicapa, redes neuronales profundas y redes neuronales convolucionales. Establecida una línea de base de comparación, se procedió a seleccionar una técnica clásica (basada en modelo teórico y optimización), de acuerdo con la fuente bibliográfica, validada con datos reales procedentes de ensayos en vuelo de flameo y una de las redes neuronales entrenadas. Partiendo de las lecciones aprendidas se desarrolló una técnica innovadora basada en el modelo clásico de modelo teórico y optimización, verificación con datos sintéticos y comparación de las tres técnicas seleccionadas anteriormente. Finalmente, las tres técnicas fueron validadas con datos reales de ensayos en vuelo de flameo.

Los resultados obtenidos son altamente satisfactorios, alcanzando los objetivos previstos inicialmente. Las técnicas presentadas se han verificado con datos sintéticos, comparadas con modelos bibliográficos previamente validados de forma independiente, y validadas en este estudio con datos reales. Los resultados son coherentes con lo esperado. La velocidad de proceso permite el análisis de los datos en tiempo real, aumentan la consciencia situacional del director de ensayos y facilitan la toma de decisiones para continuar o detener el test, en condiciones de peligro, con mayor seguridad.

Acknowledgements

In 2009 I was selected to follow a Flight Test Engineering Master in USAF Test Pilot School. To me (and probably anyone who attended since its creation) it was an unique opportunity, and totally changed my career and also my life. After returning to the Spanish Air Force I was assigned to CLAEX, and TCol. Carazo assigned me to the Stores Integration team, where I learned from Col. Alonso, my mentor, most of the things I know today to be able to properly integrate stores in an aircraft and expand its Flight Envelope.

My motivation to complete this PhD was due to the fact that I wanted to fulfil my duty in the best possible way. I started a Master in what I thought I could contribute most to the team, Technologies of the Information and Communication with specialization in Digital Data Processing, and due to the great interest it awoke on me, I decided to continue and specialize following a PhD.

During the development of this Thesis the contribution of my tutors, Dr. Manuel Rosa Zurera and Dr. Roberto Gil Pita, was utterly and undoubtedly crucial. Dr. Rosa provided me with an insight on how to orient the paper and the investigation, while the contribution of Dr. Gil was paramount to reach a successful solution to the problem described in this Thesis. His contribution to unlock a gordian knot, related to the importance of the phase angle in the equations, was the key to solve a five years stagnation point in the investigation. His support, help and deep knowledge on math, signal processing and programming (for the topics I know of) are virtually light years away from what I could ever reach.

My wife Luz and my children Iria and Leo shared my frustration, gave me their time and stubbornly gave me a support that demanded quite a share of their patience and generosity. Luz always knew it was an important stage in my life, and pulled from me when I needed most and was about to give up. It is absolutely fair to say that without her on my side these lines would never have seen light.

Last but not least, my parents Carmen and Sami. This Thesis constitutes the highest (although not the last) stage of my education. They blindly supported me even in the hardest times and never gave up on me. They were on my side when I needed them most, sacrificed their own happiness to provide my sister Layla and I a loving family, a future and made the hardest effort to support our education.

With this Thesis I hope to provide some useful information to make Envelope Expansion Tests a little safer for the stores integration community...

Contents

Abstract **ii**

Resumen **iii**

Acknowledgements **iv**

1 Introduction, State of the Art and Scope of the thesis **1**
1.1 Introduction . . . 1
1.2 Concept of Aeroelasticity . . . 1
1.2.1 Concept of Flutter . . . 3
1.2.2 Flight Envelope . . . 7
1.2.3 Flutter and Envelope Expansion Testing paradigm . . . 7
1.3 State of the Art . . . 13
1.3.1 Aeroelastic equations documentary basis . . . 13
1.3.2 Flutter Data Processing Documentary Basis . . . 14
1.4 Objective, Scope and Limitations . . . 15
1.5 Description of the Problem . . . 15
1.6 Work Hypotheses and assumptions . . . 16
1.7 Methodology of Investigation . . . 16

2 Materials and Methods **18**
2.1 Introduction to the flutter mechanism . . . 19
2.2 First term: Inertial forces . . . 20
2.3 Second term: Dissipative forces (damping) . . . 21
2.3.1 Undamped vibrations . . . 21
2.3.1.1 Modal shapes . . . 22
2.3.2 Damping and damped vibrations . . . 22
2.3.2.1 Proportional damping . . . 23
2.3.2.2 Viscous damping . . . 26
2.4 Third term: Elastic forces . . . 28
2.5 Fourth term: Aerodynamic forces . . . 28
2.5.1 Steady Aerodynamics . . . 29
2.5.1.1 Euler reference system . . . 30
2.5.1.2 Substantial derivative . . . 30
2.5.1.3 General equations . . . 30
2.5.1.4 Velocity potential . . . 31
2.5.1.5 Stream function . . . 32
2.5.1.6 Relationship between Φ and Ψ. Complex potential . . . 32
2.5.1.7 Euler-Bernouilli's equation . . . 35
2.5.1.8 Lift and non-dimensional coefficients. Kutta - Joukowski Theorem . . . 35
2.5.1.9 Kutta condition . . . 37
2.5.1.10 Thin airfoil theory . . . 38
2.5.2 Unsteady Aerodynamics . . . 43

2.5.2.1 Description of the procedure . . . 43
2.6 Flutter on an Airfoil . . . 49
2.7 Flutter signal particularities . . . 50
2.7.1 Wing Flutter Signals . . . 50
2.7.2 Frequency resolution . . . 51
2.7.3 High damping and relationship with short duration . . . 52

3 Investigation **56**
3.1 Introduction to this chapter . . . 56
3.2 Phase angle and bandwidth in linear second order ordinary differential equations . . . 57
3.2.1 Relationship between the phase angle and the damping ratio . . . 57
3.2.2 Relationship of the bandwidth B with the phase angle φ . . . 60
3.2.3 Conclusions of the phase angle impact on the signals identification . . . 62
3.3 Data processing techniques description . . . 62
3.3.1 Basic processing techniques . . . 62
3.3.1.1 Time Processing algorithm . . . 63
3.3.1.2 Complex Spectrum algorithm . . . 64
3.3.1.3 Power Spectrum algorithm . . . 64
3.3.2 Peak-Amplitude algorithm . . . 64
3.3.3 Matrix Pencil algorithm . . . 65
3.3.4 Laplace Wavelet Matching Pursuit algorithm . . . 65
3.3.5 Deep Learning based estimation . . . 66
3.3.5.1 Multi-Layer perceptrons . . . 66
3.3.5.2 Deep Neural Networks . . . 67
3.3.5.3 Convolutional Neural Networks . . . 67
3.4 Verification and comparison of the classical techniques with synthetic data . . . 69
3.5 Proposed Data Processing algorithm. PRESTO algorithm . . . 74
3.5.1 PRESTO vs. Laplace Wavelet Matching Pursuit . . . 75
3.6 Verification of the PRESTO algorithm with synthetic data and comparison with Laplace Wavelet Matching Pursuit . . . 76
3.7 Verification and comparison of the Deep Learning techniques with synthetic data . . . 77
3.7.1 Design data and feature extraction . . . 77
3.7.2 Multi-layer perceptron training process and results . . . 79
3.7.3 Deep Neural Network training process and results . . . 80
3.7.4 Convolutional Neural Network training process and results . . . 83
3.8 Comparison of synthetic data analysis results and performance between PRESTO, Laplace Wavelet and Deep Learning techniques . . . 87
3.9 Experimental results . . . 89
3.9.1 Data acquisition . . . 90
3.9.2 Analysis of results . . . 92

4 Conclusions and future lines of work **98**
4.1 Conclusions of the results . . . 98
4.2 Conclusions . . . 100
4.3 Future lines of work . . . 100
4.4 List of publications . . . 102

A Generic demonstrations **104**
A.1 Demonstration of the aerodynamic velocity potential . . . 104
A.2 Calculation of pressure coefficient terms in unsteady aerodynamics from the velocity potential and thermodynamic relationships . . . 105

A.3 Velocity of sound demonstration 106
A.4 Calculation of the circulation of the vortices sheet under unsteady aerodynamics . . 107
A.5 Calculation of the unsteady pressure coefficient 110
A.6 Demonstration of the case $\omega_0 = 0$ in equation 3.11 111

Bibliography **113**

List of Figures

1.1 Collar's triangle . . . 2
1.2 Physical depiction of an airfoil under flutter coupling. There is a 90° offset between torsion and bending motions. . . . 3
1.3 Typical V-G plot. Original plot extracted from Tian et al., 2016 and modified to match similar parameters to our case. Damping vs. Airspeed plot . . . 4
1.4 Typical V-G plot. Original plot extracted from Tian et al., 2016 and modified to match similar parameters to our case. Frequency vs. Airspeed plot . . . 5
1.5 First vertical bending mode . . . 6
1.6 First torsion mode . . . 6
1.7 Flight envelope example. Straight lines indicate constant dynamic pressure curves q, while dashed lines represent constant airspeed. Image extracted from the USAF TPS Master of Science notes. Subject "Envelope Expansion Tests" . . . 8
1.8 Flutter Flight Testing paradigm. . . . 10
1.9 Risk Matrix. Extracted from MIL-STD-882E, 2012 . . . 13

2.1 Comparison between the viscous damping force and structural damping force maximum amplitude. Extracted from García-fogeda and Arévalo-Lozano, 2015 . . . 25
2.2 Velocity circulation around a closed curve . . . 32
2.3 Streamlines around an airfoil . . . 33
2.4 Different potential flows examples. Upper left a sink example of intensity Q. Upper right a vortex example of intensity Γ. Lower left an example of uniform flow with velocity u_∞. Lower right an example of source with intensity Q . . . 33
2.5 Vortex sheet . . . 34
2.6 Airfoil definitions. The camber is defined as the distance between the mean chamber line and the chord, the mean camber line c is the line which separates equally the upper side of the airfoil and the lower side of the airfoil, depicted in blue, the chord is the straight line that joins the the leading edge and the trailing edge, depicted as a red line. The undisturbed airflow speed is u_∞, the angle of attack is the angle between the chord and the airflow airspeed vector. Dimension ζ along the chord indicates the distance from the leading edge to the chord element $d\zeta$ . . . 36
2.7 Airfoil camber mean line defined by a vortex and doublets distributed over the curve 37
2.8 Trailing edge ending with a finite angle . . . 38
2.9 Trailing edge ending in cusp . . . 38
2.10 Thin airfoil theory nomenclature . . . 39
2.11 Symmetric airfoil sample . . . 40
2.12 Cambered airfoil sample . . . 41
2.13 Control volume excluding wake. The figure represents in red the vortex sheet and in green the Karman Vortex street into the wake. . . . 45
2.14 Airfoil definitions . . . 46
2.15 Sample data. Sine Dwells . . . 51
2.16 Comparison of different versions of the same signal with different levels of noise and its power spectrum. Low damping. . . . 53

2.17 Comparison of different versions of the same signal with different levels of noise and its power spectrum. High noise and low damping. 54

3.1 Relative resonant frequency ($\gamma = \omega_0/\omega_n$) of a single underdamped mode, with respect to the damping factor (ζ) for different phase values (φ). 60
3.2 Relative bandwidth (B/ω_n) of a single underdamped mode, with respect to the damping factor (ζ) for different phase values (φ). 61
3.3 Data processing algorithm applicable to three different processing techniques, Time Series fitting, Complex Spectrum fitting and Power Spectrum fitting 63
3.4 Multi Layer Perceptron sample network. In this case the MLP with 20 neurons is depicted. 67
3.5 Deep Neural Network sample. In this case a DNN with one input layer, three hidden layers and one output layer is depicted. In this case each hidden layer has 40 neurons 68
3.6 Convolutional Neural Network sample. In this case a CNN with one input layer, two convolutional layers, one connection layer and one regression layer is depicted. Each convolutional network has a different number of neurons in their convolutional layers (in each convolutional process) and a different number of convolutional processes. 68
3.7 Plot depicting the estimated natural frequency average relative error in percentage. The data were produced with a SNR of 5dB removing the worst 10% estimations. . . 71
3.8 Plot depicting the estimated damping factor root mean square error (RMSE) in logarithmic scale. The data were produced with a SNR of 5dB removing the worst 10% estimations. 72
3.9 PRESTO block diagram 74
3.10 Plot depicting the estimated natural frequency average relative error in percentage and the Root Mean Square Error (RMSE), comparing the Laplace Wavelet and the PRESTO techniques. The data were produced with a SNR of 5dB removing the worst 10% estimations. 76
3.11 Plot depicting the estimated natural frequency average relative error in percentage [%] and the Root Mean Square Error (RMSE) in absolute value, comparing MLP networks composed of different number of neurons. The secondary "y" axis plots the execution time required for each network in [ms]. The networks were trained with 0dB, 5dB and 10dB SNR data, removing the worst 10% estimations on the validation dataset. 80
3.12 Plot depicting the estimated natural frequency average relative error in percentage [%] and the Root Mean Square Error (RMSE) in absolute value, comparing DNN networks with 2 layers and composed of different number of neurons on each layer. The secondary "y" axis plots the execution time required for each network in [ms]. The networks were trained with 0dB, 5dB and 10dB SNR data, removing the worst 10% estimations on the validation dataset. 82
3.13 Plot depicting the estimated natural frequency average relative error in percentage [%] and the Root Mean Square Error (RMSE) in absolute value, comparing DNN networks with 3 layers and composed of different number of neurons on each layer. The secondary "y" axis plots the execution time required for each network in [ms]. The networks were trained with 0dB, 5dB and 10dB SNR data, removing the worst 10% estimations on the validation data. 83
3.14 Construction of the data matrix to feed the CNN. Once the time series dataset is transformed into a frequency spectrum (real and imaginary parts), each dataset of the CNN feed matrix will distribute the frequencies in columns and the projection of each frequency value on different determined vectors in rows. 84

3.15 Plot depicting the estimated natural frequency average relative error in percentage [%] and the Root Mean Square Error (RMSE) in absolute value, comparing CNN networks with 5 layers and composed of different number of neurons on each layer. The secondary "y" axis plots the execution time required for each network in [ms]. The networks were trained with 0dB, 5dB and 10dB SNR data, removing the worst 10% estimations on the validation data. 86
3.16 Plot depicting the estimated natural frequency average relative error in percentage [%] and the Root Mean Square Error (RMSE) in absolute value, comparing CNN networks with 6 layers and composed of different number of neurons on each layer. The secondary "y" axis plots the execution time required for each network in [ms]. The networks were trained with 0dB, 5dB and 10dB SNR data, removing the worst 10% estimations on the validation data. 87
3.17 Plot depicting the estimated natural frequency average relative error in percentage [%] and the Root Mean Square Error (RMSE) in absolute value, comparing Laplace Wavelet, PRESTO and a 6x(40) CNN network. The data compared was generated synthetically by known parameters (10.000 datasets), in the case of the CNN the validation dataset (20.000 datasets) with a SNR of 5dB. In all three cases the 10% worse estimations were removed. 89
3.18 Disposition of extensometers in the Spanish Air Force F-18A/B employed to perform flutter tests 91
3.19 Data plot between real and synthetic data processed by Laplace Wavelet Matching Pursuit, PRESTO and a Convolutional Neural Network of 6 hidden layers and 40 neurons per layer. The 150 best matching signals out of a complete dataset of 640 were employed. The red line represents the linear regression of the dataplots. 93
3.20 Mean Absolute Error (MAE) plot between the PRESTO and Laplace Wavelet Matching Pursuit analyzed data. 640 signals were employed to get the error plot. 94
3.21 Average Frequency Spectrum of real data. The first figure shows the frequency spectrum of all the original datasets, the second shows the histogram of frequencies estimated by PRESTO on the original datasets. The third shows the histogram of the dampings estimated by PRESTO on the original datasets. 95
3.22 Average Frequency Spectrum of real data. The first figure shows the frequency spectrum of all the original datasets, the second shows the histogram of frequencies estimated by the Laplace Wavelet on the original datasets. The third shows the histogram of the dampings estimated by the Laplace Wavelet on the original datasets. 95
3.23 Average Frequency Spectrum of real data. The first figure shows the frequency spectrum of all the original datasets, the second shows the histogram of frequencies estimated by a CNN 6x(40) on the original datasets. The third shows the histogram of the dampings estimated by a CNN 6x(40) on the original datasets. 96

A.1 Sign convention and nomenclature 104
A.2 Velocity circulation around a closed curve. Figure 2.2 reproduced here for clarity. . . 105
A.3 Control volume including a static pressure wave. Note that the control volume is moving with the pressure wave to prevent dependency on time. 107

List of Tables

2.1 Summary of signals comparison results 55

3.1 Results of running different estimation algorithms over synthetic datasets. The metrics are: Time required to estimate each set of data, Natural frequency average error (in percentage) and damping factor Root Mean Square Error deducting the worse 10% errors. 72
3.2 Results of running Laplace Wavelet and PRESTO algorithms over synthetic datasets. The metrics are: Time required to estimate each set of data, Natural frequency average error (in percentage) and damping factor Root Mean Square Error. 77
3.3 Summary table of MLP trained networks. Each column indicates the type of network (MLP) and the quantity of neurons in the hidden layer. 79
3.4 Summary table of DNN trained networks with two hidden layers and one output layer. Each column indicates the type of network (DNN) and the quantity of neurons in each hidden layer. 81
3.5 Summary table of DNN trained networks with three hidden layers and one output layer. Each column indicates the type of network (DNN) and the quantity of neurons in each hidden layer. 82
3.6 Summary table of CNN trained networks with five hidden layers and one output layer. Each column indicates the type of network (CNN) and the quantity of neurons in each hidden layer. 85
3.7 Summary table of CNN trained networks with six hidden layers and one output layer. Each column indicates the type of network (CNN) and the quantity of neurons in eacg hidden layer. 86
3.8 Results of running Laplace Wavelet, PRESTO and CNN 6x(40) algorithms over synthetic datasets. The metrics are: Time required to estimate each set of data, Natural frequency average error (in percentage) and damping factor Root Mean Square Error. 88
3.9 Linear regression over sampled data vs. reconstructed data, considering the Laplace Wavelet Matching Pursuit, PRESTO and a Convolutional Neural Network 6x(40). . . 92

Acronyms

AC Aerodynamic Center.

ADS Airbus Defense and Space.

CG Center of Gravity.

CLAEX Centro Logistico de Armamento y Experimentacion.

CNN Convolutional Neural Network.

DNN Deep Neural Network.

DOF Degree of Freedom.

EC Elastic Center.

FECU Flight Excitation Control Unit.

FFT Fast Fourier Transform.

FRF Frequency Response Function.

GVT Ground Vibration Test.

Kts Knots.

LCO Limit Cycle Oscillation.

MLP Multi Layer Perceptron.

MS Master of Science.

SVD Singular Vector Decomposition.

SW Software.

TPS Test Pilot School.

USAF United States Air Force.

ZLL Zero Lift Line.

Dedicado al amor de mi vida Luz, mis niños Iria y Leo y a mis padres Carmen y Sami.. . .

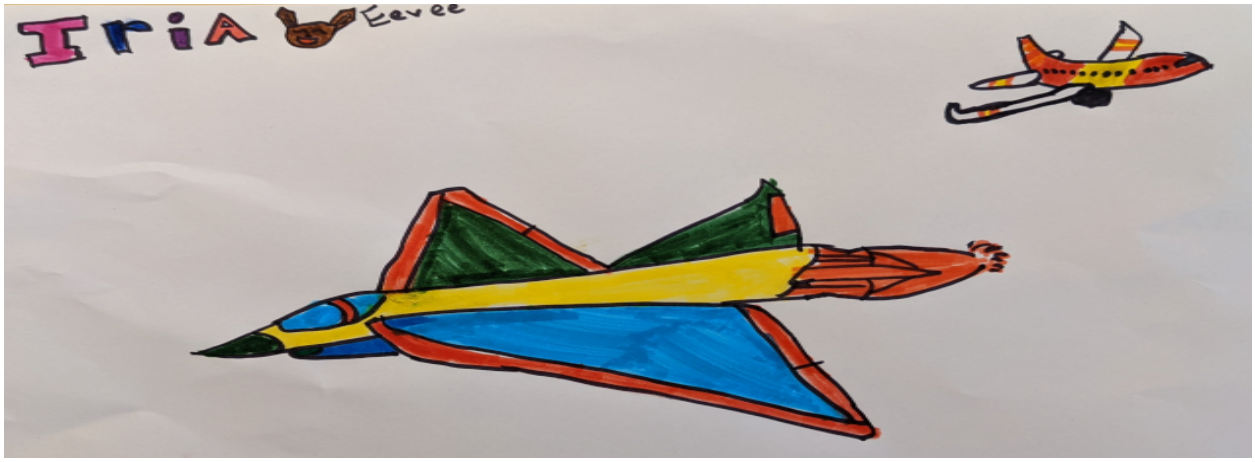

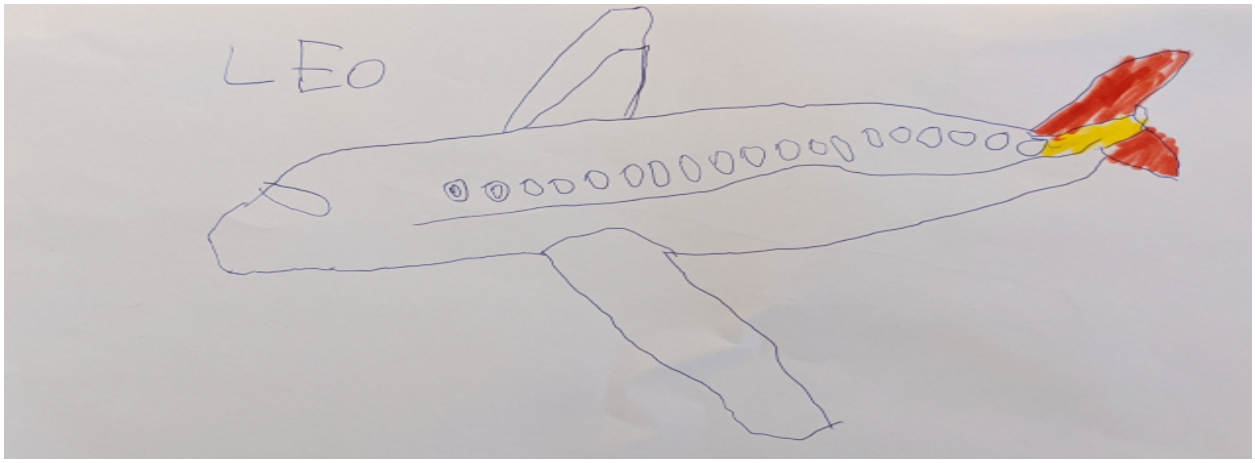

Chapter 1

Introduction, State of the Art and Scope of the thesis

1.1 Introduction

Aeroelasticity is a branch of aeronautics centered in studying combination of the forces acting on an aircraft, as will be described thoroughly in section 1.2.

One of the main problems in aeroelasticity is the flutter problem. Flutter involves the interaction of inertial, elastic and aerodynamic forces on the aircraft, in particular a resonant coupling between two different natural modes, entering into a self-exciting situation. In fact, flutter was one of the main reasons for airplane accidents even up to the between-wars period (1930s-1940s). According to the excellent historical perspective provided by Garrick and Reed, 1981, the first accurate study on flutter was made by Lanchester, 1916, who clearly determined that the cause for a "De Havilland" DH-9 accident was self-exited vibrations on the elevator. However, was Bairstow and Fage, 1916 who first set the equations of motion for the flutter phenomenon. Since then the phenomenon was known, but the uncertainty on the aerodynamic coefficients made not possible to accurately implement the lessons learned on prototypes until a decade later.

Nowadays, most of civilian aircraft are developed considering variations of wing structures based on models already implemented and developed, which proved to be tolerant to aeroelastic phenomena, enormously minimizing the tests required. However for military designs, where it is necessary to integrate different stores, it is still necessary to perform a full aeroelastic study.

1.2 Concept of Aeroelasticity

Aeroelasticity is one of the most important areas in aircraft design, since historically has been one of the main responsible phenomena for accidents during the early (and also current) days of aviation. As a broad definition it covers the interaction of aerodynamic, inertial and elastic forces, and nowadays, as a subarea of aeroelasticity, we can talk also about aero-servo-elasticity, which also includes the effects of servo-mechanic systems and control loops in the cocktail.

Collar, 1946 developed the well known Collar's triangle in a basic format, and was posteriorly complemented by Bisplinghoff, Ashley, and Halfman, 1983 as reproduced in figure 1.1.

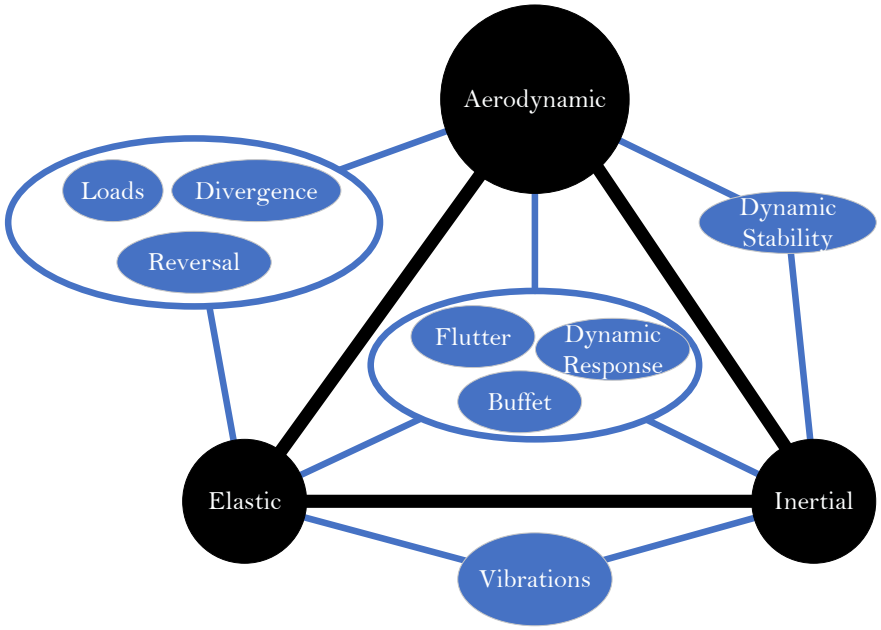

FIGURE 1.1: Collar's triangle

In the figure, the three main forces are represented in black:

- Aerodynamic
- Elastic
- Inertial

And the phenomena associated to these forces:

- Aerodynamic + Inertial:
  - *Dynamic Stability*. This is the classical study of the aircraft stability as a rigid-body. Note that the dynamic stability may be influenced under certain conditions by the deformation of the structure, and therefore it may be necessary to introduce this field of study inside of the triangle. This phenomenon is out of the scope of this thesis.
- Elastic + Inertial:
  - *Vibrations*. This field of study is the study of vibrations at zero (or negligible) airspeed, i. e. Ground Vibration Tests (GVT), Taxiing Vibration Tests (TVT), etc. The GVTs will be mentioned in this thesis as they are part of the Flutter Testing paradigm.
- Aerodynamic + Elastic:
  - *Load Distribution*. Represents the effects of loading the aircraft with aerodynamic forces and analyzing the effects on the deformation of the structure. This phenomenon will not be directly discussed in this paper, since a deeper analysis (also with a different scope) will be performed with the inclusion of inertial forces.
  - *Divergence*. The Divergence occurs when the restoring moment of the structure is exceeded by the aerodynamic torsional moment. The phenomenon of Divergence has

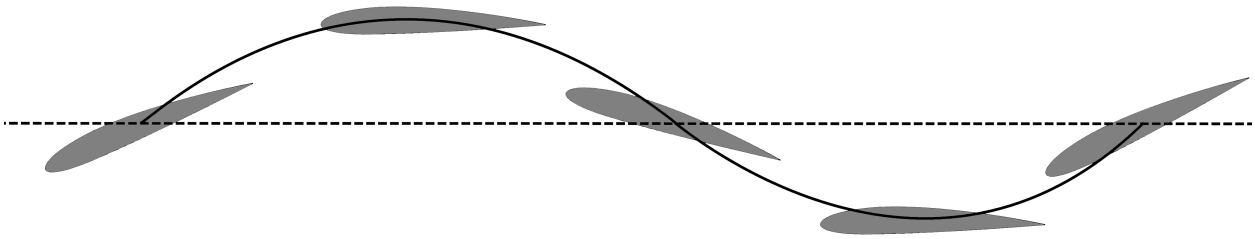

FIGURE 1.2: Physical depiction of an airfoil under flutter coupling. There is a 90º offset between torsion and bending motions.

historically been a field of deep study, since it was responsible for an important number of accidents during the early days of aviation. However it is a relatively simple phenomenon to calculate (with enough accuracy) and correct, and therefore nowadays most structures are designed so that the divergence point will not be a factor. In any case, during the design phase of an aircraft it is necessary to calculate the Divergence point and confirm that the structure will be free of divergence, either experimentally or by sufficient simulation, although this analysis is out of the scope of the present thesis.

- *Reversal*. Control Surfaces Reversal is a phenomenon known since the early days of aviation. Although the phenomenon is a clear case of aeroelastic behavior, it is out of the scope of this thesis.

- Aerodynamic + Elastic + Inertial
  - *Flutter*. This is the main topic of the present thesis, and will be discussed thoroughly.
  - *Buffet*. This effect is produced by transient vibration of structural elements. For example, boundary layer separation and reattachment close to the aileron. The discussion on buffeting is out of the scope of this thesis.
  - *Dynamic Response*. This effect is similar to buffet in definition. Transient vibration of structural elements. However the difference with Buffet is that in this case the loads are applied suddenly, like gusts or landings. In this case, the Control Reversal considering the weight of the wing during transient maneuvers would be analyzed here.

1.2.1 Concept of Flutter

Flutter is an aeroelastic phenomenon, and appears as the interaction between aerodynamic, inertial and elastic forces on a lifting surface. A very clear description can be found in the excellent handbook from J. Norton, 1990. In particular, the interaction is a self excited vibration result of the interaction of two natural modes of the structure initially orthogonal between them, which produce an exchange in energy. One of the modes will increase its energy out from the other and also from the air current, and therefore the interaction will result in one of the modes will get a reduction in amplitude, while the other will increase it up to a fracture point, on which the structure will fail with catastrophic consequences. The flutter point will start when one of the modes reaches a negative damping. At this point the amplitude of the critical mode starts to increase while the system absorbs energy. In the most simple case of flutter applied to airfoils, the bending-torsion flutter, there is also a very clear phase coupling between modes as depicted in figure 1.2. There is a 90º offset between the torsion and bending modes, while the lift is in phase between them.

To understand why two initially orthogonal modes start to get coupled together, it is necessary to see it from a different perspective. Flutter is a self exciting coupling between two aircraft modes initially at different frequencies, but those frequencies change and get close to a resonant

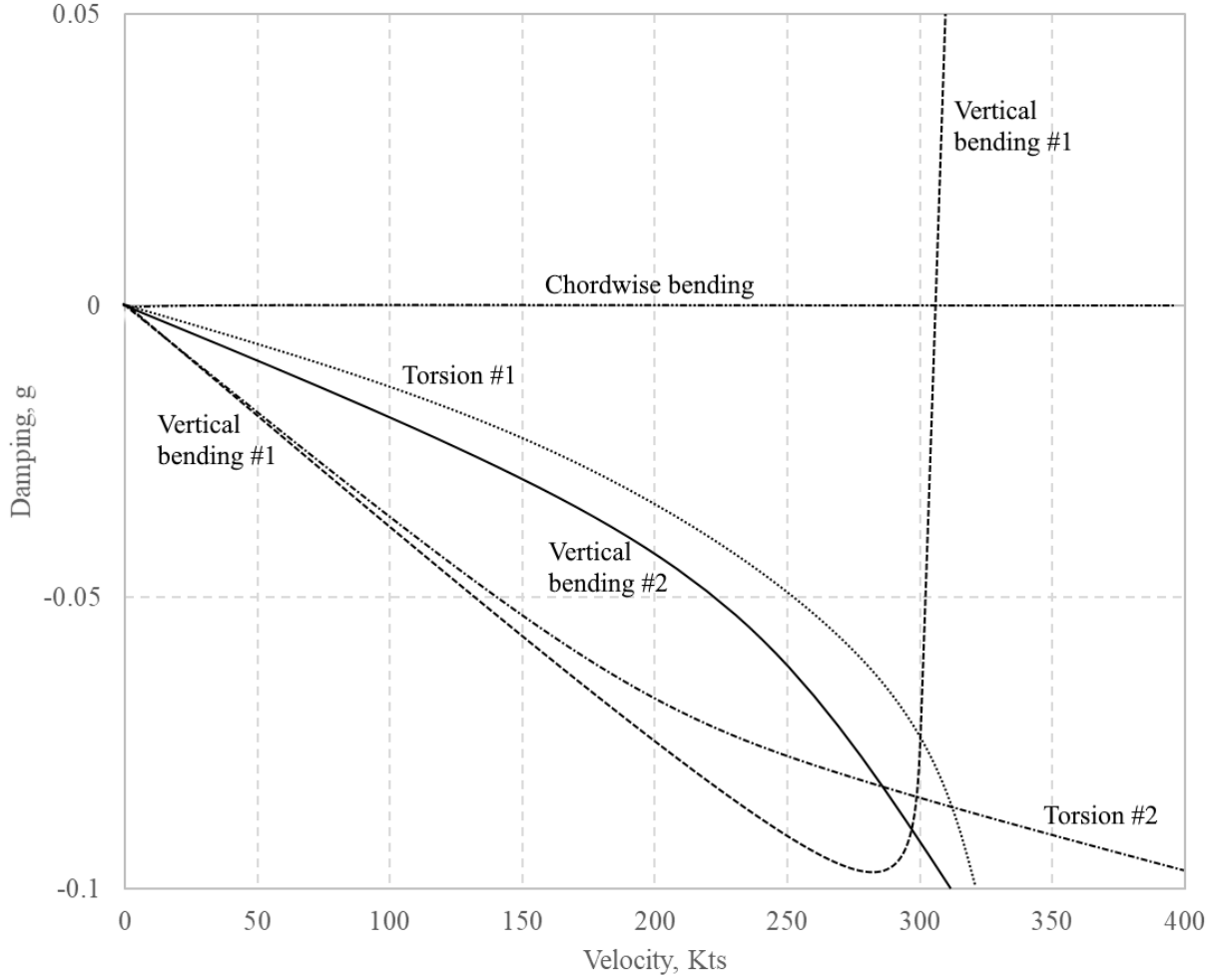

FIGURE 1.3: Typical V-G plot. Original plot extracted from Tian et al., 2016 and modified to match similar parameters to our case. Damping vs. Airspeed plot

frequency as airspeed (more accurately dynamic pressure) increases, approaching to the so called "flutter airspeed".

This phenomenon is depicted graphically in figures 1.3 and 1.4. Plot 1.3 shows the variation of damping for each natural mode (described with a descriptive name) with airspeed, while plot 1.4 shows the variation in frequency with airspeed for each natural mode. Please note that since the dynamic pressure is assumed to be a function dependent on pressure and airspeed, these plots at different altitudes are representatives of the behavior of the system.

The analysis from figures 1.3 and 1.4 shows several remarkable things. The "chordwise bending mode" keeps stable at approximately 0 damping, but it is not considered a critical mode according to JSSG-2006, 1998, and therefore is not included in the 3% damping rule. In fact it is descriptive of an LCO mode, an aeroelastic phenomenon similar to flutter as long as the damping is zero and to the pilot a frightening situation, but the amplitude doesn't change with increasing airspeed, and the equations are ruled by the "Van Der Pol oscillator". However, the LCO is beyond the scope of this paper. Rand, 2005 provides a very good description of the phenomenon. Another point to notice is the coupling between the "first vertical bending mode" and "first torsion mode", both shown in figures 1.5 and 1.6. As shown in figure 1.4, both modes change their frequency as airspeed increases, getting close together as they approach $300Kts$. At approximately $270Kts$ both modes enter into a self-excited vibrational situation, and figure 1.3 represents the fact with an

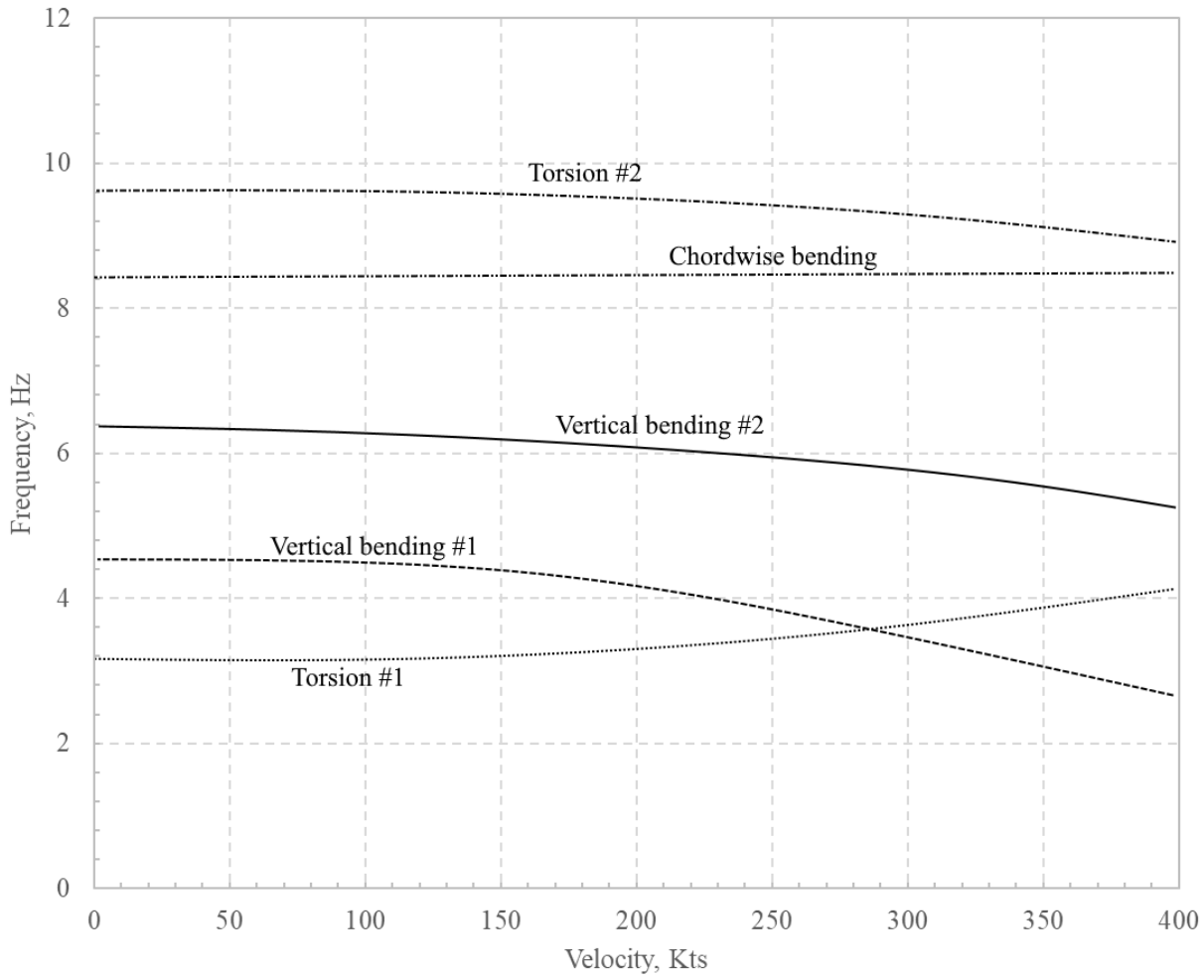

FIGURE 1.4: Typical V-G plot. Original plot extracted from Tian et al., 2016 and modified to match similar parameters to our case. Frequency vs. Airspeed plot

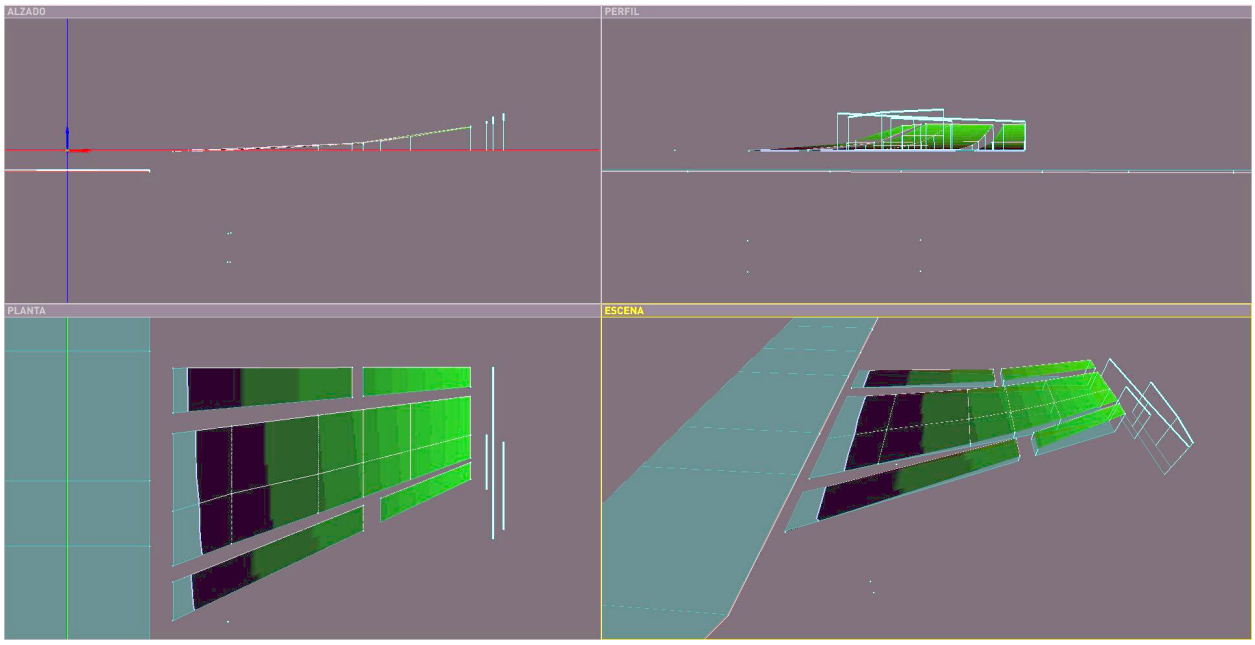

FIGURE 1.5: First vertical bending mode

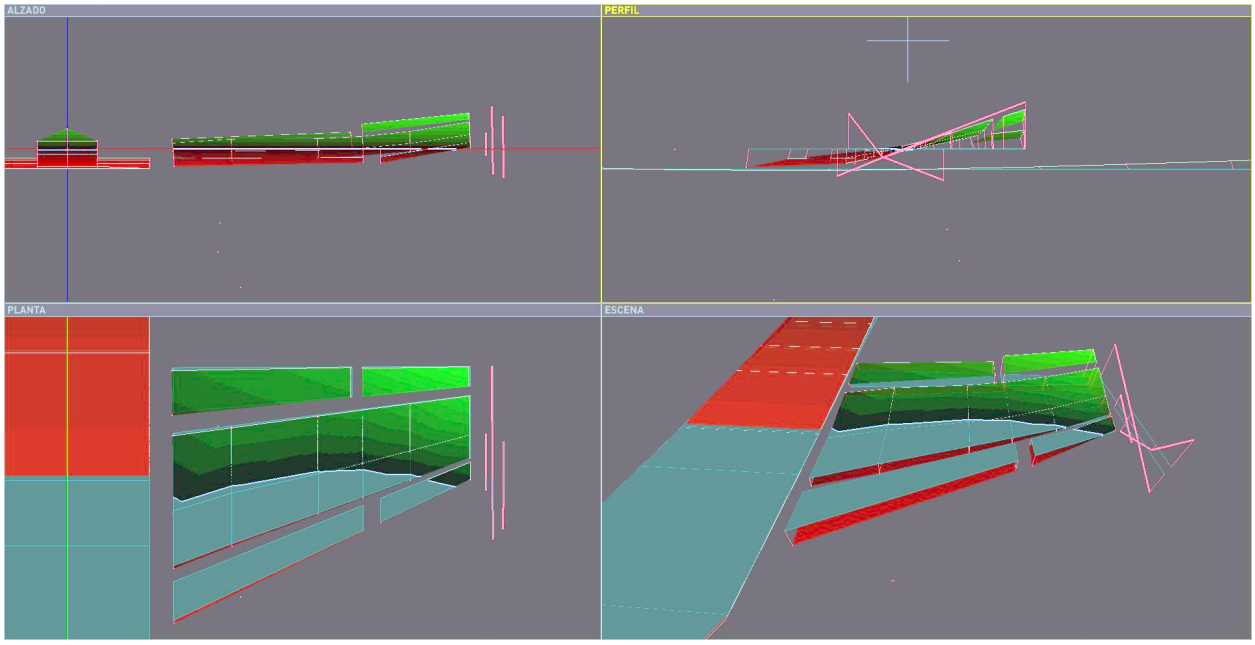

FIGURE 1.6: First torsion mode

explosive flutter of the "first vertical bending mode" rapidly passing damping above zero, while the "second vertical bending mode" reduces its damping. Please note the physical meaning of positive and negative damping. A negative damping implies that the amplitude of the structure's vibration will be reduced over time, while a positive damping implies that the amplitude will be increased over time (and eventually destroying the structure).

1.2.2 Flight Envelope

One of he steps in this study is the envelope definition and expansion involving external loads, which change the aeroelastic characteristics of the aircraft and could lead to flutter. The envelope is defined as the locus of the points on which the aircraft can safely fly. Figure 1.7 shows a typical flight envelope. The straight lines represent constant dynamic pressure lines, while dashed lines represent constant airspeed lines. The horizontal axis shows the Mach number and the vertical axis the pressure-altitude. The red lines limit the envelope. Beyond it the aircraft is unable to fly tor the reasons written in the diagram (typically). The stall speed [at a given altitude] represents the minimum airspeed the aircraft needs so that the maximum lift produced equals weight. The flight ceiling represents the maximum altitude the aircraft is able to reach. The maximum power boundary indicates the maximum airspeed the aircraft can reach with the engines at full power in straight level flight. At last, the flutter boundary will be the main topic for this thesis. Depending on the wing stores configuration the flutter dynamic pressure may vary, and therefore it is necessary to know where the new flutter boundary lies in order to define the most restrictive flight envelope for the pilot.

Please note that not always all the boundaries are reached. For example, in transport aircraft usually the flutter boundary is not relevant, and the limitation comes by the maximum power/transonic effects boundary. However in fighter aircraft the flutter boundary is usually one of the limiting factors.

1.2.3 Flutter and Envelope Expansion Testing paradigm

During an Envelope Expansion study for a given stores configuration, it is necessary to perform Flutter Flight Tests in order to validate the predicted-by-analysis envelope. The goal of the validation is to either:

1. Reach the flutter limit (extremely undesired)
2. Compare the expected frequencies and dampings predicted by the analysis with the actual values

In both cases it is necessary to accurately identify the frequencies and dampings of each natural mode at different dynamic pressures, in order to compare the analytic model with the parameters of the modes found during the Flight Tests.

Case 1 above, reaching the flutter limit, is a completely undesired situation. The case happens when the analytic model fails to predict accurately the modes and parameters, and the only means of preventing a catastrophic situation is by identifying low dampings on flight before they reach the flutter limit, preferably in real time.

Case 2 above is the preferred situation. The identification of parameters and comparison to the analytic model leads to an increase of the trust on the model, and therefore the number of test points can be reduced and safely reach a desired envelope with safety.

MIL-HDBK-516C, 2014 specifies that each aircraft configuration must be free of flutter and other undesirable aeroelastic phenomena. In particular for the USAF (the same criterion is followed at the Spanish Air Force) the criterion states to follow MIL-A-8870C, 1993 and JSSG-2006,

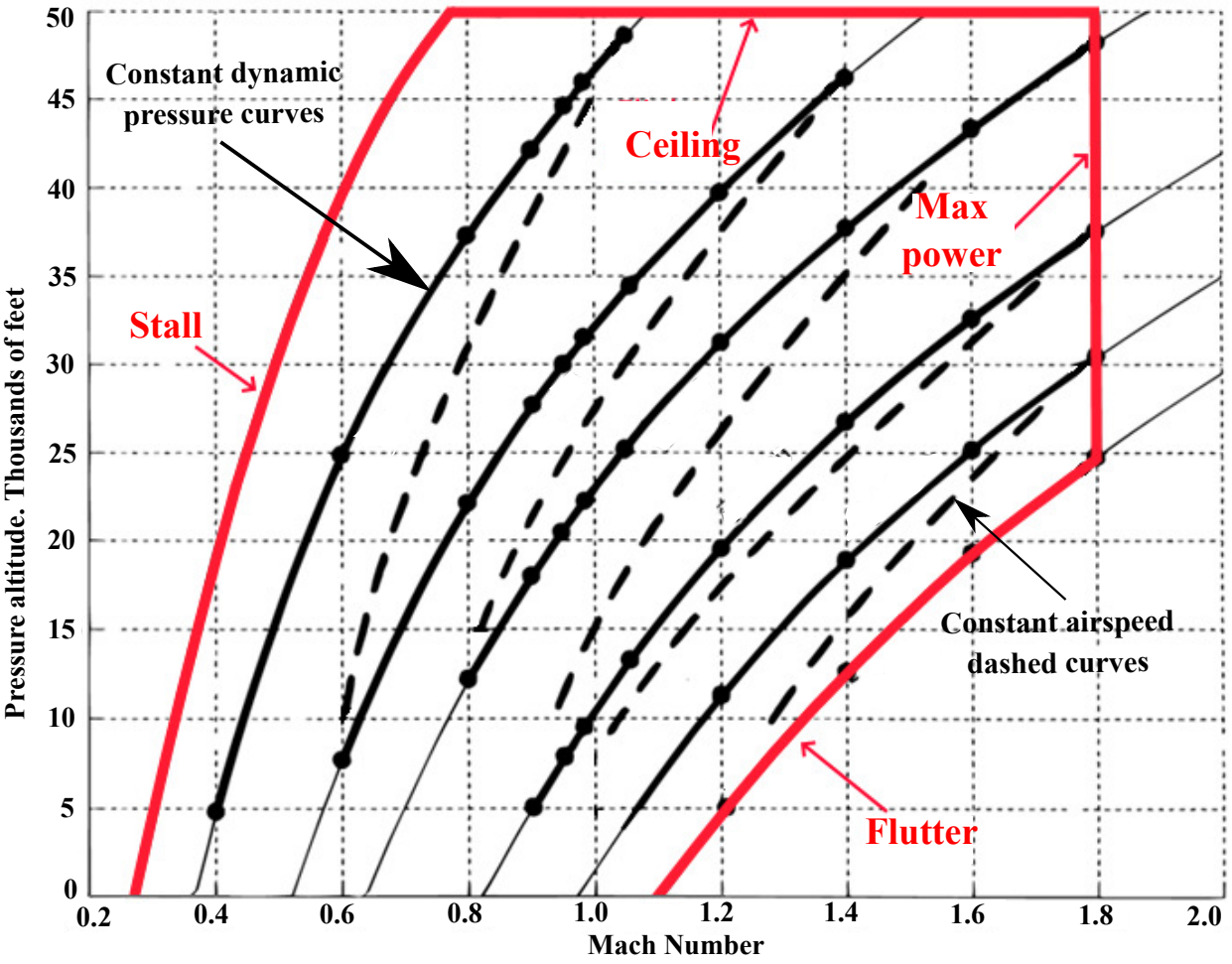

FIGURE 1.7: Flight envelope example. Straight lines indicate constant dynamic pressure curves q, while dashed lines represent constant airspeed. Image extracted from the USAF TPS Master of Science notes. Subject "Envelope Expansion Tests"

1998, which set the limitation for the most critical modes damping ratio in 0.03, defined as the logarithmic decrements calculation between two peaks of different amplitude in the vibrational time series data $g = \frac{1}{N\pi} Ln\left(\frac{A_i}{A_j}\right)$, where N is the difference between j and i and A_k is the amplitude in the vibrational time series of the peak number k. In order to demonstrate that it is required evidence through analysis and testing.

The Expansion Testing Paradigm followed is the one depicted in figure 1.8. We must take into account that the Flutter (in general all the Envelope Expansion) testing is considered a high risk test according to MIL-STD-882E, 2012. Even after applying all the possible mitigation procedures, the risk remains high.

The steps followed during a stores integration campaign are the following:

1. Prediction

   (a) Definition. Before integrating a new store in the aircraft it is necessary to define very clearly the necessity and expectations. This step is defined in the upper green box in figure 1.8. The most important considerations include (but are not limited to):

      i. Kind of store: We need to know the physical characteristics of the store. As a minimum for stores that can be considered a rigid solid without aerodynamic properties it is necessary to know the total mass, center of gravity relative to the holding lungs/rails and moment of inertia. If the store is slender and might be considered elastic and aerodynamic, it is also necessary to know the rigidity and aerodynamic matrices.

      ii. Expected envelope: It is necessary to define an "envelope of necessity". For example, if the store is intended for ground attack it might not be necessary to reach supersonic regime, given that supersonic regime would enormously increase drag and limit the effective range, and the limitation may be artificially set to a maximum range airspeed, even though the flutter boundary or engine power allow for a supersonic flight. However this may not be true for all scenarios, and therefore it is necessary to define an envelope of necessity.

      iii. Stores configuration: In this step the position of the stores is defined. Usually aircraft have different underwing stations, and it is necessary to define the positions of the stores. It might be possible that stores above certain mass cannot be installed in the external wing stations. Another thing to consider is if the store is installed with single or multiple launchers. Other factor is variable mass distribution, for example in the case of fuel tanks. The combination of different stores. For example in case wingtip missiles are transported along the new stores, it is necessary to consider different combinations of wingtip missiles with the new stores. At last, when all the different factors have been accounted for, it is necessary to evaluate all the possible combinations between factors, discarding the non applicable configurations.

   (b) Risk Analysis. Once defined the scope of the problem, it is necessary to do a risk analysis as part of the Test Plan in accordance with MIL-STD-882E, 2012. This analysis must take into account all the risks associated with the test assessing their severity and probability, and depending on the combination of both, in a first iteration, assign a risk assessment. After this initial assessment, mitigation procedures must be considered and described in the Test Plan in order to reduce the risk as much as possible. With these procedures implemented, a second iteration must be made to assess the residual risk. The risk category will be the assessment of the higher residual risk, and the consequences of this assessment will impact the level of authorizations required to approve the test and also the capability to change the test conditions once it is approved.

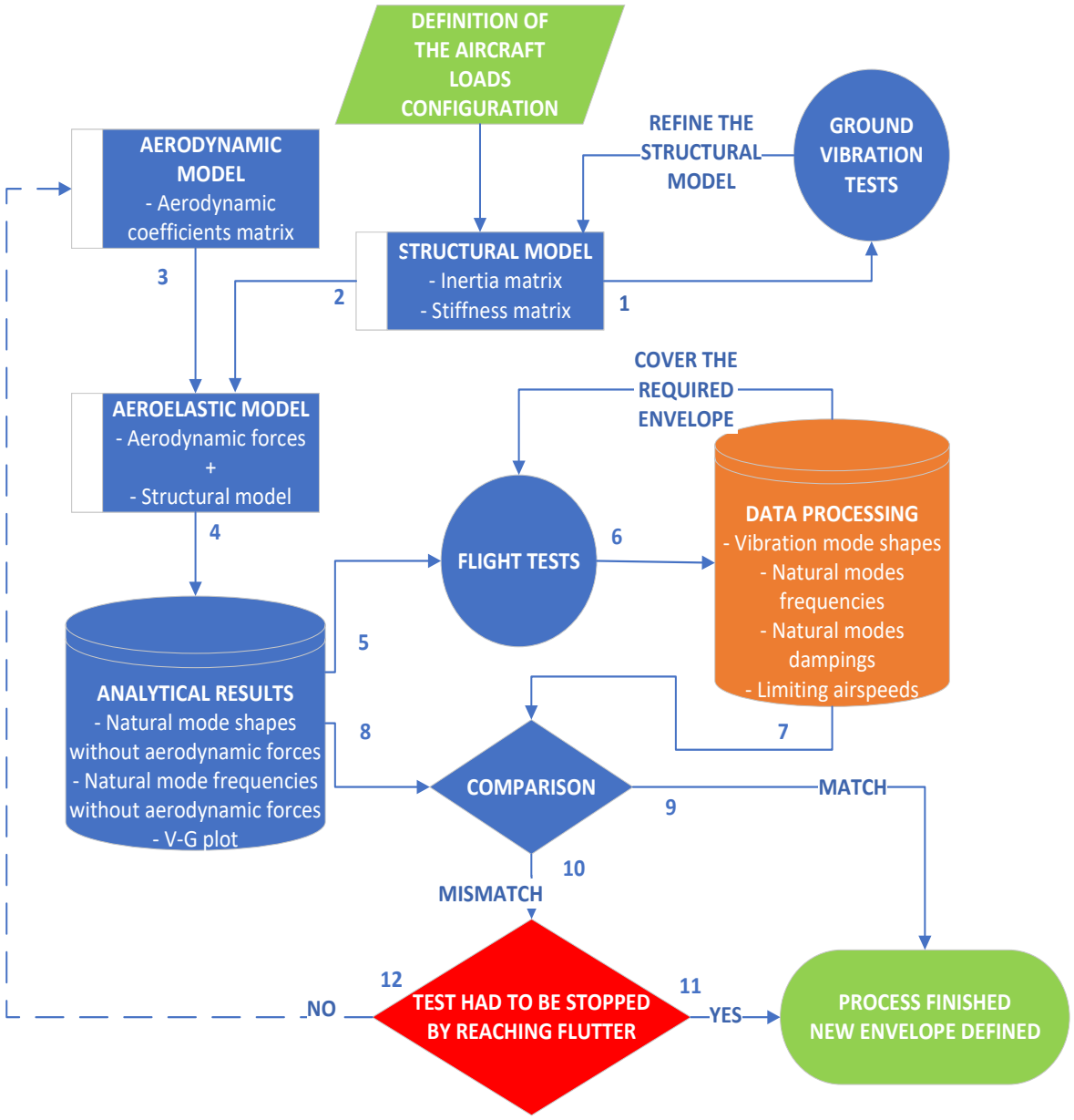

FIGURE 1.8: Flutter Flight Testing paradigm.

(c) Structural analysis. The requirements for this step are to have a previously defined elastic model of the aircraft. The usual SW package employed for this task is MSC NASTRAN's solution 103 (MSC. Software, 1994). In this phase the natural modes will be calculated. The natural modes are defined as the eigenvalues and eigenvectors of the homogeneous solution of the second degree differential equation of the structure. Figures 1.5 and 1.6 show the graphical outcome of this analysis. This analysis must be made for each flight configuration possible. For example, with full fuel load, 3/4 fuel load, one bomb dispensed...take into account that the combinations must consider the fuel available, the stores available and the mode symmetry (symmetric or anti-symmetric modes). In the case of the F-18, there are usually hundreds of combinations for a single stores configuration. These modes will define the initial conditions of the structure, and need to be validated with a Ground Vibration Test (path 1 in figure 1.8). The Ground Vibration Test will also refine the structural model in case there is a significant mismatch between the analytic and test results. This analysis will allow a full track of the evolution of these modes with increasing airspeed. A full description can be found in section 1.2.1.

(d) Flutter analysis. Once the structural analysis has been finished, it is necessary to know the evolution of these natural modes with building airspeed and also the flutter point. This analysis has two pre-requisites: The Natural Modes calculated in the previous step and the aerodynamic model, which includes the aerodynamic forces acting on each mass element of the structure. Even though there are different SW packages for this task, like MSC NASTRAN's solution 145 (MSC. Software, 1994) or ZAERO (Zona Technology, 2017), different companies usually employ their proprietary SW. It will return the V-G plots, similar to the ones shown in figures 1.3 and 1.4. In this case, it is necessary to add still more combinations to the previous ones. Depending on the technique chosen, it may be necessary to add different altitudes to the previous combinations (dynamic pressures) or altitudes and also Mach numbers to get "matched" solutions, which increase the number of combinations and the computational requirements. Paths 2 and 3 in figure 1.8 show this evolution. This topic will be thoroughly discussed in chapter 2.

(e) Critical modes identification. Once the previous analysis has been finished it is necessary to select a reduced number of aircraft configurations to perform the Flight Tests. Take into account that these tests are extremely costly and long in duration, given that many flights need to be canceled due to weather conditions, problems with the aircraft, etc, so it is very unlikely to fly more than two different configurations for the same loadings requirement. This step is represented as path 4 in figure 1.8. Once the critical modes have been identified we can proceed with the testing phase. Abou-Kebeh LLano and Vaquero Gomez, 2016 proposed a procedure to expedite the analysis and critical modes identification taylored to the tools available at CLAEX for the Spanish Air Force F-18.

2. Testing

(a) Ground vibration testing. The necessity for this step was described above, and is described by step 1 in figure 1.8. The aircraft will be configured with the critical configurations, set on jacks (or on the landing gear with the wheels deflated), instrumented to record the vibration of the aircraft as accurately as possible and connected to vibrational exciters. Then exciters start the vibration and the aircraft response is recorded. This way, the natural modes of the aircraft are identified experimentally. The mode shapes (eigenvectors) and frequencies (eigenvalues) are compared to the results from

the modal analysis. In case the results are assumed to be similar, the model is considered accurate and the confidence for the V-G plots is considered to be sufficient to proceed with the Flight Test. If not, the elastic model of the aircraft needs to be tuned up until there is sufficient convergence in the results. Several papers and algorithms are used for this task. Peeters and Auweraer, 2005 is a referent in these tests, and very detailed descriptions are made by Peeters et al., 2009.

(b) Flight Tests. Once the GVT demonstrated that the Natural Modes are trustworthy, it is necessary to carefully prepare the test points in order to safely approach the flutter airspeed and altitude (path 5 in figure 1.8). There is no standard requisite on how to approach those points. MIL-HDBK-516C, 2014, JSSG-2006, 1998 and MIL-A-8870C, 1993 only specify that the aircraft needs to be free of flutter (with a margin in airspeed) in the Flight Envelope, but doesn't specify how to approach the flutter point or prepare the tests. Piazzoli, 1970 and Stoliker, 1995 describe different procedures. But the procedure followed at CLAEX was taylored at USAF TPS. To start at the maximum envelope altitude and low airspeed (minimum dynamic pressure), and perform test points at different airspeeds, until either the flutter point or the limit of the planned envelope are reached. Then reduce altitude and start again with different test points and airspeeds until the whole envelope is cleared. These steps demand a careful and arduous job during the whole Flight campaign. On one side, the test is directed and monitored in real time from the Control Room. The vibrational data is sent by telemetry to the Control Room and the Test Director commands when to start the excitation and when to stop the test point, usually because the vibration is reaching an unacceptable amplitude level, building up at an unacceptable pace, coupling between modes... in general indications of a flutter onset. Even if the test has been followed correctly, it is necessary to analyze the results the same day of the tests in order to validate the previsions of the V-G plots, and depending on the results of that test day, select the test points for the next day (path 6 in figure 1.8). For this reason, it is paramount to accurately estimate and identify the frequencies and dampings from Flight Test Data in a reasonable time. Ideally in real (or nearly real) time, but if not, at least within a few hours. Paths 7 and 8 in figure 1.8 represent the necessity to compare the results between both results, the analytic and tests.

3. Validation

(a) Once all the data have been gathered, it is necessary to provide the final envelope and integration report to the Certification Authority. The comparison between the analytic and test results can be similar (path 9 in figure 1.8), in which case it is possible to extrapolate the flutter point safely, or dissimilar (path 10 in figure 1.8). This last condition also has two possible outcomes, to reach the flutter (or expected envelope) point (path 11 in figure 1.8), in which case the envelope is defined and the process is closed, or the flutter point has not been reached, but discrepancy is big enough as to require a recalculation of the analysis (path 12 in figure 1.8). For that reason it is necessary to get a final result on the frequencies and dampings of the global configuration at different airspeeds, so that there is a solid demonstration on the "free-of-flutter" requirement on the critical modes withing the envelope and 15% less airspeed than the 3% damping point, according to MIL-A-8870C, 1993 and JSSG-2006, 1998. In case that the 3% damping has not been reached, several predictors for the flutter point can be employed. In particular, in CLAEX the predictor employed is the "Flutter Margin", based on Zimmerman and Weissenburger, 1964 studies.

RISK ASSESSMENT MATRIX				
SEVERITY / PROBABILITY	Catastrophic (1)	Critical (2)	Marginal (3)	Negligible (4)
Frequent (A)	High	High	Serious	Medium
Probable (B)	High	High	Serious	Medium
Occasional (C)	High	Serious	Medium	Low
Remote (D)	Serious	Medium	Medium	Low
Improbable (E)	Medium	Medium	Medium	Low
Eliminated (F)	Eliminated			

FIGURE 1.9: Risk Matrix. Extracted from MIL-STD-882E, 2012

1.3 State of the Art

This thesis comprises different areas regarding aeroelasticity. As stated in section 1.4, equation-wise it will be divided in two main areas, a review of the aeroelastic equations and a review of the data processing techniques applied to Flutter Flight Test data processing and system identification. The main sources of documentation will be analyzed in this chapter.

1.3.1 Aeroelastic equations documentary basis

The first area, the theoretical basis of aeroelastic equations, depend upon fluid dynamics, stationary aerodynamics, non-stationary aerodynamics and theory of vibrations. These fields have not changed substantially in the latest years, so the source employed in the present thesis will be based on classical textbooks.

As for a historical introduction on flutter, different authors are cited. Garrick and Reed, 1981 and Hill, 1951 provided a very good overview of aeroelasticity along history, while Lanchester, 1916 provided the first mathematical description of the flutter problem and Bairstow and Fage, 1916 first described and mathematically analyzed a real flutter mishap.

The basic non-stationary aerodynamics equations were compiled by (Theodorsen, 1935 as the first thorough source. However the main reference for these developments has been provided by Bisplinghoff in Bisplinghoff, Ashley, and Goland, 1963 and Bisplinghoff, Ashley, and Halfman, 1983, one of the most comprehensive authors in the area, although complementary descriptions on the governing equations, mainly in the frequency domain, have been provided by Fung, 2008, and a very good summary of equations and developments were described by García-fogeda and Arévalo-Lozano, 2015. In this aspect, we must also cite the sources for numerical analysis of the flutter model, like MSC. Software, 1994 and Zona Technology, 2017, while García-fogeda and

Arévalo-Lozano, 2015 and Wright and Cooper, 2008 describe the general procedure to predict and construct the "V-G" plots via a numerical analysis.

The vibrations description and equations have been documented by Shabana, 1996; Hidalgo Martinez, 2010; Ewins, 2000; Meirovitch, 2000; Soroka, 1949 and French, 1971. In particular, the damping models have been documented by the classical sources in flutter cited above, mainly Bisplinghoff, Ashley, and Halfman, 1983 and García-fogeda and Arévalo-Lozano, 2015, and for data on experimental sources Coleman, 1940 and Kijewski and Kareem, 2000. It is also worth mentioning the contribution of Adhikari, 2000 as a review of different sources of damping.

Regarding fluid dynamics, the source for the Navier-Stokes equations development has been described in this thesis by White, 2016, and the aerodynamics equations, both stationary and non stationary, have been based on the excellent works from Meseguer Ruiz and Sanz Andrés, 2010 and Anderson, 2007.

The experimental analysis has been based mainly on the own experience of the author, and citing as a documentary basis the excellent works provided by Peeters et al., 2009; Piazzoli, 1970; J. Norton, 1990 and Stoliker, 1995. It is also worth mentioning Chajec, 2018 as a source for Ground Vibration Tests information and Abou-Kebeh LLano and Vaquero Gomez, 2016 for the pre-Flight Test analysis phase.

1.3.2 Flutter Data Processing Documentary Basis

The aim of this section is focused on the state of the art regarding the data post-processing. It is necessary to remark that validated sources are hard to find, since the Flutter Tests are extremely dangerous and costly. For that reason different companies develop their own techniques and keep their results and procedures secret.

Regarding authors who provided data validated with actual experiments, we can cite Coll, 2016 to have developed the Jflutter software package, which is employed nowadays by Airbus to identify natural modes in flutter flight test data, along with Peeters et al., 2009; Peeters and Auweraer, 2005, whose Polymax algorithm is also employed by Airbus and CLAEX for ground vibration tests on real aircraft. These authors have developed fast, robust and validated techniques. However the data required for these techniques implies a large recording time, around 60 seconds minimum, which by nature is incompatible with the Sine Dwell excitations recording time for safety reasons.

The data processing source handbooks mainly used in this paper come from Oppenheim and Schafer, 2009 and Bishop, 2021, and the source for the optimization algorithm, Trust-Region, from Coleman and Li, 1996 and Yuan, 2000.

The different techniques evaluated are Prony and Prony variant methods, in particular Matrix Pencil, citing Almunif, Fan, and Miao, 2020; Barros-Rodriguez et al., 2015; Potts and Tasche, 2010 and Kiviaho, Jacobson, and Kennedy, 2019, taking also into consideration the techniques by Patel et al., 2013 to sort the natural modes returned. The Peak-Amplitude method was described by Ewins, 2000 and will prove to be extremely useful to estimate the seeds for the optimization algorithms. The techniques described in this paragraph show different advantages and drawbacks. In general they are all extremely fast compared to other techniques. However the lack of phase information in the aforementioned methods produced a bad estimation compared to other techniques. These techniques will be discussed later in chapter 3.

However, the most important source in this area for the present thesis has been Freudinger, 1989 and Freudinger, Lind, and Brenner, 1997, based on Matching Pursuit techniques. For these, the works from Goodwin, 1997 and Zhu, 2007 were used as a reference to develop the Matlab algorithm employed in the simulations. The aforementioned authors describe the Laplace Wavelet Matching Pursuit technique, which has been used as a source of validation for the present thesis, as those papers themselves also validate experiments on real Flutter Flight Tests on USAF F-18A/B aircraft, the same source airplane from which the data for the present thesis have been provided.

The Laplace Wavelet technique has proved to be a reliable and robust technique to identify Sine Dwell flutter signals, but has an important drawback in the computational power required, which makes it unusable for real time data processing unless a cluster is available for the test team. That considered, this technique will follow extensive discussion in chapter 3 and will be the most important referent for comparison in this thesis.

At last, the damping model employed will be the viscous damping model. There are many different damping models, as described by Adhikari, 2000 and Shabana, 1996. However the main two damping models described in aeroelasticity are the structural damping model and viscous damping model, as described by the main textbooks in aeroelasticity, like Bisplinghoff, Ashley, and Goland, 1963, García-fogeda and Arévalo-Lozano, 2015 and Fung, 2008 to cite only a few. The reason to chose viscous damping over structural damping is because authors like Barros-Rodriguez et al., 2015; Freudinger, 1989 and Coll, 2016 employ it either implicitly or explicitly in their calculations, also it can be demonstrated that the viscous damping model has a simple relationship with structural damping and, as a final argument, the viscous damping model has returned very good results with the techniques developed in chapter 3.

1.4 Objective, Scope and Limitations

Under the light of the discussion carried out in section 1.3, the scope of the thesis will cover:

- An insight on the concepts of aeroelasticity, flutter and flutter testing paradigm, as described in the introduction
- A brief review of Aeroelasticity and the main flutter governing equations
- A brief review on data processing and the problems associated with short time and low frequency signals
- Present a new robust technique for Flutter Flight Test data processing and system identification based on identifying short time and low frequency signals associated with aeroelastic natural modes

Although the Flutter Testing Paradigm involves several steps described in this thesis, the scope will be limited to the Flight Test Data Postprocessing and System Identification.

1.5 Description of the Problem

The problem described in this thesis is related to the accurate identification of different natural modes parameters found during Flutter Flight Tests, in particular frequencies and dampings of each natural mode of interest (participating in the flutter mechanism). The identification of the frequencies and dampings will allow to assess the risk associated with the next flight and the necessity to proceed with a given dynamic pressure or not. The techniques employed nowadays face many issues, since to accurately identify the system it is necessary to gather long duration datasets, which involves a risk itself, or gather short time datasets, which are usually poor in quality and repeatability.

The main goal of this thesis is to present a new and robust technique to identify those parameters from Flutter Flight Test data, considering short time datasets and allowing for repeatable results.

1.6 Work Hypotheses and assumptions

This thesis will be based upon several work hypotheses, from which the main are:

- Exponentially damped sinusoids: The signals follow an exponentially damped sinusoids model. This hypothesis is concurrent with the general flutter theory, and is well developed in almost every paper and textbook on aeroelasticity, like Bisplinghoff, Ashley, and Halfman, 1983, Fung, 2008, Wright and Cooper, 2008, García-fogeda and Arévalo-Lozano, 2015, etc.
- Viscous damping: The damping model to be used is based on a viscous damping model. The main two models accepted for damping in aeroelastic applications are structural and viscous. However there is a relationship between both models, as will be demonstrated in section 2.3.2.1. For that reason and given the convenience of the mathematical model, the viscous damping model will be used.

Also, this thesis is constrained by one main condition. The datasets will be limited to sine dwell excitations. This condition implies time series signals with a very short duration (2 to 5 seconds) and low frequency (2 to 10 Hz). There are a series of pros and cons with this approach compared to frequency sweeps, as a reference:

- Cons:
  - Sine dwells are a very restrictive condition, considering the effort required to obtain accurate and repetitive results, since the noise and local minima affect enormously the results.
  - Requires the pilot to get closer to the flutter point than, for example, frequency sweeps, with the danger involved. Please note that this drawback is not minor.
- Pros:
  - The time to stay close to the flutter point is minimum, since the duration of the maneuver is minimum (3 to 5 seconds) compared to, for example, frequency sweeps (around 60 seconds).
  - Even though getting accurate numbers in terms of frequency and damping is complicated, during the test, close to the flutter point, is very easy to see qualitatively a near-flutter trend and coupling between modes, so it allows to get the optimum envelope boundaries with very limited (or even none at all) computational power.

1.7 Methodology of Investigation

As described in section1.4, we have three main parts in this thesis.

- Review on Flutter equations. The main equation of aeroelasticity particularized for flutter will be described and its most relevant parts demonstrated. Chapter 2 will demonstrate the physical principle of flutter. Each section of this chapter will focus on the reconstruction of the flutter equations by developing each term of the flutter equations, and at last will demonstrate the physical principle of flutter and the relationship with the different terms.
- Characterization of the flutter signals and parameters. The case described in section 1.5 will be analyzed, considering that the short time and low frequency signals have a series of implications on the processing of data that will affect the resolution of the problem. The first part of chapter 3 will describe the particularities associated with different parameters in the flutter solution and their influence in the identification of the flutter parameters. In particular:

  - Develop a mathematical framework analyzing the influence of the phase angle in the flutter equations related to the estimation of frequency and damping.
  - Develop a mathematical framework analyzing the influence of the Power Spectrum bandwidth in the flutter equations related to the estimation of frequency and damping.

- Flutter Flight Test data identification techniques. The second part of the investigation in chapter 3 will be focused on reviewing state of the art Flutter Flight Test data processing algorithms and perform a comparison between them:
  - Compare different algorithms to identify signals on synthetic datasets. The metrics employed will take into account the closeness between the generating parameters and the identified parameters.
  - Compare the best two of these techniques to identify signals on real datasets. The metric employed will be a regression curve, between the real data and the reconstruction of the signals with the identified parameters.

Chapter 2

Materials and Methods

The equations of flutter, as stated in section 1.2, are based upon elastic, inertial and aerodynamic forces. In regular textbooks about aeroelasticity there are chapters dedicated to elasticity and steady and unsteady aerodynamics before describing the flutter equations. The reason to follow this approach is to construct and solve the flutter differential equations and solutions, based on the different forces intervening in the mechanism of flutter, and we will refer to this approach as the "direct problem". The "inverse problem" will be, given a set of signals originated from an aeroelastic source (in our case from a flutter flight test), identify the modal frequencies and dampings contributing to the vibration.

Even though the approach in this thesis will not be to solve the direct problem (given a set of masses, contour conditions and relations between them estimate the flutter frequencies, dampings and airspeeds), but the inverse problem instead (given a vibration signal generated by an aeroelastic phenomenon at a given dynamic pressure, identify the frequencies and dampings intervening in the mechanism), it is important to demonstrate the relationship between the different forces participating in the mechanism of flutter and, as a last stance, in the signals received.

As stated above, the first part of the present chapter will be dedicated to demonstrate the mechanism of flutter. As an advance and brief summary of section 2.6, the flutter equation is constructed from a forced second degree linear differential equation. The most common means of constructing this equation is applying the minimum action principle through Lagrange's equation to the Lagrangian of the system. García-fogeda and Arévalo-Lozano, 2015; Bisplinghoff, Ashley, and Goland, 1963 and most authors employs such approach. However applying Newton's laws approach will provide a clearer understanding of the mechanism of flutter, and hence will be the approach followed in this thesis. Note that this decision is not trivial. The present thesis involves different areas of knowledge, say Signal Processing and Aeroelasticity, which are typically unknown between them. This fact implies that many readers will require an effort to understand some developments while others will be trivial, and for other readers the same fact will be true with the reverse sets of developments. For this reason, one of the biggest effort in this thesis will be to summarize and simplify the developments as much as possible, and be as didactic as possible in order to ease the effort from both sets of readers. Also, taking into account that the thesis was directed and tutored by Authorities in Signal Processing, the notation in the upcoming chapters and sections will be different from what is usual in Aeroelasticity and related disciplines, to adapt to a less conventional but easier to understand model for people not accustomed to the classical notation.

To understand the mechanism of flutter we need to demonstrate the intrinsic dependency of each term in the main equation of dynamic aeroelasticity. We will demonstrate the derivation of the terms and the dependency on different parameters.

The main equation describing dynamic aeroelastic phenomena is a forced second degree linear equation which will be presented in further sections, and the terms are the following:

- Inertial forces: $M\frac{d^2x}{dt^2}$. Where for one degree of freedom M is a mass element constant subjected to vibration and x represents its displacement variable in generalized coordinates.

This term represents the **third Newton's Law**, and will be discussed in more detail in section 2.2.

- Damping forces: $C\frac{dx}{dt}$. Where C represents the damping factor. The form expressed here is the viscous damping model for 1 degree of freedom, employed by the Author to derive the conclusions in this thesis. However it is possible to apply different damping models which don't depend on the velocity of the mass element. Sections 2.3.1 and 2.3.2 will discuss some different damping models and solutions.
- Elastic forces: Kx. The one expressed here is the most basic form of **Hooke's Law** for 1 degree of freedom. For multiple degrees of freedom, the equation is basically the same, but instead of a single parameter a elastic matrix will be employed and a displacements vector, combining the contributions of the displacement of different mass elements of the system for each equation $\mathbf{K} \cdot \mathbf{x}$. These equations will be derived in section 2.4.
- Unsteady aerodynamic forces: $q_a = f\left(\alpha, \frac{d\alpha}{dt}, \frac{d^2\alpha}{dt^2}, \frac{dh}{dt}, \frac{d^2h}{dt^2}, Q_p\right)$, meaning that the unsteady aerodynamic forces depend upon the angle of attack α and its first $\left(\frac{d\alpha}{dt}\right)$ and second $\left(\frac{d^2\alpha}{dt^2}\right)$ time derivatives, and the vertical displacement first $\left(\frac{dh}{dt}\right)$ and second $\left(\frac{d^2h}{dt^2}\right)$ time derivatives and the dynamic pressure Q_p. Section 2.5.1 and 2.5.2 provide the demonstrations for the stated dependency.

Once the forced second degree linear differential equation terms have been demonstrated, section 2.6 will demonstrate the relationship between all the terms and the mechanism of flutter.

Then a brief discussion on the characteristics of short time and low frequency signals will be described in section 2.7, followed by a description of the actual signals found during a flutter test campaign in section 2.7.1.

2.1 Introduction to the flutter mechanism

The standard equation of motion (Wright and Cooper, 2008, Bisplinghoff, Ashley, and Goland, 1963, MIL-A-8870C, 1993 and others) starts assuming a second degree differential equation with subcritical damping, in the form described in equation 2.2 as solved by different authors, like Hidalgo Martinez, 2010; Shabana, 1996; Meirovitch, 2000 and others. **This example will consider one single degree of freedom**, since the final objective is to reduce to independent variables (degrees of freedom) all the matrix equations. The reason for this is that the flutter testing standards, like MIL-A-8870C, 1993; JSSG-2006, 1998 define a particular model and flutter limit as a damped sinusoid, and therefore it is necessary to search for a model that matches these standards.

We will start defining several parameters that will be useful later on:

$$
\begin{aligned}
&\zeta = \frac{C}{C_{cr}} \;\; Damping\, factor \\
&C_{cr} = 2\sqrt{K \cdot M} \;\; Critical\, damping \\
&\omega_n = \sqrt{\frac{K}{M}} \;\; Natural\, frequency \\
&\omega_d = \omega_n \cdot \sqrt{1-\zeta^2} \;\; Damped\, natural\, frequency \\
&Q_d = \frac{1}{2}\rho u^2 \;\; Dynamic\, pressure \\
&\rho = \;\; Air\, density \\
&u = \;\; Airspeed
\end{aligned}
\tag{2.1}
$$

The starting point will be the following differential equation:

$$M \cdot \frac{d^2x(t)}{dt^2} + C \cdot \frac{dx(t)}{dt} + K \cdot x(t) = q_a(x(t), \frac{dx(t)}{dt}, \frac{d^2x(t)}{dt^2}, Q_d) \tag{2.2}$$

In this equation the terms $x(t)$ represents the displacement variable in generalized coordinates, t represents the independent time variable, M represents the mass of the element (constant), C represents the damping constant, K represents the elastic parameter, q_a represents the aerodynamic forces as a linear dependent function on the displacement variable and its derivatives and Q_d, which represent the dynamic pressure, parameter that accounts for the altitude and airspeed of the aircraft. Notice that for our purposes we will only consider subcritical vibrations, and therefore the damping parameter C will be smaller than the critical damping parameter C_{cr} ($C < C_{cr}$).

The homogeneous version of equation 2.2 describes a vibrational movement with a particular natural frequency $\omega_{n,0}$ and damping ζ_0. However note that the aerodynamic forces q_a depend linearly on the same variables as the left hand side of the equation. Therefore, for each dynamic pressure $Q_{d,i}$ we can define a quasi-stationary homogeneous equation, transferring the aerodynamic forces to the left hand side of the equation:

$$\begin{aligned}(M - q_{a,3}(Q_{d,i})) \cdot \frac{d^2x(t)}{dt^2} + (C - q_{a,2}(Q_{d,i})) \cdot \frac{dx(t)}{dt} + (K - q_{a,1}(Q_{d,i})) \cdot x = 0 \iff \\ \iff M'(Q_{d,i}) \cdot \frac{d^2x(t)}{dt^2} + C'(Q_{d,i}) \cdot \frac{dx(t)}{dt} + K'(Q_{d,i}) \cdot x(t) = 0\end{aligned} \tag{2.3}$$

Where $q_{a,j}$ indicate the aerodynamic forces term corresponding to the respective derivative of x and the prima (M', C', K') values represent the modified terms of the equation at different dynamic pressures $Q_{d,i}$. Note here that in this case we are considering quasi-stationary evolutions, and therefore the dynamic pressure will be considered a parameter instead of a variable.

Equation 2.3 will be key to understand the mechanism of flutter in section 2.6 when applied to several degrees of freedom. This equation describes the evolution of the natural frequencies and dampings (and also mode shapes when considering multiple degrees of freedom) of each mode as the dynamic pressure changes.

The solution to equation 2.3 is an exponentially damped sinusoid of the form:

$$x(t) = Ae^{-\zeta\omega_n t}\sin(\omega_d \cdot t + \varphi) \tag{2.4}$$

Here A represents the amplitude constant and φ the phase angle of the sinusoidal movement. The rest of the parameters are defined above (2.1).

Equation 2.4 will be the equation model that will be employed to identify the signals as a solution to the problem described in section 1.5, and the main focus of this thesis.

2.2 First term: Inertial forces

The inertial forces constitute the third Newton's law:

$$\mathbf{f}_i = \mathbf{M} \cdot \frac{d^2\mathbf{x}(t)}{dt^2} \tag{2.5}$$

Where $\mathbf{f}_i$ represents the inertial forces vector, $\mathbf{M}$ is the inertia matrix and $\mathbf{x}(t)$ is the vector of displacements in generalized coordinates.

Particularized for two DOF in our problem, an airfoil with pitch (rotation) and plunge (vertical displacement) movements, the matrix $\mathbf{M}$ can be expressed as follows:

$$\mathbf{M} = \begin{bmatrix} M & S_\alpha \\ S_\alpha & I_\alpha \end{bmatrix} \tag{2.6}$$

Where M is the mass of the airfoil, S_α is the static moment of first order, meaning the contribution of the rotation of the airfoil to the vertical displacement of the center of gravity (note that the rotation will be produced around the elastic axis, which in general doesn't coincide with the center of gravity) and I_α is the moment of inertia of the airfoil.

The demonstration of this Law is out of the scope of this thesis and actually poses no discussion or complexity. Only suffices to say that when considering multiple degrees of freedom, the inertial matrix constitutes the matrix of a positive definite quadratic form, since represents the contribution of the kinetic energy, and therefore, the inertial matrix is symmetric (Shabana, 1996).

2.3 Second term: Dissipative forces (damping)

The damping forces will require a deeper discussion. In particular different damping models exist, and therefore it is necessary to discuss the different alternatives.

The main three damping models applied by authors, like Wright and Cooper, 2008; Adhikari, 2000; Ewins, 2000, in flutter investigations will be used. We will provide a comparison between the *proportional damping model* applied to multiple degrees of freedom, the *structural damping model*, and the *viscous damping model*.

For multiple degrees of freedom, depending on the damping model the damping matrix can or cannot be symmetric. In the case of proportional damping the damping matrix can be definite positive or semidefinite positive, and therefore not necessarily symmetric. For structural or viscous damping, we cannot state anything about the nature of the governing matrix.

2.3.1 Undamped vibrations

Even though undamped vibrations don't constitute a damping model themselves, it is presented here for comparison reasons. The development of this section is a basic development that can be found in classical textbooks on vibrations, like Shabana, 1996, Meirovitch, 2000, French, 1971,Hidalgo Martinez, 2010, etc.

We will start with the second degree differential equation in its homogeneous most general case matrix form, without considering damping. The forced solution will not be developed, since the upcoming sections modify the system of equations into a homogeneous system.

$$\mathbf{M} \cdot \frac{d^2\mathbf{x}(t)}{dt^2} + \mathbf{K} \cdot \mathbf{x}(t) = 0 \tag{2.7}$$

Where $\mathbf{M}$ is the mass matrix, $\mathbf{K}$ the stiffness matrix, $\mathbf{x}(t)$ the displacement vector in generalized coordinates and $\frac{d^2\mathbf{x}(t)}{dt^2}$ the accelerations vector.

This equation can be solved by considering a solution of the form:

$$\mathbf{x}(t) = f(t)|_\omega \cdot \mathbf{\Psi} \tag{2.8}$$

Where $f(t)|_\omega$ needs to be a harmonic function (for non trivial eigenvalues $\omega > 0$) or a linear function in t (for trivial eigenvalues $\omega = 0$) and $\mathbf{\Psi}$ is a constant vector of the same dimensions as our coordinates space (eigenvector).

The demonstration of the solution of this equation is out of the scope of this thesis, but can be found in Hidalgo Martinez, 2010. The final equation yields:

$$\left(\mathbf{K} - \omega^2\mathbf{M}\right)\mathbf{\Psi} = 0 \iff det\left|\mathbf{K} - \omega^2\mathbf{M}\right| = 0 \tag{2.9}$$

Where the solution of the determinant for different values of ω will represent the different eigenvalues of the system $\boldsymbol{\omega}_j$, say the natural frequencies of the system, and eigenvectors $\boldsymbol{\Psi}_j$, representing the different mode shapes of the system. From the individual eigenvectors we can also define the eigenvectors matrix $\boldsymbol{\Psi}$.

2.3.1.1 Modal shapes

We will now describe a very useful (and basic) feature related to modal analysis from linear algebra, the modal shapes of the system, meaning the principal directions of vibration defined by the eigenvectors of the system.

If we pre- and post-multiply the mass $\mathbf{M}$ and stiffness $\mathbf{K}$ matrices by the eigenvectors matrix $\boldsymbol{\Psi}$:

$$\begin{aligned} \boldsymbol{\Psi}^T \mathbf{M} \boldsymbol{\Psi} &= \mathbf{M}_r \\ \boldsymbol{\Psi}^T \mathbf{K} \boldsymbol{\Psi} &= \mathbf{K}_r \\ \mathbf{x}(t) &= \boldsymbol{\Psi} \cdot \mathbf{q}(t) \end{aligned} \tag{2.10}$$

Where $\mathbf{M}_r$ is the modal mass matrix, $\mathbf{K}_r$ is the modal stiffness matrix, the superindex ^{T} indicates transposition and $\mathbf{q}(t)$ is the modal coordinates vector.

The main property of those two matrices 2.10 are that they are diagonal in the state space defined by the eigenvalues, fact that simplifies enormously the calculations when trying to estimate the modal shapes and also will be important when considering damping, as will be demonstrated in section 2.3.2.

Pre-Multiplying equation 2.7 by the modal matrix $\boldsymbol{\Psi}^T$ and substituting the coordinates vector $\mathbf{x}(t)$ by the third equation 2.10, equation 2.7 can be written in modal coordinates as (the demonstration, even though is trivial, can be found in the references cited in the beginning of the section):

$$-\boldsymbol{\omega}_j^2 \mathbf{M}_r \cdot \mathbf{q}(t) + \mathbf{K}_r \cdot \mathbf{q}(t) = 0 \tag{2.11}$$

Note that we introduced the diagonal eigenvalues matrix $\boldsymbol{\omega}_j$, resulting from the second derivative of $\mathbf{x}$ in equation 2.7 considering the definitions in 2.1. The particularity of equation 2.11 is that the matrices are diagonal, and therefore can be solved as independent equations of motion for each DOF.

The solution for this system of equations is the following:

$$q_j(t) = A_j \cdot sin(\omega_j t + \varphi) \tag{2.12}$$

Where A_j is a generic constant, ω_j the natural frequency of that mode and φ the phase angle. Note that this solution is oscillatory without any damping factor.

The eigenvectors matrix $\boldsymbol{\Psi}$ represents the natural modal shapes of deformation of the structure, while the eigenvalues diagonal matrix ω_j represent the natural frequencies of the system

To understand this important conclusion, the structure will resonate at the frequencies ω_j, and the vibrating shape of the structure will be defined by the respective eigenvectors $\boldsymbol{\psi}_j$.

2.3.2 Damping and damped vibrations

Damping represents the contribution of dissipating forces to the system. Considering the second degree equation 2.2 in its homogeneous form with a general case damping (represented here one single DOF for clarity):

$$M \cdot \frac{d^2x(t)}{dt^2} + C \cdot \frac{dx(t)}{dt} + K \cdot x(t) = 0 \tag{2.13}$$

the term C indicates the viscous damping contribution to the motion of the system. However there are other types of damping models. In this thesis we will describe the "proportional damping" model along with the "viscous damping" model, taking as references Ewins, 2000, García-fogeda and Arévalo-Lozano, 2015, Shabana, 1996, Hidalgo Martinez, 2010.

However it is necessary to remark one important issue. As stated in section 1.4 the current thesis is oriented towards the identification of signals derived from aeroelastic vibrations, and the criterion is based upon JSSG-2006, 1998 and MIL-A-8870C, 1993. Those standards are based on one single damping factor for the critical modes, and hence it is implied that in multimodal systems the damping matrix **C**, **either in the original or in modal coordinates**, after the base change described in equation 2.10, must be diagonal. For that reason our damping model must consider such condition, and the damping solutions described in section 2.3.2 will take into account only the damping models which fulfill such condition.

2.3.2.1 Proportional damping

The current section follows the development on Proportional Damping by Ewins, 2000. Proportional damping considers the damping of the system, in generalized coordinates, as a linear dependent matrix on the mass matrix and stiffness matrix:

$$\mathbf{M} \cdot \frac{d^2\mathbf{x}(t)}{dt^2} + \mathbf{C} \cdot \frac{d\mathbf{x}(t)}{dt} + \mathbf{K} \cdot \mathbf{x}(t) = \mathbf{M} \cdot \frac{d^2\mathbf{x}(t)}{dt^2} + [A\mathbf{M} + B\mathbf{K}] \cdot \frac{d\mathbf{x}(t)}{dt} + \mathbf{K} \cdot \mathbf{x}(t) = 0 \tag{2.14}$$

To solve this system, it is necessary to develop the equations into a more convenient form. Notice that the characteristic of proportional damping is that the damping matrix is a linear combination of the mass **M** and stiffness **K** matrices.

We can introduce modal coordinates in equation 2.14 and reduce the system of equations to an independent set of equations with diagonal matrices. To facilitate the understanding we will develop here only the damping term:

$$[A\mathbf{M} + B\mathbf{K}] \cdot \frac{d\mathbf{x}(t)}{dt} = \mathbf{\Psi}^T [A\mathbf{M} + B\mathbf{K}] \mathbf{\Psi} \cdot \frac{d\mathbf{q}(t)}{dt} = [A\mathbf{M}_r + B\mathbf{K}_r] \cdot \frac{d\mathbf{q}(t)}{dt} = \mathbf{C}_p \cdot \frac{d\mathbf{q}(t)}{dt} \tag{2.15}$$

Since matrices $\mathbf{M}_r$ and $\mathbf{K}_r$ are diagonal, we can define $\mathbf{C}_p$ as the modal proportional damping matrix, also diagonal, and therefore the system of equations can be separated as a set of independent 1 DOF equations in the form:

$$\mathbf{M}_r \cdot \frac{d^2\mathbf{q}(t)}{dt^2} + \mathbf{C}_p \cdot \frac{d\mathbf{q}(t)}{dt} + \mathbf{K}_r \cdot \mathbf{q}(t) = 0 \tag{2.16}$$

Note that since equation 2.16 defines a set of uncoupled 1 DOF equations, we can solve the matrix equation as independent equations (the derivation of the solution can be found in texts like Shabana, 1996 or Boyce and Diprima, n.d.):

$$q_j(t) = A_j \cdot e^{-\zeta_j \omega_{n,j} t} \cdot sin(\omega_{d,j} t + \varphi_j) \tag{2.17}$$

Where φ represents the phase angle and $q_j(t)$ represents the component j of the vector $\mathbf{q}(t)$. Note that these uncoupled set of solutions allows to model the solution of a multiple DOF system with proportional damping to follow JSSG-2006, 1998 and MIL-A-8870C, 1993, and therefore this

kind of damping is specially interesting for aeroelastic phenomena. However it is important to remark that this damping only applies under certain conditions that are not generally fulfilled.

Structural damping The structural damping is a kind of damping that appears under harmonic movements, it is in phase with the airspeed and offsetted 90 degrees with regards to the movement of the mass element.

Soroka, 1949 provides a thorough demonstration of the equations of structural damping, in particular as related to viscous damping, while García-fogeda and Arévalo-Lozano, 2015 provides a very good summary of the equations and derivation of the solution.

To study the structural damping we will consider only 1 DOF. One particular case of proportional damping appears when in equation 2.14 the constant A equals 0 and the constant B is expressed as a constant inversely proportional to the natural frequency ω (the fact that the "constant" is inversely proportional to a variable will be clearer below). We will also introduce the parameters $D = \frac{C_s}{\omega}$, where C_s represents the structural damping factor and ω represents the frequency of the harmonic movement, and $C_s = G \cdot K$ where D is the equivalent viscous damping factor and G the structural damping ratio:

$$\begin{aligned} &M \cdot \frac{d^2x(t)}{dt^2} + D \cdot \frac{dx(t)}{dt} + K \cdot x(t) = 0 \\ &D = \frac{C_s}{\omega} \\ &C_s = G \cdot K \end{aligned} \tag{2.18}$$

Even though equation 2.18 is a homogeneous equation, this doesn't contradict the statement that the structural damping occurs under harmonic movements. Note that in our development we will study the evolution of the system during the transient phase of the movement, meaning that the natural mode has been previously excited at a frequency ω and we are analyzing the behavior of the system immediately after the excitation stops. Please note that the frequency ω above in the structural damping factor D will be selected conveniently, since it will be useful when coincidental with the natural frequency of the system ω_n. Substituting we get:

$$M \cdot \frac{d^2x(t)}{dt^2} + \frac{G}{\omega} \cdot K \cdot \frac{dx(t)}{dt} + K \cdot x(t) = 0 \tag{2.19}$$

Even though the imaginary factors are incompatible with real movements, as a mathematical artifact we will introduce the imaginary constant, to account for the offset of 90 degrees between the velocity of the mass element and its position:

$$M\frac{d^2x(t)}{dt^2} + K(1 + iG)x(t) = 0 \iff \frac{d^2x(t)}{dt^2} + \omega_n^2(1 + iG)x(t) = 0 \tag{2.20}$$

It can be demonstrated (see Soroka, 1949) that the frequency for a structurally damped structure is as follows:

$$\omega_d = \frac{\omega_n}{2}\sqrt{1 + \sqrt{1 + G^2}} \tag{2.21}$$

Where ω_d is the damped vibration (structurally damped), ω_n is the undamped natural vibration as defined by $\omega_n^2 = \frac{K}{M}$ and G is the structural damping constant already defined.

In equation 2.18 we introduced the equivalent damping factor D. The importance of this factor comes because it will allow us to solve equation 2.18 following a viscous damping model, and then

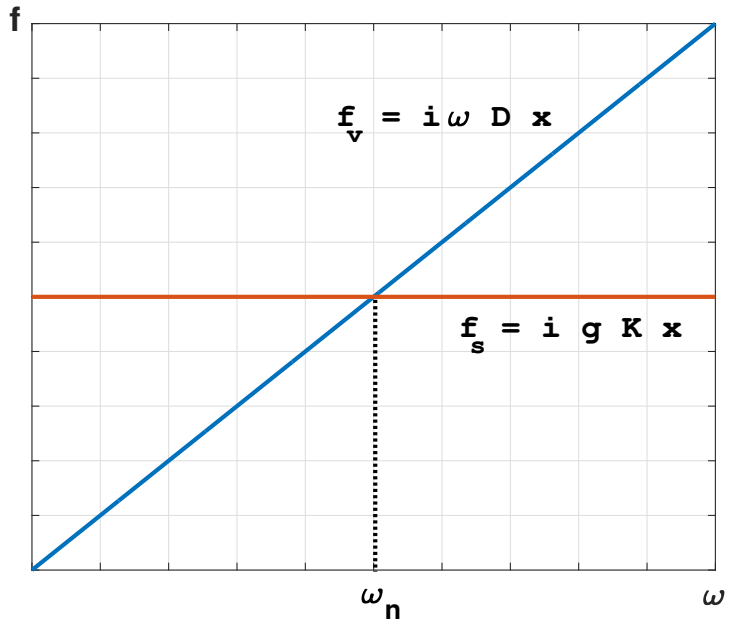

FIGURE 2.1: Comparison between the viscous damping force and structural damping force maximum amplitude. Extracted from García-fogeda and Arévalo-Lozano, 2015

use the conversion between structural damping ratio g and viscous damping ratio ζ. The solution for the viscous damping model will be described in section 2.3.2.2.

$$C_s = G \cdot K = D \cdot \omega \tag{2.22}$$

Assuming an oscillatory motion where the frequency ω coincides with the natural frequency ω_n, the frequency ω in equation 2.22 becomes ω_n, and the following equation can be written:

$$\begin{aligned} C_{cr} &= 2\sqrt{KM} \\ \omega_n &= \sqrt{\frac{K}{M}} \\ D &= G \cdot \omega_n \cdot M \\ \zeta &= \frac{D}{C_{cr}} = \frac{G \cdot \omega_n \cdot M}{2\sqrt{KM}} = \frac{G}{2} \end{aligned} \tag{2.23}$$

It is important to notice that equation 2.23 can only be applied on 1 DOF equations, since assuming that equation 2.3.2.1 was a matrix equation instead of a single degree of freedom equation, the expression for structural damping ratio G (scalar value) multiplies the stiffness matrix $\mathbf{K}$ as a whole, and therefore it can only be applied to systems where each mode has the same structural damping ratio, which is not necessarily true. However, if the system can be separated into independent equations via diagonal matrices, each mode can have its own different structural damping factor.

Notice that the viscous damping force $f_v = i\omega Dx$ is a linear function with frequency ω, while

the structural damping force $f_s = iGKx$ is constant in frequency, as depicted in figure 2.1. However, at the natural frequency ω_n, the damping force is the same for both mechanisms, and therefore it is possible to establish a relationship between both factors as demonstrated in equation 2.23:

$$\zeta = \frac{G}{2} \tag{2.24}$$

As a side note, we must remark that in aeroelasticity applications it is common to employ the imaginary constant i as part of the value of real magnitudes. This is done to indicate a 90 degrees offset between the imaginary magnitude and the reference magnitude, usually the displacement x. For example, figure 2.1 was replicated from García-fogeda and Arévalo-Lozano, 2015, and represents the variation of damping force (maximum amplitude) modeled as structural or viscous damping in imaginary magnitudes. Both result from oscillatory movements and are in phase with the velocity, which itself is offsetted 90 degrees with the displacement

2.3.2.2 Viscous damping

Another different form of damping is the viscous damping. In this case the damping matrix is not necessarily diagonal or proportional to the natural modes of the system, and since it depends on the velocity of each mass element it has a 90 degrees offset with regards to the displacement, in phase with the velocity, similar to the structural damping. We will follow the demonstrations provided by Shabana, 1996 to demonstrate the equations in this chapter.

The classical form of viscous damping for a multi-dimensional movement is the following:

$$\mathbf{M} \cdot \frac{d^2\mathbf{x}(t)}{dt^2} + \mathbf{C} \cdot \frac{d\mathbf{x}(t)}{dt} + \mathbf{K} \cdot \mathbf{x}(t) = 0 \tag{2.25}$$

This equation (assuming one dimension) has the same form as equation 2.18, but instead of depending on a factor D inversely proportional to the frequency ω, the factors of the matrix are constant.

In this case, assuming the most general for for the damping matrix, the solutions depend on the size of the matrices. In case of a single degree of freedom, the solution has a dependency on a single factor, and there is a direct relationship with the structural damping. In case of two degrees of freedom, the damping matrix can be expressed as a linear combination of the mass and stiffness matrices, and therefore can still be expressed as a form of proportional damping. However for more than two degrees of freedom, the general expression for the damping matrix can not always be decomposed in a linear combination of the damping and stiffness matrices.

Single degree of freedom When considering one single DOF, the solution to equation 2.25 considering viscous damping yields the same result as equation 2.17 for proportional damping. The demonstration can be found in Shabana, 1996:

$$x(t) = B \cdot e^{-\zeta\omega_n t} \cdot sin(\omega_d t + \varphi) \tag{2.26}$$

Which is the same equation 2.17 but with viscous damping coefficients.

Two degrees of freedom Shabana, 1996 provides a demonstration of the equations of viscous damping for two degrees of freedom.

The viscous damping model with 2 DOF can in general, assuming a matrix **C** negative-definite, be expressed as a form of proportional damping with complex coefficients as:

$$\begin{aligned} x_1(t) &= A_{11} \cdot e^{-\zeta_1 \omega_{n1} t} \cdot sin(\omega_{d1} t + \varphi_{11}) + A_{12} \cdot e^{-\zeta_2 \omega_{n2} t} \cdot sin(\omega_{d2} t + \varphi_{12}) \\ x_2(t) &= A_{21} \cdot e^{-\zeta_1 \omega_{n1} t} \cdot sin(\omega_{d1} t + \varphi_{21}) + A_{22} \cdot e^{-\zeta_2 \omega_{n2} t} \cdot sin(\omega_{d2} t + \varphi_{22}) \end{aligned} \tag{2.27}$$

Notice that it is not necessary to solve the system for the individual values of A_{ij}, since the problem described in this thesis only needs the expression of the corresponding equations. The values will be calculated empirically from the dataset. This result shows that the relationship between viscous damping and proportional damping (in our case particularized for structural damping) can always be made with one DOF and with restrictions for two DOF. However this fact is not generally true for three degrees of freedom or more. The equations for more than 2 DOF will be developed in section 2.3.2.2 (subsection Multiples degrees of freedom).

In section 2.3.2.2 (subsection Single degree of freedom) it was described the relationship between viscous and structural damping for one single DOF. This conclusion can be extrapolated to multiple DOF in case the damping matrix is diagonal or linearly dependent with the inertial and structural matrices, as described in section 2.3.2.1. In this section it has been demonstrated that when the analysis implies two DOF and the matrices derive from a mechanical system, if the damping matrix is not diagonal, it can always be expressed as a linear combination of the inertial and structural matrices, and therefore in this case it can always be found a relationship between the structural and viscous damping.

Multiple degrees of freedom In the case of more than 2 DOF, the viscous damping vibrational equations can in general be also expressed as a system of 1 DOF equations. However there is a caveat. For 2 DOF the number of elements in the characteristic matrix is the **square of the number of DOF**, so in 2 DOF the number of elements in the characteristic matrix is 4. However, for more than 2 DOF the number of elements is **the square of double the number of DOF** as will be demonstrated below. So for example, for 3 DOF the number of elements in the characteristic matrix is $(2 \cdot 3)^2 = 36$ instead of the expected 9. The development below is described by Shabana, 1996.

Starting with equation 2.25 under a generalized system of coordinates (reproduced here for the sake of clarity):

$$\mathbf{M} \cdot \frac{d^2\mathbf{x}(t)}{dt^2} + \mathbf{C} \cdot \frac{d\mathbf{x}(t)}{dt} + \mathbf{K} \cdot \mathbf{x}(t) = 0 \tag{2.28}$$

We can define the state vector $\mathbf{p}(t)$:

$$\mathbf{p}(t) = \begin{Bmatrix} \mathbf{x}(t) \\ \frac{d\mathbf{x}(t)}{dt} \end{Bmatrix} \tag{2.29}$$

And its derivative $\frac{d\mathbf{p}(t)}{dt}$:

$$\frac{d\mathbf{p}(t)}{dt} = \begin{Bmatrix} \frac{d\mathbf{x}(t)}{dt} \\ \frac{d^2\mathbf{x}(t)}{dt^2} \end{Bmatrix} \tag{2.30}$$

Where $\mathbf{x}(t)$, $\frac{d\mathbf{x}(t)}{dt}$ and $\frac{d^2\mathbf{x}(t)}{dt^2}$ are the generalized coordinates, velocity and acceleration in a particular system.

As described above, the demonstration of the solution of this system of differential equations can be found in Shabana, 1996. Its solution yields:

$$\frac{d\mathbf{p}(t)}{dt} = \begin{Bmatrix} \frac{d\mathbf{x}(t)}{dt} \\ \frac{d^2\mathbf{x}(t)}{dt^2} \end{Bmatrix} = \begin{bmatrix} \mathbf{0} & \mathbf{I} \\ -\mathbf{M}^{-1}\mathbf{K} & -\mathbf{M}^{-1}\mathbf{C} \end{bmatrix} \cdot \begin{Bmatrix} \mathbf{x}(t) \\ \frac{d\mathbf{x}(t)}{dt} \end{Bmatrix} = \mathbf{B} \cdot \mathbf{p}(t) \tag{2.31}$$

Where matrix B is defined as:

$$\mathbf{B} = \begin{bmatrix} \mathbf{0} & \mathbf{I} \\ -\mathbf{M}^{-1}\mathbf{K} & -\mathbf{M}^{-1}\mathbf{C} \end{bmatrix} \tag{2.32}$$

The solution for this matricial equation $\frac{d\mathbf{p}(t)}{dt} = \mathbf{B} \cdot \mathbf{p}(t)$ will yield solutions in the form expressed in equation 2.27 particularized for multiple degrees of freedom, with the caveat that the number of solutions is the one corresponding to displacements and velocities, and hence resulting in double the square of solutions.

$$\begin{aligned} p_i(t) &= \sum_{j=1}^{2n} A_{i,j} \cdot e^{-\zeta_{i,j}\omega_{n\,i,j}t} \cdot sin(\omega_{d\,i,j}t + \varphi_{i,j}) \\ \left.\frac{dp(t)}{dt}\right|_i &= \sum_{k=2n+1}^{4n} A_{i,k} \cdot e^{-\zeta_{i,k}\omega_{n\,i,k}t} \cdot sin(\omega_{d\,i,k}t + \varphi_{i,k}) \end{aligned} \tag{2.33}$$

Where the subindexes $_i$ indicate the component i of the vectors $\mathbf{p}(t)$ and $\frac{d\mathbf{p}(t)}{dt}$ Note however that this solution involves a large amount of matrix inversions. This fact usually brings complications due to ill-conditioned matrices, and even in theoretical systems the errors can lead to wrong solutions, specially in large systems.

2.4 Third term: Elastic forces

The elastic forces $\mathbf{f}_e(t)$ are considered as Hooke's law:

$$\mathbf{f}_e(t) = \mathbf{K} \cdot \mathbf{x}(t) \tag{2.34}$$

This equation will not be derived or discussed in the present thesis, since the demonstration would increase enormously and unnecessarily the complexity of the thesis. Bisplinghoff, Ashley, and Goland, 1963 provides a very thorough demonstration of the elastic equations applied to aeroelasticity, Fung, 2008 provides a simpler demonstration, although more generalistic and less oriented to the deformation of an airfoil. The basic equations from elasticity can be found in textbooks like Gere, 2009.

However it can be mentioned (Shabana, 1996) that the elastic matrix deriving from strain energy, the aforementioned Hooke's Law, can be semidefinite positive, accounting the *semidefinite* portion from the fact that the system can have rigid body modes. These cases derive from the eigenvalues of the system equal to zero. In these cases, the existence of a zero eigenvalue means that there exists one particular direction (associated eigenvector) on which the strain energy of the system doesn't increase with the movement, therefore being a rigid body movement.

2.5 Fourth term: Aerodynamic forces

The current section will demonstrate the relationship between the different parameters of movement of the airfoil and the flutter mechanism. To achieve such objective it is necessary to have a

basic knowledge of the Navier-Stokes equations applied to aerodynamics, including the derivation based on the theory of potential flow and different hypotheses and theories. This will allow us to understand the basis of steady aerodynamics, which also will be the foundation stone for unsteady aerodynamics, the final objective of this section.

2.5.1 Steady Aerodynamics

Steady aerodynamic equations for complete wings are out of the scope of this thesis for reasons expressed further on, therefore in this section we will limit the expression to the 2-D airfoil steady incompressible aerodynamic equations as a basis to understand the unsteady aerodynamics in section 2.5.2.

The demonstrations on this section will be based upon the texts by Meseguer Ruiz and Sanz Andrés, 2010; Bisplinghoff, Ashley, and Goland, 1963; Anderson, 2007.

Before starting the development of the present section, it is necessary to declare the following assumptions:

Assumption 1. *The air will be considered an incompressible subsonic inviscid flow.*

This statement is controversial, considering that one of the main contributors to the lift of the airfoil is due to the existence of viscosity, which is responsible for the existence of boundary layer, drag force, wake, etc. To account for the viscosity effects, we will introduce assumption 2. The subsonic condition is coherent with the results and analysis presented in this thesis. All the datasets analyzed derive from subsonic flight flutter tests, and therefore the assumption poses no controversy. At last, regarding the "incompressible" condition, many of the datasets analyzed derive from high subsonic regime (close to the transonic region), and therefore it is incoherent not to consider compressibility effects. These conditions will not be analyzed. Meseguer Ruiz and Sanz Andrés, 2010 and Anderson, 2007 provide some analytical basis to start reaching conclusions on the compressibility effects, based on the incompressible subsonic equations by the modification of the pressure coefficient C_p based on the Mach number (the *Prandtl-Glauert compressibility correction*), and further more a refinement on the correction based on experimental results. All in all, the equations for aerodynamic forces and moments eventually depend on he same factors as the incompressible equations, and therefore dedicating one chapter to describe these results will needlessly add complexity to the thesis.

Assumption 2. *The airfoil will artificially produce a rotational potential, which will account for the effects of viscosity and boundary layer.*

This is common practice for these kind of derivations.

Assumption 3. *The control volume will exclude the airfoil itself, the boundary layer and the wake.*

This assumption complements assumption 2. The boundary layer and wake are the areas where the viscosity needs to be taken into account. Leaving those areas out of the control volume and introducing artificial mechanisms to replicate the effects of viscosity (introduce an artificial circulation where needed, Kutta's condition...) will enormously simplify the equations.

Assumption 4. *The equations of motion will be considered in a stationary steady state condition, without changes in altitude, airspeed or angle of attack.*

This is necessary to account for the epigraph "Steady Aerodynamics".

Assumption 5. *The control volume will extend between minus infinite to plus infinite (aerodynamically speaking) in the flight direction.*

This assumption will account for the necessity to start in undisturbed conditions of the airflow.

Assumption 6. *The air current starts from a reservoir of static irrotational undisturbed air and the stream lines are parallel and uniform in plus/minus infinite ($\nabla \times \mathbf{v}|_{-\infty/+\infty} = 0$), where* $\mathbf{v}$ *represents the airspeed vector.*

This assumption comes as a consequence of **Bjernes-Kelvin's theorem**. The summation of wake vorticity and circulation around the airfoil must be zero ($\Gamma_a + \Gamma_w = 0$), where Γ represents the circulation and the subindexes $_a$, $_w$ represent the airfoil and wake respectively. The demonstration of this theorem is out the scope of this thesis, but can be found in Anderson, 2007 pages $316 - 319$.

Assumption 7. *The heat transfer is negligible (adiabatic mechanism), and therefore there is no need to consider energy dissipation in form of temperature or (assumption 3) viscosity.*

The demonstration is beyond of the scope of this thesis, but can be found in Meseguer Ruiz and Sanz Andrés, 2010, pages $10, 11$.

Assumption 8. *Internal fluid viscosity forces and buoyancy (floatability) forces can be ignored.*

A demonstration for the validity of this assumption can be found in Meseguer Ruiz and Sanz Andrés, 2010, pages $8, 9$.

2.5.1.1 Euler reference system

In fluid mechanics there are classically two main reference systems, the Lagrange reference system and the Euler reference system.

The Lagrange reference system is usually employed when we are interested in knowing the evolution of a given fluid particle along a trajectory (space and time evolution). A comparison can be made with a person sitting on a boat which moves with the water and studying the evolution of the water along the river. On the other hand, the Euler reference system is used when the interest is not related to the evolution of the fluid particle but the influence of an obstacle over the fluid. The comparison here is the observer sat in the riverside while studying the influence of a bridge pillar over the river fluid particles.

In this thesis we will employ the Euler reference system.

2.5.1.2 Substantial derivative

Along this thesis, the concept of *substantial derivative* will appear in numerous occassions.

The substantial derivative is represented as $\frac{D}{Dt}$, and is applicable whenever there is a time derivative of any variable depending both on time and spatial coordinates, and is defined as (for a generic scalar magnitude $\theta(x, y, z, t)$):

$$\begin{aligned} &\frac{D\theta(x,y,z,t)}{Dt} = \frac{\partial\theta(x,y,z,t)}{\partial t} + \frac{\partial\theta(x,y,z,t)}{\partial x(t)}\frac{\partial x(t)}{\partial t} + \frac{\partial\theta(x,y,z,t)}{\partial y(t)}\frac{\partial y(t)}{\partial t} + \frac{\partial\theta(x,y,z,t)}{\partial z(t)}\frac{\partial z(t)}{\partial t} \iff \\ &\iff \frac{D\theta(x,y,z,t)}{Dt} = \frac{\partial\theta(x,y,z,t)}{\partial t} + \mathbf{v}\cdot\nabla\theta(x,y,z,t) \end{aligned} \tag{2.35}$$

Where $\mathbf{v}$ represents the velocity vector.

2.5.1.3 General equations

Under the assumptions stated above, we will present the Navies-Stokes equations, which are the main equations for modeling fluid dynamics, equivalent to the Maxwell equations for electromagnetism.

The equations that will be considered in the present section will be limited to the following set (the demonstration is out of the scope of this thesis, but can be found in White, 2016):

$$\frac{D\rho}{Dt} + \rho\nabla \cdot \mathbf{v} = 0 \tag{2.36}$$

$$\rho\frac{D\mathbf{v}}{Dt} = -\nabla p \tag{2.37}$$

Where ρ represents the air density and p represents the air static pressure, both as a scalar fields ($\rho, p = \rho, p(x, y, z, t)$), and $\mathbf{v}$ represents the air velocity vector as a vector field ($\mathbf{v} = \mathbf{v}(x, y, z, t)$). These three variables are a function of time t and the three spatial coordinates x, y, z.

Equation 2.36 represents the mass conservation equation, also called "continuity" equation, and represents the first of the Navier-Stokes equations. The physical meaning of this equation is that considering a control volume, say a pipe opened through both extremes with its section changing arbitrarily, the mass of air per time unit flowing into the tube must be the same as the mass flowing out.

Equation 2.37 represents the momentum conservation equation, and it considers all the factors that may exert any influence on the system to change its momentum after having been applied the assumptions stated in section 2.5.1.

The third Navier-Stokes equation, the conservation of energy, as stated in assumption 7 can be neglected, since there will be no external contribution of sources adding or subtracting energy, and therefore will be a linear combination of equations 2.36 and 2.37. Of course sources of energy like radiation or chemical reactions, like for example analyzing reentry of space vehicles, is completely out of the scope of this thesis and have not even been included in the general energy equations.

At last it may be possible to consider the second principle of Thermodynamics and analyze the exchange of entropy. For the present effort it will suffice to say that we can assume the entropy of the system to be constant, the system can be considered isoentropic without demonstration. As a reference Meseguer Ruiz and Sanz Andrés, 2010 demonstrates the isoentropic assumption. This case must be considered when analyzing hypersonic flow and reentry of space vessels, like the Space Shuttle or the X-52. However that range of altitudes and airspeeds are far beyond the scope of the present thesis.

2.5.1.4 Velocity potential

One important concept to start studying the aerodynamics over an airfoil is the velocity potential. Being the airspeed field around an airfoil a vector field, we will apply complex potential theory and try to model each objects in the flowfield as combinations of complex potential singularities.

As a summary of the upcoming section we will define a potential function for the airspeed $\Phi(x, z)$, and will create the airfoil boundary as a combination of potential perturbations in the airflow (sources, sinks, doublets and vortices). These considerations, along with the Navier-Stokes equations, will return a theory suitable for calculating the lift on an airfoil with reasonable accuracy, assuming that the flow is laminar and incompressible and the airfoil has a low angle of attack (in general the flow remains attached to the airfoil in most of its surface). The demonstrations in the current and upcoming subsections can be found in Meseguer Ruiz and Sanz Andrés, 2010.

Theorem 2.5.1. *The airspeed function* $\mathbf{v}$ *derives from a velocity potential field* Φ

The demonstration is out of the scope of this thesis, but will be reproduced in appendix A.1.

The consequence of this Theorem is equation 2.38:

$$\nabla \times \mathbf{v} = 0 \iff \mathbf{v} = \nabla\Phi \implies u = \frac{\partial\Phi}{\partial x},\ w = \frac{\partial\Phi}{\partial z} \tag{2.38}$$

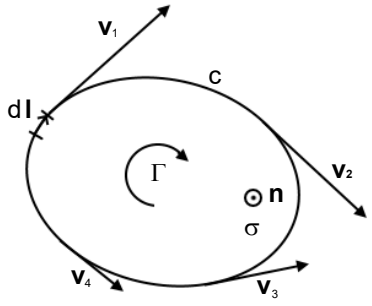

FIGURE 2.2: Velocity circulation around a closed curve

Where Φ represents the velocity potential, u, w are respectively the horizontal and vertical local components of the airspeed $\mathbf{v}$ and x, z represent the cartesian components, as described in figure 2.3. Note also that we can consider regular derivatives in x, z (as opposed to partial derivatives) since as we already demonstrated, the variables u and w don't depend on time t (stationary aerodynamics hypothesis).

2.5.1.5 Stream function

The next step is to define the stream function $\Psi(x, z)$. The stream lines are the locus of the velocity vector tangents.

Mathematically the stream lines $\mathbf{s}(x, z)$ can be calculated as follows:

$$\begin{aligned} d\mathbf{s} &= d\mathbf{s}(dx, dz) \\ \mathbf{v} &= \mathbf{v}(u, w) \end{aligned}$$

By definition of cross product, for both vectors being parallel it is sufficient that the cross product equals zero, and as defined above, if we calculate the cross product of the stream lines ($\mathbf{s}(x, z)$, tangent to the velocity) and the velocity, we end up with a scalar field:

$$d\mathbf{s} \times \mathbf{v} = 0 \iff \frac{dz}{dx} = \frac{w}{u} \iff udz - wdx = 0 \tag{2.39}$$

And integrating, by definition of $\Psi(x, z)$:

$$\Psi(x, z) = uz - wx = C \tag{2.40}$$

Where C is an integration constant. The stream function Ψ has the following properties:

$$\begin{aligned} \frac{\partial \Psi}{\partial z} &= u \\ \frac{\partial \Psi}{\partial x} &= -w \end{aligned} \tag{2.41}$$

2.5.1.6 Relationship between Φ and Ψ. Complex potential

Notice that the following equations are true from equations 2.38 and 2.40:

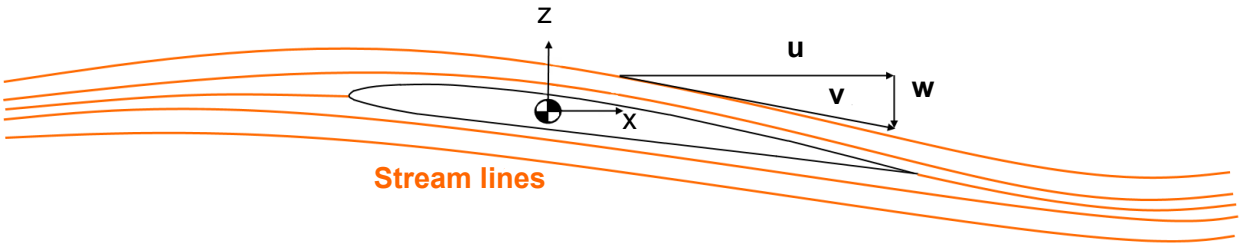

FIGURE 2.3: Streamlines around an airfoil

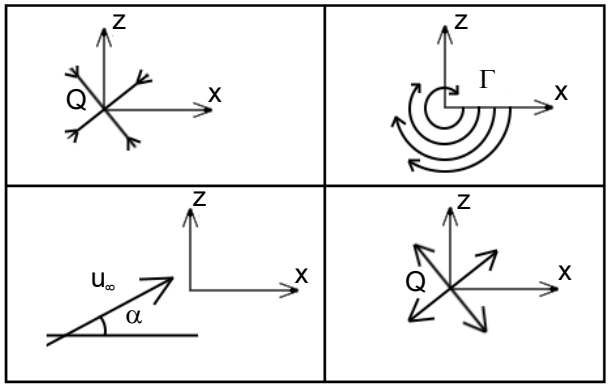

FIGURE 2.4: Different potential flows examples. Upper left a sink example of intensity Q. Upper right a vortex example of intensity Γ. Lower left an example of uniform flow with velocity u_∞. Lower right an example of source with intensity Q

$$d\Psi = udz - wdx = 0 \tag{2.42}$$

$$d\Phi = udx + wdz = 0 \tag{2.43}$$

Analyzing equations 2.42 and 2.43, it can be inferred that Φ and Ψ are both orthogonal functions:

$$\Psi \perp \Phi \tag{2.44}$$

And since function Ψ represents the stream function, Φ shall represent equipotential curves. That been said, it is possible to compose a complex function f for the potential:

$$f(s) = \Phi + i\Psi \tag{2.45}$$

Where f is the complex potential function and s is the complex variable associated, defined as $s = x + iz$. This complex potential allows to define objects in the undisturbed potential airflow equation by combination of different singularities, like sources, sinks, doublets and vortices. **Note not to confuse the vector variable s, representing the streamlines function, with the scalar variable s, representing a generic complex variable**.

Complex potential: Uniform flow The definition for the complex potential of a uniform flow is the following:

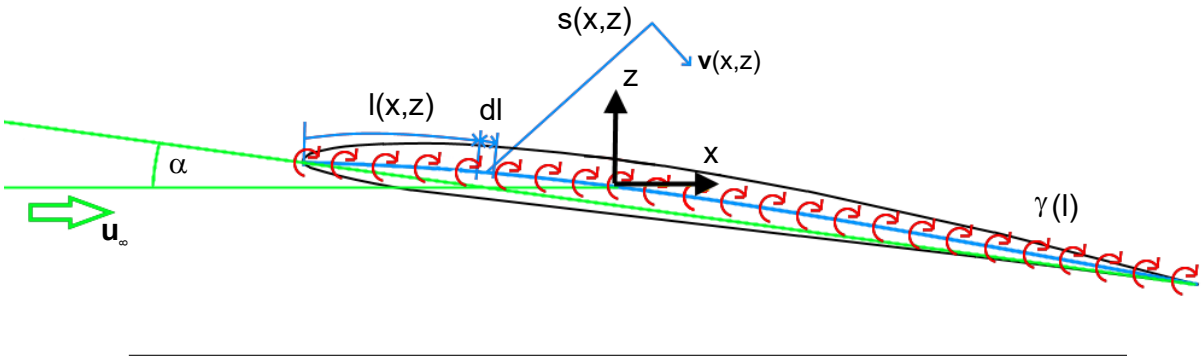

FIGURE 2.5: Vortex sheet

$$f(s) = u_\infty e^{-i\alpha} s \tag{2.46}$$

Where α is the angle of attack and u_∞ is the airflow current. An example of an uniform current flow can be seen in figure 2.4.

Complex potential: Source and sink The mathematical definition for a source and sink with intensity Q centered at a point s_0 is as follows:

$$f(s) = \pm\frac{Q}{2\pi} Ln(s - s_0) \tag{2.47}$$

Where the difference between sources and sinks comes from the sign of the intensity, positive for sources and negative for sinks. An example of sources and sinks can be seen in figure 2.4

Complex potential: Vortices In the case of vortices, the intensity of the vortex is defined by Γ. In this case, the definition of a vortice centered at s_0 comes by:

$$f(s) = \frac{i\Gamma}{2\pi} Ln(s - s_0) \tag{2.48}$$

The sign criterion is positive clockwise, coincidental with a right handed trihedral for the y axis. an example can be seen in figure 2.4.

A particular case of the vortices potential is the vortex sheet. The vortices are distributed along a line uniformly, and instead of having a single intensity Γ there is a intensity density γ per length unit. In this case the velocity expression for a vortex sheet on an airfoil camber, as defined in figure 2.5, at a point p for a vortex sheet of length L is as follows:

$$\mathbf{v}(s) = -\frac{i}{2\pi} \int_0^L \frac{\gamma(l)dl}{|l(s) - p(s)|} \tag{2.49}$$

A particular case of equation 2.49 is when the camber coincides with the x axis, has length L and the point p is placed on the vertex sheet, is as follows:

$$\mathbf{w} = -\frac{i}{2\pi} \int_0^L \frac{\gamma(l)dl}{p - l} \tag{2.50}$$

2.5.1.7 Euler-Bernouilli's equation

Once defined the velocity potential Φ, we can simplify the conservation of momentum equation 2.37. Euler-Bernouilli's equation is one of the most important equations in aerodynamics, since it relates the airspeed modulus variation with the pressure variation, which ultimately is responsible for lift.

The derivation of the current section can be found in Anderson, 2007 and Meseguer Ruiz and Sanz Andrés, 2010, and will be reproduced here given the relevance of this equation.

From equation 2.37, developing the substantial derivative of the velocity we can derive:

$$\frac{D\mathbf{v}}{Dt} = \frac{\partial \mathbf{v}}{\partial t} + \mathbf{v}\cdot\nabla\mathbf{v} = \frac{\partial \mathbf{v}}{\partial t} + \frac{1}{2}\nabla(\mathbf{v}\cdot\mathbf{v}) = -\frac{1}{\rho}\nabla p = -\nabla\int\frac{dp}{\rho} \tag{2.51}$$

And introducing the definition of the potential of velocities $\mathbf{v} = \nabla\Phi$ into equation 2.51 yields:

$$\nabla\left[\frac{\partial\Phi}{\partial t} + \frac{1}{2}|\nabla\Phi|^2 + \int\frac{dp}{\rho}\right] = 0 \iff \frac{\partial\Phi}{\partial t} + \frac{1}{2}|\nabla\Phi|^2 + \int\frac{dp}{\rho} = C_1(t) \tag{2.52}$$

Since we defined in assumption 1 the fluid as incompressible, the density is independent to the pressure, and therefore we can define the following relationship from equation 2.52 for unsteady flow:

$$\frac{\partial\Phi}{\partial t} + \frac{1}{2}|\nabla\Phi|^2 + \frac{p}{\rho} = C_2(t) \tag{2.53}$$

And likewise for steady flow:

$$\frac{1}{2}\rho_\infty|\nabla\Phi|^2 + p = C_3 = \frac{1}{2}\rho_\infty u_\infty^2 + p_\infty \tag{2.54}$$

Which constitutes the popular form of the Euler-Bernouilli equation.

The importance of the right hand term of equation 2.54 is paramount. It is applicable for the whole trajectory of streamlines, so known the static pressure and velocity at infinity (flight speed of the airfoil and static pressure of the air at that altitude) it is possible to know the constant C_3, and from there knowing the airspeed at a given point it is possible to know the static pressure at that point. Hence, knowing the velocity vector field around the airfoil it is possible to know the pressure field and from there calculate lift. Now the problem is reduced to knowing the airspeed field around the airfoil.

2.5.1.8 Lift and non-dimensional coefficients. Kutta - Joukowski Theorem

Bernouilli's equation describes an equivalence between air static pressure and airspeed. We can start getting a physical meaning out of equation 2.54. The derivation of this section can be found in Meseguer Ruiz and Sanz Andrés, 2010.

The term p_∞ represents the stream's static pressure. The next term has also pressure dimensions, $\frac{1}{2}\rho_\infty u_\infty^2$, and is dependent upon stream pressure ρ and airspeed u_∞. This term is called dynamic pressure Q_∞.

Now we must understand that the dynamic pressure can be understood as a reservoir for energy derived from the static pressure, while the static pressure is the actual contributor to the lift of the airfoil. Hence, we can define the pressure coefficient $C_p(\zeta)$ for a point ζ in the x dimension of the chord and for the upper and lower sides of the airfoil as follows:

$$C_p^{u,l}(\zeta) = \frac{p_u^{u,l}(\zeta) - p_\infty}{\frac{1}{2}\rho_\infty u_\infty^2} = \ldots = 1 - \left(\frac{|\mathbf{v}|}{u_\infty}\right)^2 \tag{2.55}$$

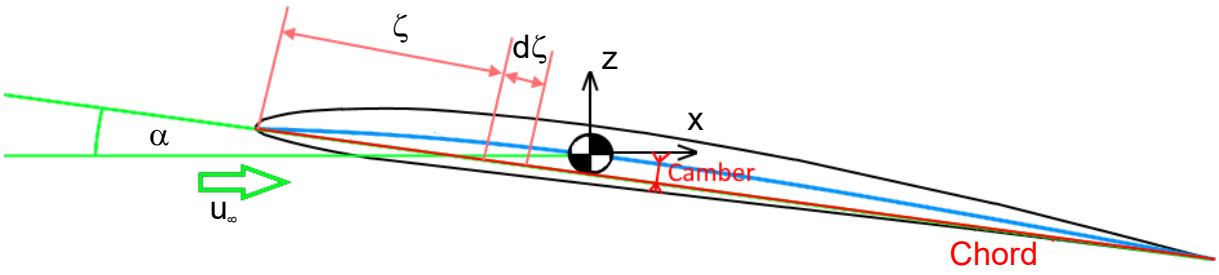

FIGURE 2.6: Airfoil definitions. The camber is defined as the distance between the mean chamber line and the chord, the mean camber line c is the line which separates equally the upper side of the airfoil and the lower side of the airfoil, depicted in blue, the chord is the straight line that joins the the leading edge and the trailing edge, depicted as a red line. The undisturbed airflow speed is u_∞, the angle of attack is the angle between the chord and the airflow airspeed vector. Dimension ζ along the chord indicates the distance from the leading edge to the chord element $d\zeta$

Notice that the pressure coefficient is defined for a given point, but it also needs to be calculated for the upper and lower sides of the airfoil, since in both positions the pressure coefficient may be different. To calculate the lift coefficient C_L, it is necessary to integrate the pressure coefficient along the chord and consider the upper and lower sides of the airfoil (indicated by the superindex ^{u} and ^{l} respectively):

$$C_L = \frac{1}{c}\left[\int_0^c C_p^l d\zeta - \int_0^c C_p^u d\zeta\right] \tag{2.56}$$

From the lift coefficient we can calculate lift per span unit by definition:

$$L_s = \frac{1}{2}\rho_\infty S\, u_\infty^2\, C_L \tag{2.57}$$

Where S is the surface per span unit of the lifting surface.

Once the lift per span unit is defined, we can introduce another important theorem, the *Kutta - Joukowski's theorem*.

Theorem 2.5.2 (Kutta - Joukowski's Theorem)**.** *The lift over an airfoil can be calculated by calculating the velocity distribution over a closed curve engulfing the airfoil, and the expression for lift per span unit over an airfoil with a circulation distribution* Γ *is as follows:*

$$L_s = \rho_\infty u_\infty \Gamma \tag{2.58}$$

The demonstration of the Kutta - Joukowski's theorem is out of the scope of this thesis. However Meseguer Ruiz and Sanz Andrés, 2010 provides a very good demonstration in pages 46-49.

The importance of the Kutta - Jukowski's theorem is that it directly relates the global circulation of the airfoil with the lift, regardless of the angle of attack, thickness, curvature or lifting surface per span unit. These parameters are embedded into the final solution for the circulation. Therefore **it is possible to know the lift of an airfoil indirectly, by knowing the density, flight speed and the circulation of the wake**.

This conclusion might seem unrealistic, since appears to be much easier to calculate the circulation around an airfoil than the circulation around the wake. However, this conclusion will be crucial for the upcoming sections.

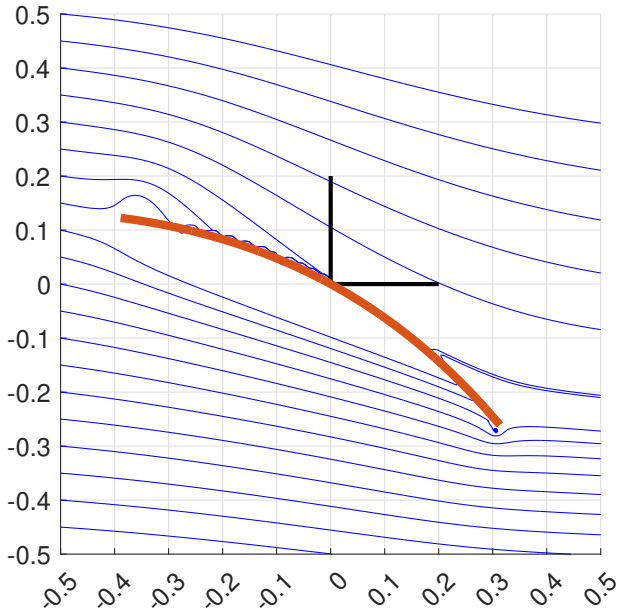

FIGURE 2.7: Airfoil camber mean line defined by a vortex and doublets distributed over the curve

2.5.1.9 Kutta condition

We can find further information for this section in Anderson, 2007. Although Kutta-Joukowski theorem 2.5.2 gives a very simple tool to calculate lift, which basically indicates that the total circulation around the airfoil is directly proportional to the total lift, it is necessary to be able to accurately estimate (calculate actually) the circulation around a cylinder (or associated airfoil), which implies to know the field of velocities.

Now we face a problem. Remember that we are working under the assumption that the viscosity is negligible. This means that under a potential flow the stangation points can be anywhere on the airfoil, since there is no mechanism to model the detachment of the airflow. For example, we can imagine an airfoil perfectly perpendicular to the airstream ($\alpha = \pi/2$). In such situation there should be two different stagnation points, one approximately in the middle of the chord line and the other opposite to it in the upper side of the airfoil. This may seem an extreme case, but in general this is the standard behavior under potential flow. A sharp trailing edge won't prevent the airflow to perfectly and smoothly bend around it. Figure 2.7 shows the behavior of such flow, with two stagnation points, one in the lower and one in the upper side of the airfoil (both streamlines in black), which is blatantly incorrect.

To prevent this situation, Kutta proposed a condition indicating that:

1. The circulation Γ must be such that the flow leaves the trailing edge smoothly
2. If the trailing edge is finite, then the trailing edge is a stagnation point, the velocities V_1 and V_2 are zero and therefore $\gamma_{t.e.} = 0$. See figure 2.8
3. If the trailing edge is cusped, then the velocities V_1 and V_2 must be equal in magnitude and direction: $\mathbf{v}_1 = \mathbf{v}_2$. See figure 2.9. Since $\gamma = V_2 - V_1$, this condition is also reduced to $\gamma_{t.e.} = 0$.

The Kutta condition was paramount to the advance of aerodynamics, since currently the potential flow theory is the basis for many finite element algorithms.

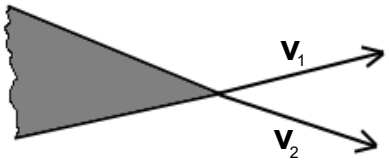

FIGURE 2.8: Trailing edge ending with a finite angle

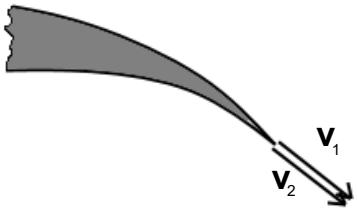

FIGURE 2.9: Trailing edge ending in cusp

2.5.1.10 Thin airfoil theory

The derivation of this section can be found in Anderson, 2007.

Currently we have enough knowledge to calculate lift around an airfoil. First as steady aerodynamics (current section), where the airfoil keeps a constant angle of attack and the vertical displacement of the airfoil is zero, and later (section 2.5.2) during an unstable phase, where the angle of attack varies due to the rotation and vertical displacement of the airfoil.

The thin airfoil theory will be based in the following constraints to model the airfoil (see figure 2.10 for the definitions):

1. The airfoil seen from afar can be simplified as a vortex sheet over the camber (mean line between the upper and lower side of the airfoil).
2. The camber is a streamline. To reach this constraint we will define the velocity on the surface of the camber as tangent to the camber (the normal velocity perpendicular to the camber equals zero): $u_{\infty,n} + w' = 0$.
3. The thickness of the airfoil will not be directly incorporated. Its influence will be incorporated into the value of $\gamma(l)$.
4. The kutta condition will be incorporated forcing the trailing edge circulation value to be zero $\gamma_{t.e.} = 0$.
5. Although the camber shape will be considered as $\frac{dz}{dx}$, the distance between the camber and the chord is small and we can make the approximation $w'(l) \approx w(x)$. The velocity normal to the chord will be zero instead of the velocity normal to the camber.

Figure 2.10 defines the nomenclature used in the thin airfoil theory. β angle is the angle between the chord line and the x axis: $\beta = atan\left(-\frac{dz}{dx}\right)$. The velocity $u_{\infty,n}$ is the free stream velocity

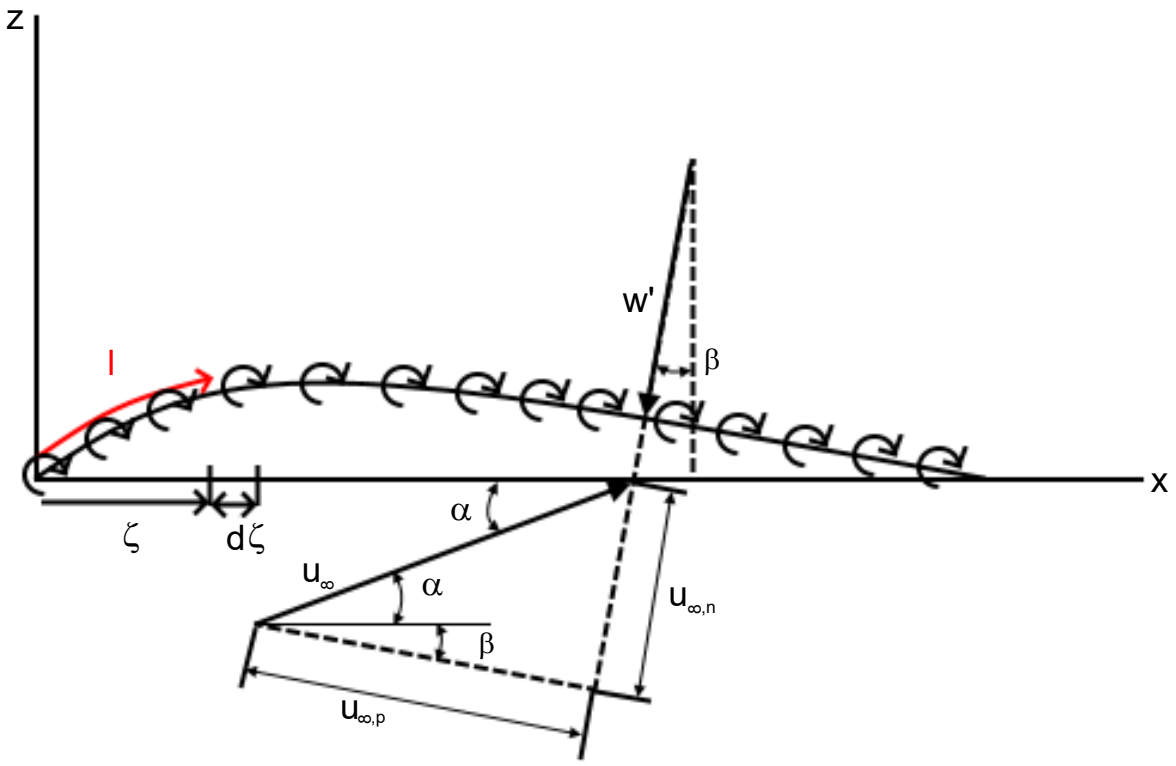

FIGURE 2.10: Thin airfoil theory nomenclature

normal to the camber, ζ is the distance over the chord, $d\zeta$ its differential element and w' is the velocity induced by the vortex sheet normal to the camber, although as said above it will simplified to the velocity normal to the x axis w.

We will start by modeling the camber as a streamline. To reach that goal, we will apply the constraints above, model the camber as a vortex sheet and identify the contributors to the velocity perpendicular to the camber, say the normal contribution from the undisturbed airflow $u_{\infty,n}$ and the perpendicular vortex induced velocity w', and force them to sum zero.

First we will define the velocity normal to the camber w' from equation 2.50

$$w' \approx -\frac{1}{2\pi}\int_0^L \frac{\gamma(\zeta)d\zeta}{x-\zeta} \tag{2.59}$$

And the free stream velocity normal to the camber:

$$u_{\infty,n} = u_\infty \cdot sin\left(\alpha + atan\left(-\frac{dz}{dx}\right)\right) \approx u_\infty \cdot \left(\alpha - \frac{dz}{dx}\right) \tag{2.60}$$

With these constraints into account we can calculate the velocity field:

$$u_{\infty,n} + w' = 0 \tag{2.61}$$

And applying the previous approximations:

$$\frac{1}{2\pi}\int_0^L \frac{\gamma(\zeta)d\zeta}{x-\zeta} \approx u_\infty \cdot \left(\alpha - \frac{dz}{dx}\right) \tag{2.62}$$

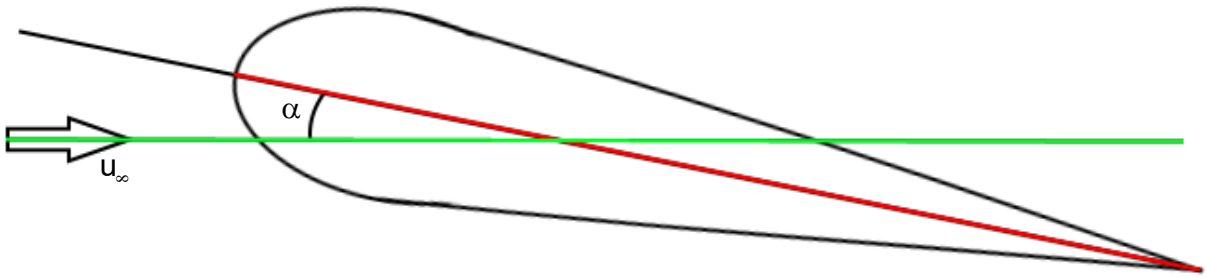

FIGURE 2.11: Symmetric airfoil sample

Equation 2.62 constitutes the fundamental equation for the thin airfoil theory, and is an integral equation where the unknown term is the vorticity density γ, which is needed to calculate lift applying the Kutta-Joukowski theorem 2.5.2. **This equation can be summarized by a simple statement: The camber is a streamline of the flow.**

To solve γ we can identify two different cases, corresponding to the two different airfoil models defined by the kutta condition, the symmetric and the cusped airfoil. Both will have a different definition of $\frac{dz}{dx}$, and therefore the solution of the circulation will be different.

Symmetric airfoil The case of a symmetric airfoil (figure 2.11) implies that the term $\frac{dz}{dx} = 0$ in equation 2.62:

$$\frac{dz}{dx} = 0 \iff \frac{1}{2\pi}\int_0^L \frac{\gamma(\zeta)d\zeta}{x-\zeta} = u_\infty \cdot \alpha \tag{2.63}$$

To calculate this integral is convenient to transform ζ into θ with the following relation:

$$\zeta = \frac{L}{2}(1 - cos\,\theta) \iff d\zeta = \frac{L}{2} sin\,\theta\, d\theta \tag{2.64}$$

Where θ is a variable that defines the position over the cord, centered in $L/2$. Notice that the points $\zeta = 0$ and $\zeta = L$ correspond to the points $\theta = 0$ and $\theta = \pi$. For the point x in equation 2.63 we can establish point θ_0:

$$x = \frac{L}{2}(1 - cos\,\theta_0) \tag{2.65}$$

And equation 2.63 becomes:

$$\frac{1}{2\pi}\int_0^\pi \frac{\gamma(\theta)\, sin\,\theta\, d\theta}{cos\,\theta - cos\,\theta_0} = u_\infty \cdot \alpha \tag{2.66}$$

Equation 2.66 constitutes an inhomogeneous Fredholm integral equation of the first kind, whose solution demonstration is beyond the scope of this thesis, but can be found in Wazwaz, 2011. Its solution is as follows:

$$\gamma(\theta) = 2\,\alpha\, u_\infty \frac{1 + cos\,\theta}{sin\,\theta} \tag{2.67}$$

Once the solution to γ is known, we have the distribution of vortices along the camber. Remember that in order to be able to calculate lift we need to calculate first the global circulation

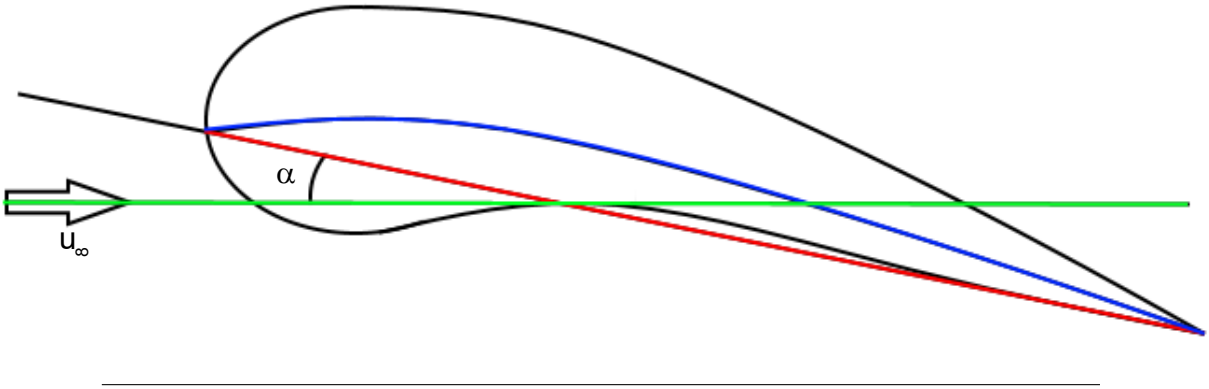

FIGURE 2.12: Cambered airfoil sample

around a closed line around the airfoil (Kutta - Joukowski's theorem 2.5.2). Now we can calculate the global circulation Γ simply integrating the vortices distribution:

$$\Gamma = \int_0^L \gamma(\zeta)\, d\zeta = \frac{L}{2} \int_0^\pi \gamma(\theta)\, d\theta \tag{2.68}$$

Incorporating the solution of γ (equation 2.67):

$$\Gamma = \alpha\, L\, u_\infty \int_0^\pi (1 + cos\,\theta)\, d\theta = \pi\, \alpha\, L\, u_\infty \tag{2.69}$$

Now substituting equation 2.69 into the Kutta-Joukowski theorem (2.5.2), the lift per span unit is:

$$L_s = \rho_\infty\, u_\infty\, \Gamma = \pi\, \alpha\, L\, \rho_\infty\, u_\infty^2 \tag{2.70}$$

Note that this result indicates that the lift per span unit for a symmetric airfoil depends linearly on the angle of attack. This result is coherent with experimental data (Anderson, 2007) under the restrictions imposed to the thin airfoil model.

We can also calculate the aerodynamic moment per span unit about the leading edge, by integrating the lift contribution along the cord multiplied by the distance along the cord ζ (the integration is trivial):

$$M_{s,le} = -\int_0^L \zeta dL_s = -\frac{1}{4}\rho_\infty u_\infty^2 L^2 \pi\alpha \tag{2.71}$$

As for the lift, the aerodynamic moment about the leading edge is a function linearly dependent on the angle of attack.

Cambered airfoil The cambered airfoil solution is more complicated than the symmetric airfoil. In this case it is not possible to simplify the integral equation, and will be a second kind inhomogeneous Fredholm equation, also demonstrated in Wazwaz, 2011. We will follow the same reasoning until equation 2.66, but carrying the term $\frac{dz}{dx}$:

$$\frac{1}{2\pi} \int_0^\pi \frac{\gamma(\theta)\, sin\,\theta\, d\theta}{cos\,\theta - cos\,\theta_0} = u_\infty \cdot \left(\alpha - \frac{dz}{dx}\right) \tag{2.72}$$

In this case the solution for equation 2.72 is not so simple as in the symmetric airfoil case. Instead it necessary to expand in power series the solution with coefficients depending on α and $\frac{dz}{dx}$.

$$\gamma(\theta) = 2\,u_\infty \left(A_0 \frac{1+cos\,\theta}{sin\,\theta} + \sum_{n=1}^{\infty} A_n\, sin\, n\theta \right) \tag{2.73}$$

This equation has as unknowns the parameters of the series expansion A_0 and A_n, and it is necessary to calculate both in order to have a solution for $\gamma(\theta)$, which will be done in the following paragraphs.

Substituting equation 2.73 into equation 2.72:

$$\frac{1}{\pi}\int_0^\pi \frac{A_0(1+cos\,\theta)}{cos\,\theta - cos\,\theta_0}\,d\theta + \frac{1}{\pi}\sum_{n=1}^{\infty}\int_0^\pi \frac{A_n sin\, n\theta\, sin\,\theta}{cos\,\theta - cos\,\theta_0} d\theta = \alpha - \frac{dz}{dx} \tag{2.74}$$

Again, the solution of equation 2.74 is beyond the scope of this thesis. Instead the solution already integrated is as follows:

$$A_0 - \sum_{n=1}^{\infty} A_n\, cos\, n\theta_0 = \alpha - \frac{dz}{dx} \iff \frac{dz}{dx} = (\alpha - A_0) + \sum_{n=1}^{\infty} A_n\, cos\, n\theta_0 \tag{2.75}$$

Notice that $\frac{dz}{dx}$ is known (we know the geometry of our airfoil), α is known and θ_0 is a substitution for x through equation 2.64. Also notice that the expression in equation 2.75 for $\frac{dz}{dx}$ is a Fourier series expansion, with the zero term $\alpha - A_0$ and the rest of the terms $\sum_{n=1}^{\infty} A_n\, cos\, n\theta_0$. Hence, we can state:

$$\alpha - A_0 = \frac{1}{\pi}\int_0^\pi \frac{dz}{dx} d\theta_0 \iff A_0 = \alpha - \frac{1}{\pi}\int_0^\pi \frac{dz}{dx} d\theta_0 \tag{2.76}$$

$$A_n = \frac{2}{\pi}\int_0^\pi \frac{dz}{dx} cos\, n\theta_0\, d\theta_0 \tag{2.77}$$

Now we can combine equations 2.73, 2.76 and 2.77 to get the solution for $\gamma(\theta)$:

$$\gamma(\theta) = 2u_\infty \left(\left(\alpha - \frac{1}{\pi}\int_0^\pi \frac{dz}{dx} d\theta_0 \right) \frac{1+cos\,\theta}{sin\,\theta} + \sum_{n=1}^{\infty} \left(\frac{2}{\pi}\int_0^\pi \frac{dz}{dx} cos\, n\theta_0\, d\theta_0 \right) sin\, n\theta \right) \tag{2.78}$$

For the sake of simplicity, we will express the circulation Γ as a function of the parameters A_0 and A_n:

$$\Gamma = L\,u_\infty \left[A_0 \int_0^\pi (1+cos\,\theta)\,d\theta + \sum_{n=1}^{\infty} A_n \int_0^\pi (sin\, n\theta \cdot sin\,\theta)\,d\theta \right] \tag{2.79}$$

Notice that the term $sin\, n\theta$ is orthogonal to the term $sin\,\theta$ in equation 2.79, and therefore only the term for $n = 1$ is different to zero. Simplifying, we can rewrite equation 2.79 as follows:

$$\Gamma = L\,u_\infty \left[\pi A_0 + \frac{\pi}{2} A_1 \right] \tag{2.80}$$

And applying the Kutta-Joukowski theorem 2.5.2:

$$L_s = \rho_\infty\, u_\infty\, \Gamma = \rho_\infty\, u_\infty^2\, L \left(\pi A_0 + \frac{\pi}{2} A_1 \right) \tag{2.81}$$

In this case the lift is linearly dependent on the angle of attack (recall the definition of A_0 in 2.76), but also on the geometry of the airfoil. However note that the geometry of the airfoil is reduced to two constant factors A_0 and A_1, and therefore it is fair to say that in terms of aeroelasticity the only relevant factor is the angle of attack.

The aerodynamic moment per span unit about the leading edge is calculated, as in the case of the symmetric airfoil, by integrating the lift multiplied by the distance along the cord ζ:

$$M_{s,le} = -\int_0^L \zeta dL_s = \frac{1}{4}\rho_\infty u_\infty^2 L^2 \pi \left(A_0 + A_1 - \frac{A_2}{2} \right) \tag{2.82}$$

As in the case of the lift, the moment depends on the angle of attack (A_0 is a function of the angle of attack) and the geometry of the airfoil. The same conclusions as in the case of the lift related to the factors A_0, A_1 and A_2 can be reached. The only factor affecting the lift and moment related to aeroelasticity is the angle of attack.

2.5.2 Unsteady Aerodynamics

In section 2.5.1 it has been expressed the form of the aerodynamic equations of motion for an steady movement through the thin airfoil theory. These equations don't consider the transient movements of the airfoil, which are basic for the understanding and calculation of the flutter mechanism. In this section we will calculate the transient equations of motion for airfoils based on the thin airfoil theory but including terms for transient movement.

The first description of this mechanism was provided by Theodorsen, 1935, although alternative demonstrations were provided posteriorly by other authors, like Bisplinghoff, Ashley, and Goland, 1963; Fung, 2008, etc. The demonstration that will be used in this section is the small perturbatins theory, and comes from García-fogeda and Arévalo-Lozano, 2015, considering both the 2^{nd} edition from *Garceta* publisher and the original class notes published by the *Universidad Politecnica de Madrid, ETSI Aeronauticos*.

2.5.2.1 Description of the procedure

The study of unsteady aerodynamics adds (obviously) an increased level of complexity to the previous chapters. For this reason it is necessary to describe the steps that will be followed in the upcoming subsections.

1. The first thing we will do is to separate the contributions of the airfoil geometry ($F(z,x,t)$) and the velocity potential ($\Phi(x,z,t)$). We will consider the stationary ($\epsilon_0 z_0(x)$ and $\epsilon_0\varphi_0(x,z)$, geometry and velocity potential respectively) and non-stationary ($\epsilon_1 z_1(x,t)$, $\epsilon_1\varphi_1(x,z,t)$) contributions separately. The intention is to linearize the solution by adding the stationary (calculated in section 2.5.1) plus the non-stationary solutions. Note that we will operate with the implicit function of the camber. This fact will be relevant in the next bullet.

   In section 2.5.1 we defined the airfoil equation (camber line actually) as $z = z(x)$. However **the transient equations have a dependency on time** also, so for unsteady aerodynamics we will define $z = z_a(x,t)$ instead, and the implicit function for the airfoil camber $F(z,x,t)$, where the variable t represents time.

$$F(z,x,t) = z - z_a(x,t) = 0 = z - \epsilon_0 z_0(x) - \epsilon_1 z_1(x,t) \tag{2.83}$$

   Where $\epsilon_0 z_0(x)$ represents the steady airfoil camber shape considering the contribution of the mean angle of attack α_0, and $\epsilon_1 z_1(x,t)$ represents the unsteady contribution of a **flat plate**. Take into account that the oscillation around the mean angle of attack α_0 is sufficiently small, so that the order of magnitude of $\epsilon_0 \approx \epsilon_1 << 1$. With this approximation into account, we can assume linearity in the velocity potential, so it can be expressed as follows:

$$\Phi(x,z,t) = u_\infty x + \epsilon_0\varphi_0(x,z) + \epsilon_1\varphi_1(x,z,t) \tag{2.84}$$

2. Next we will impose the same thin airfoil theory constraint to the airfoil camber. The camber will be a streamline, and to achieve that we will follow a slightly different approach than in stationary aerodynamics. Instead of setting the normal velocity to zero, we will calculate the substantial derivative and operate over that function ($\frac{DF}{Dt} = 0$, note that the derivative is zero because we are operating on the implicit function).

   The derivative is the tangent to the camber function, and therefore operating with the derivative of the camber function imposes the condition of the camber being a streamline. This is possible because the substantial derivative includes an explicit expression for the gradient of the potential of velocities $\nabla\Phi(x,z,t)$, and therefore we will end up with an equation of different terms, where the expression of the velocity potential is explicitly expressed and is one of our unknowns.

   Now we will impose the camber line to be a stream line as described in section 2.5.1. In steady aerodynamics we constrained that the normal velocity to the camber line must be zero, but we will follow a different approach here. We will state that constraint calculating the substantial derivative of the airfoil equation (camber line) and operating on that equation. Remember that $\mathbf{v} = \nabla\Phi$, and the substantial derivative of a fictitious magnitude Ω is $\frac{D\Omega}{Dt} = \frac{\partial\Omega}{\partial t} + \mathbf{v}\nabla\Omega$.

$$\frac{DF(z,x,t)}{Dt} = 0 \iff \frac{\partial F(z,x,t)}{\partial t} + \nabla\Phi \cdot \nabla F(z,x,t) = 0 \mid z = z_a(x,t) \tag{2.85}$$

   Introducing equations 2.83 and 2.84 into 2.85 yields:

$$\begin{aligned}\frac{DF}{Dt} &= -\frac{\partial z_1}{\partial t}\epsilon_1 + (u_\infty + \frac{\partial\varphi_0}{\partial x}\epsilon_0 + \frac{\partial\varphi_1}{\partial x}\epsilon_1\ ,\ \frac{\partial\varphi_0}{\partial z}\epsilon_0 + \frac{\partial\varphi_1}{\partial z}\epsilon_1)\cdot(-\frac{\partial z_0}{\partial x}\epsilon_0 - \frac{\partial z_1}{\partial x}\epsilon_1\ ,\ 1) = 0 \iff \\ \iff &-\frac{\partial z_1}{\partial t}\epsilon_1 - u_\infty\frac{\partial z_0}{\partial x}\epsilon_0 - u_\infty\frac{\partial z_1}{\partial x}\epsilon_1 + \frac{\partial\varphi_0}{\partial z}\epsilon_0 + \frac{\partial\varphi_1}{\partial z}\epsilon_1 + ... + \mathcal{O}^2 = 0\end{aligned} \tag{2.86}$$

   We can identify the terms related to z_0 and z_1 in equation 2.86. Notice that at this stage we will assume the thickness of the airfoil to be neglected and evaluate the functions at $z = 0$, as done in section 2.5.1.

$$\begin{cases}\frac{\partial\varphi_0}{\partial z}(x,0) \propto u_\infty\frac{\partial z_0}{\partial x}(x) \\ \frac{\partial\varphi_1}{\partial z}(x,0,t) \propto u_\infty\frac{\partial z_1}{\partial x}(x,t) + \frac{\partial z_1}{\partial t}(x,t)\end{cases} \tag{2.87}$$

   Note also that **the condition of the airfoil being a streamline, implies that the vertical velocity of the stream in contact with the airfoil is the same as the airfoil**. Otherwise the current would be detached from the airfoil. This fact will take relevance further in this section.

3. Now we will follow a slightly different approach than in section 2.5.1. There we applied the Kutta-Joukowski theorem 2.5.2 to calculate lift around the whole airfoil. However it is also possible to calculate the lift per span unit L_s by integrating the pressure coefficient C_p, which was defined in 2.55, around the whole airfoil and projecting on the perpendicular to the airspeed vector. Notice that in this case the wake is an important part of the control volume, since the unsteady terms will directly impact the vortices in the wake.

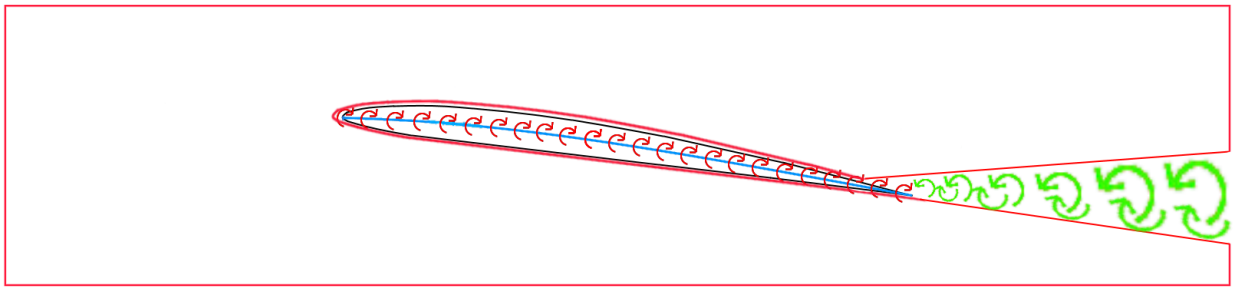

FIGURE 2.13: Control volume excluding wake. The figure represents in red the vortex sheet and in green the Karman Vortex street into the wake.

The wake will be carefully left out of the control volume (see assumption 3), since we don't want to account for the effects of viscosity, but needs to be considered as boundary conditions over the control volume to calculate the circulation of the airfoil at different time intervals.

In order to calculate the pressure coefficient we have one unknown, the pressure scalar field around the airfoil. This field cannot be calculated directly, so we need to employ Bernouilli's equation in its generalized form (equation 2.52, $\frac{\partial \Phi}{\partial t} + \frac{1}{2}|\nabla \Phi|^2 + \int \frac{dp}{\rho} = C_1(t)$). Remember that Bernouilli's equation related the scalar field of pressures to the velocity potential, and previously we had an expression for the velocity potential. The only term left is the pressure and density integral, which will be estimated by thermodynamics relationships.

At last, we reach an expression for the pressure coefficient C_p in terms of the (currently unknown) unsteady velocity potential.

The demonstration can be found as an annex in section A.2, and the main conclusions are the following equations:

$$\begin{cases} C_{p,0} = -\frac{2}{u_\infty^2} \frac{\partial \varphi_0}{\partial x}(x,0) \\ C_{p,1} = -\frac{2}{u_\infty^2} \left[\frac{\partial \varphi_1}{\partial t}(x,0,t) + u_\infty \frac{\partial \varphi_1}{\partial x}(x,0,t) \right] \end{cases} \tag{2.88}$$

Where the subindex $_0$ accounts for the steady aerodynamics terms contribution and $_1$ for the unsteady. It is relevant to acknowledge the differentiation between both terms The steady aerodynamics don't include a dependency with time t, while the unsteady terms do. Also we will assume that the curvature is small enough as to be able to calculate the contribution to the unsteady pressure coefficient as the movement of a flat place, and hence the dimension z will be zero.

4. The next step is to adimensionalize the values for displacements and velocities, in our case rotation and vertical displacement. This is necessary because the unsteady motion requires these values to oscillate around a mean value with a given amplitude, and in this case we will adimensionalize the vertical position and velocity with the semicord, while the angular position and velocity will be adimensionalized with the mean angle of attack and the distance between the elastic axis and the cord midpoint. Also the reduced frequency k will be introduced. The reduced frequency is also an adimensional parameter, that puts the oscillation frequency relative to the flight airspeed and the semicord dimension, and will take relevance further on.

   Next we will introduce some oscillatory parameters. The oscillating amplitude, airfoil circulation, wake circulation and velocity potential. To solve the unsteady aerodynamics problem

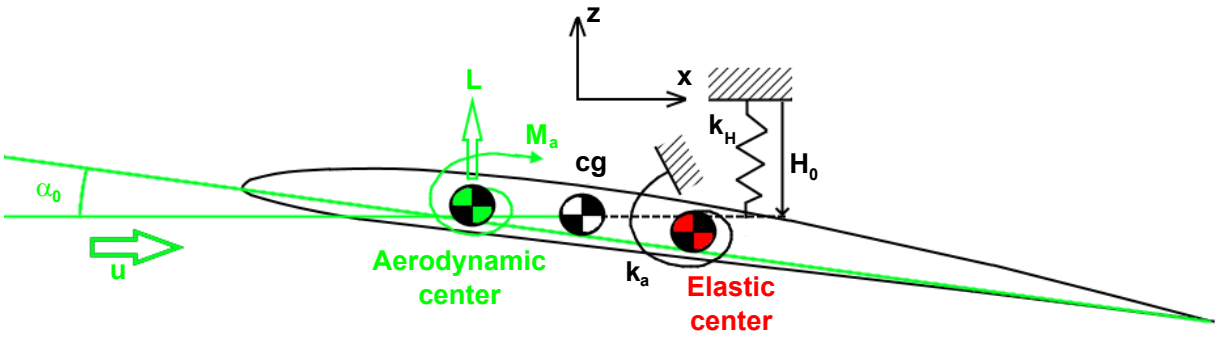

FIGURE 2.14: Airfoil definitions

we will assume a harmonic motion for the airfoil with oscillating frequency ω, and also the associated parameters, wake and airfoil circulations and velocity potential, will be defined as harmonic functions oscillating with the same frequency ω. Note also that the phase angle of each parameter is unknown, and therefore we will need to define the amplitudes as complex functions.

The stationary potential has been calculated already in section 2.5.1. To calculate the velocity potential $\varphi_1(x,z,t)$ we need to note that the following average values (as amplitudes for complex functions) apply to the airfoil, since will be useful later to understand the full problem:

$$\begin{aligned} &\textit{Vertical displacement}: \\ &\qquad \hat{z}_h = \frac{-h_0}{B} \\ &\qquad \hat{w}_h = \frac{-i\,k\,h_0}{B} = i\,k\,\hat{z}_h \approx \left.\frac{\partial \varphi_1}{\partial z}\right|_h \\ &\textit{Pitch movement}: \\ &\qquad \hat{z}_\alpha(x) = \alpha_0(A_e - x) \\ &\qquad \hat{w}_\alpha = \alpha_0[-1 + i\,k(A_e - x)] = i\,k\,\hat{z}_\alpha(x) - \alpha_0 \approx \left.\frac{\partial \varphi_1}{\partial z}\right|_\alpha \end{aligned} \tag{2.89}$$

Where h_0 is the mean vertical displacement, α_0 the mean angle of attack, i is the imaginary unit (included to indicate a 90 degrees offset between the displacement and the velocity), $B = L/2$ is the semicord dimension, $k = \frac{\omega B}{u_\infty}$ is the reduced frequency, A_e is the position of the elastic axis relative to the cord mid point, $\hat{w}$ is the velocity equation of the airfoil and $\hat{z}(x)$ is the airfoil equation of the airfoil considering the displacement. The subindexes $_h$ and $_\alpha$ indicate respectively a vertical displacement or pitching displacement, and the $\hat{tilde}$ indicates adimensional variables. These parameters indicate the amplitude value of the movement of the airfoil in case we consider an isolated vertical or pitching movement, and even though they will be useful later, the main reason to introduce them here is for better understanding of the mathematical mechanism.

We can assume that, even in unsteady motion, we can reach a stationary state by the airfoil oscillating at a given frequency. We can therefore define the movement of the structure as a

harmonic function, where we can introduce complex notation to model the position of the airfoil, the vortices distribution and the velocity potential in the following way:

$$\begin{aligned} z_1(x,\omega,t) &= \mathcal{R}[\overline{z_1}(x,\omega)e^{i\omega t}] \\ \gamma_a(x,\omega,t) &= \mathcal{R}[\overline{\gamma_a}(x,\omega)e^{i\omega t}] \\ \gamma_w(x,\omega,t) &= \mathcal{R}[\overline{\gamma_w}(x,\omega)e^{i\omega t}] \\ \varphi_1(x,z,\omega,t) &= \mathcal{R}[\overline{\varphi_1}(x,z,\omega)e^{i\omega t}] \end{aligned} \tag{2.90}$$

Where ω is the angular frequency and $\overline{z_1}$, $\overline{\gamma_a}$, $\overline{\gamma_w}$ and $\overline{\varphi_1}$ are the (in general) complex functions defining the amplitudes of the oscillatory airfoil position, airfoil vortices, wake vortices and velocity potential respectively. The tilde indicates the amplitude (complex if applicable) of the corresponding harmonic function. The demonstration of why we can model such equations by oscillatory movements of frequency ω are out of the scope of this thesis, although Bisplinghoff, Ashley, and Goland, 1963 provides a very good demonstration.

5. Now we need to calculate the expression for the vortices distribution. Recapping up to this point, we have calculated an expression for the pressure coefficient as a function of the velocity potential, which is an unknown to us. However we can relate the vertical velocity (induced by the vortices distribution) to the velocity potential (equation 2.59).

   Recall that we defined our control volume excluding the airfoil and wake. however the values for the circulation in the boundaries between our control volume and the wake, and our control volume and the airfoil need to be the same, and those are the values that we will calculate.

   Now, we will have two different vortices sheets, one in the airfoil and another in the wake, and hence when calculating the vertical velocity we will have the contribution from two different vortices sheets. However those are both related. We need to explain one physical phenomenon before. The wake receives the circulation from the airfoil in the form of detached vortices. At a given time interval, the airfoil "throws" a vortex from the trailing edge containing the circulation of the whole airfoil to the surrounding air current. This vortex is what creates the wake, and the constant flow of vortices from the airfoil to the wake are what constitute the wake and the wake circulation. In a steady aerodynamics analysis there is a constant flow, and therefore the global integration is the same. However in unsteady aerodynamics the solution needs to take into account the contribution from each cycle. As a summary, it is necessary to equal the increment to the wake circulation with the detached vortex from the trailing edge. With this into consideration, we have a mechanism to relate the airfoil circulation with the wake circulation, and in the integration of the velocity potential we have two unknowns, the velocity potential derivative with respect to z and the vortices distribution along the airfoil. However remember. We defined the camber as a stream line, and therefore the only means of the vertical velocity not being zero on the camber is if the movement of the airfoil is the same as the induced vertical airspeed, so the derivative with respect to z of the velocity potential must equal the induced vertical velocity $\frac{\partial\overline{\varphi_1}}{\partial z} = \overline{w}$, and hence we have a means of calculating the vortices distribution with only one unknown.

   We will introduce some

   The demonstration can be found in section A.4, and the main equation that can be derived from this epigraph is the expression of the circulation of the vertex sheet on the airfoil:

$$\begin{cases} \hat{\gamma}_a(\hat{x},k) = \frac{2}{\pi}\sqrt{\frac{1-\hat{x}}{1+\hat{x}}}VP\left[\int_{-1}^{1}\sqrt{\frac{1+\hat{\zeta}}{1-\hat{\zeta}}}\frac{\frac{\partial\hat{\varphi}_1}{\partial z}(\hat{\zeta},0,k)}{\hat{x}-\hat{\zeta}}d\hat{\zeta} + \frac{ik\hat{\Gamma}e^{ik}}{2}\int_{1}^{\infty}\frac{e^{-ik\hat{\zeta}}}{\hat{x}-\hat{\zeta}}\sqrt{\frac{\hat{\zeta}+1}{\hat{\zeta}-1}}d\hat{\zeta}\right] \\ \hat{\Gamma} = \frac{2VP\int_{-1}^{1}\sqrt{\frac{1+\hat{\zeta}}{1-\hat{\zeta}}}\frac{\partial\hat{\varphi}_1}{\partial z}(\hat{\zeta},0,k)d\hat{\zeta}}{ike^{ik}\frac{\pi}{2}(H_1^{(2)}(k)+iH_0^{(2)}(k))} \end{cases} \tag{2.91}$$

Where VP indicates Cauchy's principal value, and note that we defined the adimensional values and mean values in bullet 4, and the expression for the vertical velocity is also known and defined in equations 2.89. The tildesˆrepresent adimensional variables and the functions $H_0^{(2)}$ and $H_1^{(2)}$ represent Hankel functions as defined by equations A.31.

6. Once calculated the distribution of vortices on the airfoil camber, we need to calculate the pressure coefficient in order to calculate the forces and moments on the airfoil.

   The demonstration of this epigraph can be found in section A.5, and as a summary, we can indicate that the basic equations for the pressure coefficient are:

$$\Delta\hat{C}_p(\hat{x},k) = 2\left[\hat{\gamma}_a(\hat{x},k) + ik\int_{-1}^{\hat{x}}\hat{\gamma}_a(\hat{\zeta},k)d\hat{\zeta}\right] \tag{2.92}$$

   Now, from the calculated value of γ_a in equation 2.91:

$$\Delta\hat{C}_p(\hat{x},k) = \frac{4}{\pi}VP\int_{-1}^{+1}\frac{\partial\hat{\varphi}_1}{\partial z}(\hat{\zeta},k)\left[\sqrt{\frac{1-\hat{x}}{1+\hat{x}}}\sqrt{\frac{1+\hat{\zeta}}{1-\hat{\zeta}}}\frac{1}{\hat{x}-\hat{\zeta}} - ik\Lambda(\hat{x},\hat{\zeta})\right]d\hat{\zeta} + \\ + \frac{4}{\pi}[1-C(k)]\sqrt{\frac{1-\hat{x}}{1+\hat{x}}}\int_{-1}^{+1}\sqrt{\frac{1+\hat{\zeta}}{1-\hat{\zeta}}}\frac{\partial\hat{\varphi}_1}{\partial z}(\hat{\zeta},k)d\hat{\zeta} \tag{2.93}$$

   Where:

$$\Lambda(\hat{x},\hat{\zeta}) = \frac{1}{2}Ln\left[\frac{1-\hat{x}\hat{\zeta}+\sqrt{1-\hat{\zeta}^2}\sqrt{1-\hat{x}^2}}{1-\hat{x}\hat{\zeta}-\sqrt{1-\hat{\zeta}^2}\sqrt{1-\hat{x}^2}}\right] \tag{2.94}$$

   And $C(k)$ is known as the Theodorsen function:

$$C(k) = \frac{H_1^{(2)}(k)}{H_1^{(2)}(k)+iH_0^{(2)}(k)} \tag{2.95}$$

   This expression for the pressure coefficient is dependent on the movement of the structure, since we are still carrying the term $\frac{\partial\varphi_1}{\partial z}$, but remember that this term is known.

7. Once calculated the pressure coefficient, it is possible to calculate the aerodynamic interactions of interest in our problem, say aerodynamic forces (meaning vertical movement of the airfoil) and moments (meaning rotation around the elastic axis) by integration:

$$\begin{cases} \hat{q_h}(k) = Q_\infty B\int_{-1}^{+1}\Delta\hat{C}_p(\hat{x},k)(-1)d\hat{x} \\ \hat{q_\alpha}(k) = Q_\infty B^2\int_{-1}^{+1}\Delta\hat{C}_p(\hat{x},k)(A_e-\hat{x})d\hat{x} \end{cases} \tag{2.96}$$

Where $\hat{q_h}$ is the bending aerodynamic force (similar to the static lift in equation 2.81), $\hat{q_\alpha}$ is the torsion aerodynamic moment (similar to the static aerodynamic moment in equation 2.82), A_e is the distance between the cord mid point and the elastic axis, $B = \frac{L}{2}$ is half the cord length, Q_∞ the dynamic pressure at infinity and $\hat{C}_p$ the pressure coefficient in non-dimensional units. Now, substituting equations 2.93 and 2.89 into 2.96 and integrating, yields:

$$\begin{cases} \frac{\hat{q_h}(k)}{Q_\infty B} = -2\pi \left[t_0 \frac{d\alpha}{dt} + t_0^2 \left(\frac{\frac{d^2h}{dt^2}}{B} - A_e \frac{d^2\alpha}{dt^2} \right) \right] - 4\pi C(k) \left\{ \alpha + t_0 \left[\frac{\frac{dh}{dt}}{B} + \left(\frac{1}{2} - A_e \right) \frac{d\alpha}{dt} \right] \right\} \\ \frac{\hat{q_\alpha}(k)}{Q_\infty B^2} = -2\pi \left\{ t_0 \left(\frac{1}{2} - A_e \right) \frac{d\alpha}{dt} + t_0^2 \left[-A_e \frac{\frac{d^2h}{dt^2}}{B} + \left(\frac{1}{8} + A_e^2 \right) \frac{d^2\alpha}{dt^2} \right] \right\} + \\ \qquad + 4\pi \left(\frac{1}{2} + A_e \right) C(k) \left\{ \alpha + t_0 \left[\frac{\frac{dh}{dt}}{B} + \left(\frac{1}{2} - A_e \right) \frac{d\alpha}{dt} \right] \right\} \end{cases} \tag{2.97}$$

Where we introduced a new parameter $t_0 = \frac{B}{u_\infty}$, which is the characteristic time of the movement. Also recall the variables h, the vertical displacement variable, and α, the torsional angular variable.

Notice that the derivation of equation 2.97 has been reduced to the case of interest for the present thesis. Usually in the literature describing this equation there is a third degree of freedom, the lift produced by the hinge of the aileron. In this case such degree of freedom has not been included for simplicity, taking into account that the contribution of the aileron might be of interest for a generic flutter case, but is not relevant for the problem described in the present thesis.

The most important conclusion of the current section, which justifies this lengthy derivation of equations, is this:

The aerodynamic forces under unsteady conditions depend upon the following parameters: α, $\frac{d\alpha}{dt}$, $\frac{d^2\alpha}{dt^2}$, $\frac{dh}{dt}$ and $\frac{d^2h}{dt^2}$.

This dependency on those parameters will be the most important condition in section 2.6.

2.6 Flutter on an Airfoil

Once derived the equations for all the forces involved in the flutter mechanism, it is possible to describe the concept of flutter with a mathematical foundation.

We will start developing the basic second degree linear differential equation as described in classical vibrations with viscous damping (2.25), in this case excited by aerodynamic forces:

$$\begin{bmatrix} M & S_\alpha \\ S_\alpha & I_\alpha \end{bmatrix} \begin{bmatrix} \frac{d^2h}{dt^2} \\ \frac{d^2\alpha}{dt^2} \end{bmatrix} - \begin{bmatrix} c_h & c_{h,\alpha} \\ c_{h,\alpha} & c_\alpha \end{bmatrix} \begin{bmatrix} \frac{dh}{dt} \\ \frac{d\alpha}{dt} \end{bmatrix} + \begin{bmatrix} k_h & k_{h,\alpha} \\ k_{h,\alpha} & k_\alpha \end{bmatrix} \begin{bmatrix} h \\ \alpha \end{bmatrix} = \begin{bmatrix} q_h(\frac{dh}{dt}, \frac{d^2h}{dt^2}, \alpha, \frac{d\alpha}{dt}, \frac{d^2\alpha}{dt^2}, Q_\infty) \\ q_\alpha(\frac{dh}{dt}, \frac{d^2h}{dt^2}, \alpha, \frac{d\alpha}{dt}, \frac{d^2\alpha}{dt^2}, Q_\infty) \end{bmatrix} \tag{2.98}$$

Notice that equation 2.98 is a non-homogeneous matrix equation. However as we can see in equation 2.97, all the terms in the aerodynamic forces depend on any of the parameters $\frac{dh}{dt}$, $\frac{d^2h}{dt^2}$, α, $\frac{d\alpha}{dt}$, $\frac{d^2\alpha}{dt^2}$, so we can reorganize equation 2.98 and turn it into a homogeneous system of equations in matrix form:

$$\begin{bmatrix} M - q_{h,1}(Q_\infty) & S_\alpha - q_{h,2}(Q_\infty) \\ S_\alpha - q_{\alpha,1}(Q_\infty) & I_\alpha - q_{\alpha,2}(Q_\infty) \end{bmatrix} \begin{bmatrix} \frac{d^2h}{dt^2} \\ \frac{d^2\alpha}{dt^2} \end{bmatrix} - \begin{bmatrix} c_h - q_{h,3}(Q_\infty) & c_{h,\alpha} - q_{h,4}(Q_\infty) \\ c_{h,\alpha} - q_{\alpha,3}(Q_\infty) & c_\alpha - q_{\alpha,4}(Q_\infty) \end{bmatrix} \begin{bmatrix} \frac{dh}{dt} \\ \frac{d\alpha}{dt} \end{bmatrix} + \tag{2.99}$$

$$+ \begin{bmatrix} k_h & k_{h,\alpha} - q_{h,5}(Q_\infty) \\ k_{h,\alpha} & k_\alpha - q_{\alpha,5}(Q_\infty) \end{bmatrix} \begin{bmatrix} h \\ \alpha \end{bmatrix} = \begin{bmatrix} 0 \\ 0 \end{bmatrix} \tag{2.100}$$

Where the terms $q_{h,i}(Q_\infty)$ and $q_{\alpha,i}(Q_\infty)$ represent the terms of the aerodynamic forces multiplied by their respective variable.

Remember that from section 2.3.2.1, when considering two degrees of freedom it is indifferent to derive the model considering viscous or structural damping, since both have a direct relationship as described in 2.24 once diagonalized. With that information into account, we can solve the matrix equation and return independent solutions for each degree of freedom and for each dynamic pressure, considering cuasi-stationary conditions as described in section 2.3.2.2, equation 2.26 (considering the same nomenclature):

$$\begin{aligned} x_h &= B_h \cdot e^{-\zeta_h \omega_{n,h} t} \cdot sin(\omega_{d,h} t + \varphi_h) \\ x_\alpha &= B_\alpha \cdot e^{-\zeta_\alpha \omega_{n,\alpha} t} \cdot sin(\omega_{d,\alpha} t + \varphi_\alpha) \end{aligned} \tag{2.101}$$

Now this is the most important result of this lengthy demonstration.

The vibration of the two different modes in equations 2.101 is not independent, since both ω_h and ω_α, and ζ_h and ζ_α are linked by the parameters $\frac{dh}{dt}$, $\frac{d^2h}{dt^2}$, α, $\frac{d\alpha}{dt}$, $\frac{d^2\alpha}{dt^2}$ and q_∞.

This important conclusion is what drives the flutter phenomenon.

2.7 Flutter signal particularities

In general the importance of the signal quality is considered a secondary factor in flutter data processing. This is usually a consequence of the extreme cost, risk and complications associated to the extraction of data from Flutter Flight Tests. Take into account that each flight is scheduled in advance, aircraft are not always operationally available and occasionally the planes are not dedicated for Flutter Flight Tests. Sometimes other tests are scheduled and the Flutter instrumentation is removed. Some others the tests must be aborted due to maintenance, weather, etc. This fact implies that once the test starts and the atmospheric conditions are suitable for flying, it must be completed even if the atmospheric conditions are not optimal for data gathering. Also note that the risk and cost associated to the tests usually imply that in case data are not good, unless there is a very good reason to, it is not possible to repeat the test points. This poses a problem for Sine-Dwell signals for the reasons that will be described below.

2.7.1 Wing Flutter Signals

During flutter flight tests the aircraft needs to be excited at given frequencies in order to extract measurable data. There are several excitation and data extraction techniques. In our case, we will focus on Sine-Dwell signals. They consist of a frequency sweep at a given frequency and constant amplitude. The signal is measured after the excitation stops, and the expected value is an exponentially damped sinusoid representative of a natural mode. The excitations are produced as a series of close frequency programs, so that the expected mode is close to one of the modes excited by the FECU. For example, if the expected mode lies at 5.5Hz, the FECU runs a series of programs at 5.2Hz, 5.3Hz and so on until 5.9Hz, so that the operators are able to see an evolution

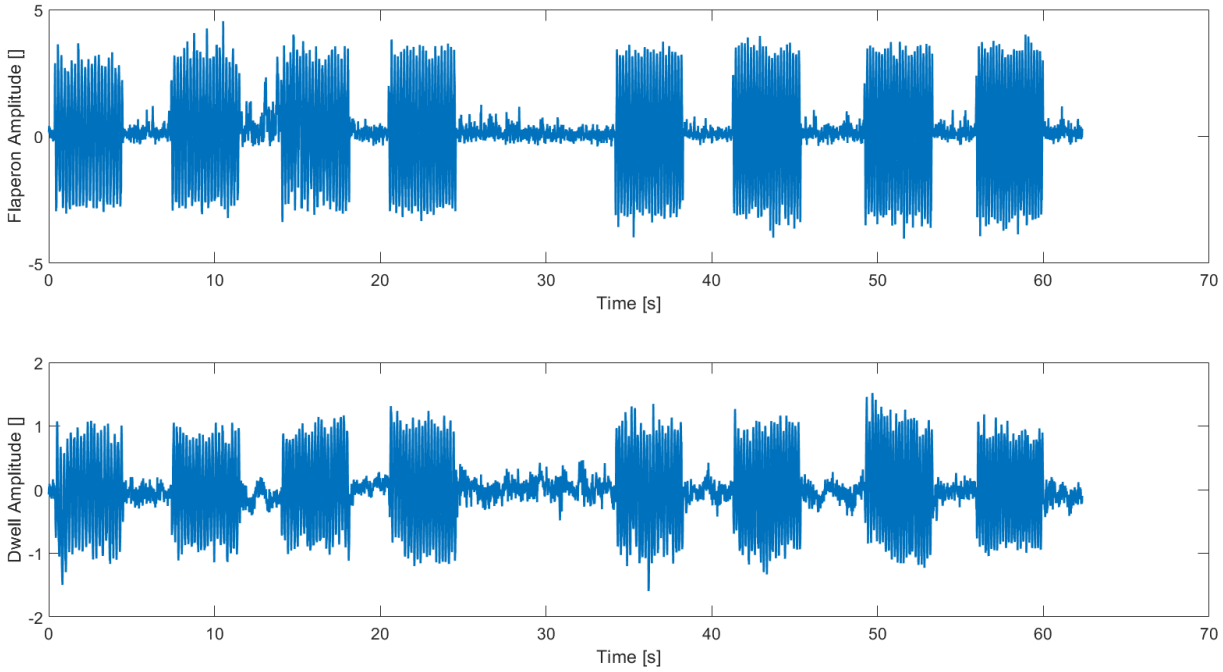

FIGURE 2.15: Sample data. Sine Dwells

on the aircraft responses when excited at each frequency and accurately estimate the natural mode. Note that the closer the excitation is to the natural mode, the most pure is the response from the aircraft mechanical system, and hence a better frequency and damping estimation will be able to be performed.

Figure 2.15 shows an example of the Sine-Dwell excitation series extracted from a real flight. The upper side of the plot shows the recording from the flaperons (the exciting surface), while the lower side of the plot shows the response from one of the wing extensometers. With this kind of excitation, the objective is to start recording and processing data right after each excitation stops, and stop recording either when 5 seconds have passed or, in case the time between excitations is lower than 5 seconds, right before the next excitation is started.

Note that it is usual that the excitations take less than 5 seconds, since different events can occur. The most typical case happens when the signals are far from the flutter point and the damping is high. In that case the response signal usually disappears before 5 seconds have passed, and therefore the Test Director commands the pilot to proceed with the next point without further delay. Another less common situation for shorter signals, but not unexpected either (in fact the attention of the Test Director in the control room is focused on monitoring this event) is when the aircraft reaches the flutter point (or close to it). At that time the damping is very low or even negative, and the response of the extensometers seems to increase with time after the excitation stopped. In that case the Test Director commands the emergency stop of the test, the Pilot flies the aircraft into a known safe point of the Flight Envelope (already known safe flight conditions of airspeed and altitude), the chase aircraft performs an external visual check (searching loose or broken parts) and they both start the return to base procedure.

2.7.2 Frequency resolution

The signals acquired are very short in time duration, usually 3s to 5s (note that damping is inversely proportional to the signal duration), and the frequency associated is also low, usually 2Hz to 10Hz. Classical textbooks on signal processing, like Oppenheim and Schafer, 2009, describe

the problem associated to extract good frequency resolution from short time signals when the frequency associated is low.

In particular the resolution of the Fourier transform depends only on the length (in time) of the signal to be processed:

$$\begin{cases} T = \frac{N}{fs} \\ \Delta t = \frac{T}{N} = \frac{N}{fs}\frac{1}{N} = \frac{1}{fs} \\ f_{max} = \frac{fs}{2} \\ Resolution = \Delta f = \frac{f_{max}}{N/2} = \frac{2fs}{2N} = \frac{N}{N \cdot T} = \frac{1}{T} \\ \Delta f = \frac{1}{T} \end{cases} \tag{2.102}$$

Where T is the maximum length of the time signal (in units of time), N is the maximum length of the time signal (in number of samples), fs is the sampling frequency, Δt is the time resolution, f_{max} is the maximum frequency obtainable with that sampling frequency for the Fourier Transform and Δf is the frequency resolution in the frequency domain.

Notice that the frequency resolution depends only on the length of the time signal T. In a typical flutter test the values are the following:

$$\begin{cases} T = 5s \\ fs = 80Hz \\ f_n = 4Hz \\ \Delta t = 0.0125s \\ f_{max} = 40Hz \\ \Delta f = 0.2Hz \end{cases} \tag{2.103}$$

Where f_n is a typical natural frequency.

In our case 0.2Hz is a bad resolution considering that the reference frequency is 4Hz. These values cannot be improved without increasing the acquisition time, and also in that case, considering a damped sinusoid, the increase in time will only increase samples with low energy, which implies that the global contribution will not improve the global resolution, this is equivalent to calculating a DFT with more samples and interpolating in frequency, but the information in the system will not be increased. Possible techniques to improve the resolution may include averaging by redundancy with other sensors. However these techniques are out of the scope of the present thesis and can be subjected to future investigations.

In case of increasing the sampling frequency nothing will change. Notice that the sampling frequency increase will only increase the maximum frequency in the Fourier Transform, not the resolution, and on top of that the processing requirements of the computer will be increased. However notice that the energy leaked through the high energy values in case of reducing the maximum frequency will be absorbed by the low energy region, and therefore increasing the error of the estimation by introducing errors in the signal transform.

2.7.3 High damping and relationship with short duration

This epigraph is intended to remark the difficulties to properly identify signals with low frequency, low damping and consequently short time duration.

The damping is the rate at which the signal fades out and falls below the noise level at an inverse exponential ratio. From this perspective, the damping is directly related with the effective duration of the signal. The higher the damping the shorter the duration. Even if the acquisition time is longer, if the damping is low enough there will be not enough samples as to reconstruct (identify) the signal correctly, specially if the noise level is so high that the signal quickly falls

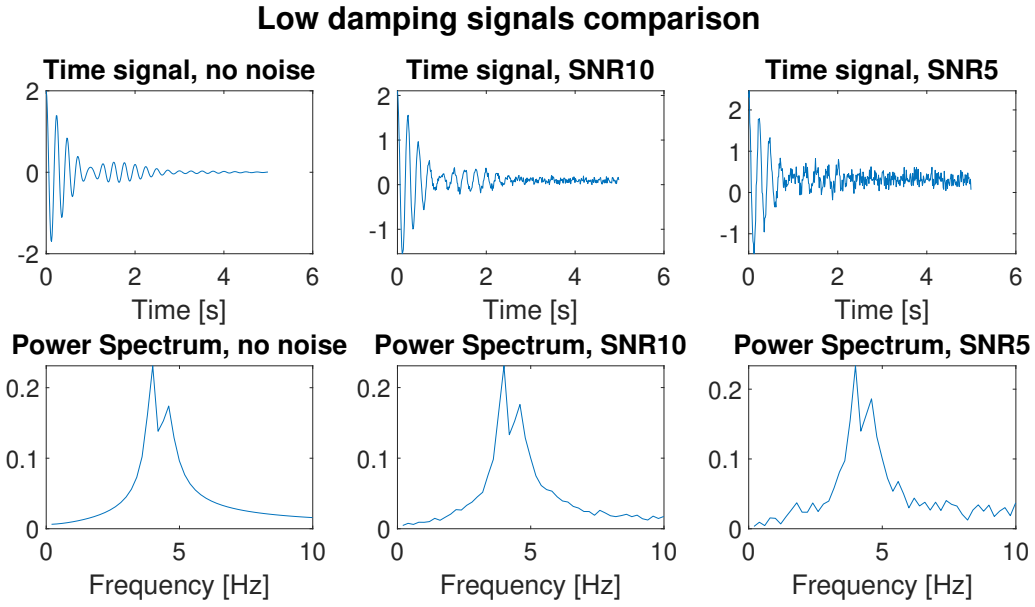

FIGURE 2.16: Comparison of different versions of the same signal with different levels of noise and its power spectrum. Low damping.

below the noise level. In this section we will define a signal representative of flutter vibrations and will analyze it increasing the noise values. The objective is to check the difficulties resulting from analyzing these signals given the constraints defined. The analysis of this signal will be made following the PRESTO technique.

Let's assume a typical case with the following parameters with and without noise:

$$\begin{cases} f_1 = 4.000Hz \\ \zeta_1 = 0.040 \\ f_2 = 4.500Hz \\ \zeta_2 = 0.050 \\ t = 5.000s \\ \varphi_1 = \varphi_2 = 0.000 \\ A_1 = A_2 = 1.000 \\ SNR_1 = \infty \\ SNR_2 = 10 \\ SNR_3 = 5 \end{cases} \tag{2.104}$$

Under these conditions the signals are represented in figure 2.16. Each signal is constructed as the addition of two exponentially damped sinusoid signals, and there are three different solutions depending of the level of white noise added.

The plots clearly show two modes in the time domain and two distinct peaks in the frequency domain. While the peaks in the frequency domain remain, the noise added increments the noise of the tails of the spectrum, increasing with every noise level. However, in the time domain the results show that most of the signal (the last 4 seconds out of 5) for the 5dB SNR fall under or at the same level as the noise background. These effect is not so much noticeable for the 10dB SNR, although the signal is somehow distorted.

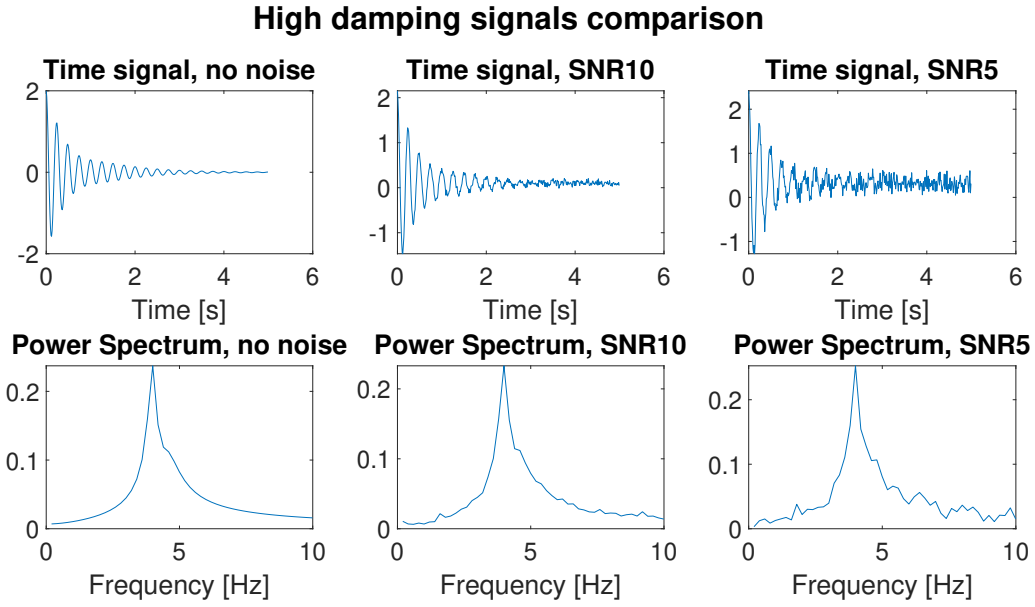

FIGURE 2.17: Comparison of different versions of the same signal with different levels of noise and its power spectrum. High noise and low damping.

Considering a different construction, with the same parameters but the damping of the second mode greatly increased:

$$\begin{cases} f_1 = 4.000Hz \\ \zeta_1 = 0.040 \\ f_2 = 4.500Hz \\ \underline{\zeta_2 = 0.1} \\ t = 5.000s \\ \varphi_1 = \varphi_2 = 0.000 \\ A_1 = A_2 = 1.000 \\ SNR_1 = \infty \\ SNR_2 = 10 \\ SNR_3 = 5 \end{cases} \tag{2.105}$$

We can plot the signals in figure 2.17. The noiseless plot shows almost no distortion for the second mode, both in the time and frequency domains. There is a slight skew in the frequency domain, indicating the presence of a second mode, but in the time domain it is not possible to identify the presence of a second mode to the bare eye. The 10dB SNR signal shows a similar result. The frequency domain shows a peak also indicating the existence of a second mode. Although the presence of noise may distort the peak, the level of noise is still not so high as to fade the second mode peak. However, the time signal shows a similar behavior to the noiseless case, easily identifying one single mode but the second is not evident. The 5dB SNR is a different case. In the frequency domain it is very clear the existence of a second mode, although the noise level being of the same magnitude as the signal distorts the signal and leads to confusion. The time signal reaches the noise level close to the first second, so leaves very small samples for reaching conclusions.

The analysis of these results is depicted in table 2.1. Comparing the results for low damping,

	Low damping			High damping		
	Noiseless	SNR 10	SNR 5	Noiseless	SNR 10	SNR 5
$f_1[Hz]$	4.000	4.004	3.995	4.000	3.987	4.001
$\zeta_1[\,]$	0.040	0.039	0.035	0.040	0.036	0.072
$f_2[Hz]$	4.500	4.510	4.548	4.500	4.485	0.019
$\zeta_2[\,]$	0.050	0.054	0.074	0.100	0.120	0.581

TABLE 2.1: Summary of signals comparison results

the identification of all noise levels returns almost no difference. The only parameter with error above the average error is the damping of the second mode. However the value is still within the order of magnitude of the actual value. When analyzing the high damping modes, the signals are still the same as in the previous case, but the damping of the second mode (4.5Hz) is greatly increased, to 0.1. The 10dB SNR signal analysis returned very similar values to the original signals. However the 5dB SNR signal analysis returned only one mode. The second mode (4.5Hz) is modeled as 0.019Hz, which is practically a flat signal (52s period), with a damping of 0.581, which means that the signal is basically reducing its continuous average level at a soft decaying rate. This value is completely biased related to the actual value of the signal.

This example shows the influence of the high damping as related to the identification of signals with a short lifetime, which is the case on flutter signals.

Chapter 3

Investigation

3.1 Introduction to this chapter

In the previous chapters several important points were demonstrated:

1. Flutter solutions represent a subset of non-linear equations of a second degree differential equation, depending on dynamic pressure, stiffness, aerodynamic, mass and damping matrices.
2. During an envelope expansion campaign it is necessary to identify each frequency and damping of the modes of interest as soon as possible, preferably in real time.
3. From the different excitation signals possible to employ during the flutter tests, the Sine Dwell signals have the following characteristics:
    - Have short duration, and therefore the frequency resolution is very low.
    - Require the pilot and aircraft to stay in flutter conditions for the shortest period of time, and thus minimizing the risk for the life of the pilot and integrity of the aircraft.

Even though the Sine Dwell excitation techniques have several drawbacks, the minimization of the risk for the life of the pilot and integrity of the aircraft make it very attractive for flutter tests, in particular in cases where it is intended to get close to the flutter point and extract the maximum of the flight envelope. Also this area of investigation is mostly unexplored given the uncertainties related to the signals identification problems, and therefore leaves a wide room open for innovations.

The current chapter will follow the path below:

- Demonstrate the importance of the phase angle related to the modal identification of the flutter signals. Section 3.2.1.
- Develop a relationship between the bandwidth of the signal power spectrum and the damping of the signal. Section 3.2.2.
- Present different Data Processing techniques. Section 3.3.
    - Classical techniques. Sections 3.3.1, 3.3.2, 3.3.3 and 3.3.4.
    - Deep Learning techniques. Section 3.3.5.
- Classical Data Processing path.
    - Select the most promising classical data processing techniques, performing a comparison between the synthetic datasets analysis. Section 3.4.
    - Introduce a new robust data processing technique based on the results on the previous step, the PRESTO technique. Section 3.5.

  - Verify the PRESTO technique with synthetic data and compare to Laplace Wavelet Matching Pursuit. Section 3.6.

- Deep Learning path.

  - Select the most promising Deep Learning techniques, performing a comparison between the synthetic datasets analysis. Section 3.7.

- Compare the PRESTO, Laplace Wavelet Matching Pursuit and Deep Learning techniques results on synthetic data. Section 3.8

- Validate the PRESTO, Laplace Wavelet and Deep Learning techniques with real flight test data. Section 3.9.

3.2 Phase angle and bandwidth in linear second order ordinary differential equations

In this section we will demonstrate the importance of the phase angle in the identification of a single mode and further the relationship between the phase angle and the bandwidth to estimate the signal parameters.

3.2.1 Relationship between the phase angle and the damping ratio

We will start recalling the flutter model equation, based on a linear second order degree ordinary differential equation 2.101, in the form of a signal sum of both motions:

$$x(t) = \sum_{j=1}^{K} a_j \cdot e^{-\zeta_j \omega_{nj} t} \sin\left(\omega_{dj} t + \varphi_j\right) + \nu(t) \tag{3.1}$$

Where K is the number of modes, a_j is a constant representing amplitude, ζ_j is the damping factor, ω_{nj} represents the natural angular frequency of the structure, t is the time variable, $\omega_{dj} = \omega_{nj}\sqrt{1-\zeta_j^2}$ is the damped angular frequency, φ_j represents the phase angle and $\nu(t)$ accounts for structural and aerodynamic noise.

Notice that we will limit the number of different modes to $K = 2$, representing a signal subjected to the interaction between bending and torsion. Under this premise and considering the results from section 2.3.2.2, it is possible to model the system either with structural or viscous damping indistinctly. For this reason we have assumed equation 3.1 to be modeled under viscous damping to simplify the calculations. Another obvious constraint is to assume an underdamped system, $(0 < \zeta < 1)$, in order to get a vibrational response. The reason to expect a vibrational response is because only vibrational responses, indeed very low dampings, are the ones that present flutter interactions and hence are of interest for the current problem.

Under the aforementioned premises, the Fourier transform of equation (3.1) (multiplied by a step function to return responses between 0 and ∞) is:

$$X(\omega)\big|_{\varphi \neq k\pi} = F\{x(t)\}\big|_{\varphi \neq k\pi} = \frac{b \cdot (\alpha + i\omega)}{(\zeta\omega_n + i\omega)^2 + \omega_n^2(1-\zeta^2)} = \frac{b \cdot (\alpha + i\omega)}{\omega_n^2 - \omega^2 + i2\zeta\omega_n\omega} \tag{3.2}$$

Where:

$$\alpha = \frac{\omega_n\sqrt{1-\zeta^2}}{\tan(\varphi)} + \zeta\omega_n = \omega_n\left(\frac{\sqrt{1-\zeta^2}}{\tan\varphi} + \zeta\right) = \omega_n\beta \tag{3.3}$$

$$b = \frac{a}{\sqrt{2\pi}} \sin(\varphi) \tag{3.4}$$

$$\beta = \frac{\sqrt{1-\zeta^2}}{\tan\varphi} + \zeta \tag{3.5}$$

From equation (3.2) we can calculate the power spectrum:

$$S_x(\omega)|_{\varphi \neq k\pi} = |X(\omega)|^2\big|_{\varphi \neq k\pi} = \frac{b^2 \cdot (\omega^2 + \alpha^2)}{(\omega_n^2 - \omega^2)^2 + 4\zeta^2\omega_n^2\omega^2} = \frac{b^2 \cdot (\omega^2 + \alpha^2)}{\omega_n^4 + \omega^4 + \omega_n^2\omega^2(4\zeta^2 - 2)} \tag{3.6}$$

Where constant b is a function of the phase angle φ. This expression is valid $\forall\varphi \neq k\pi, \forall k \in \mathbb{Z}$, expression representing a classical exponentially damped sinusoidal. In such case we can calculate the Fourier transform:

$$X(\omega)|_{\varphi = k\pi} = F\{x(t)\}|_{\varphi = k\pi} = \frac{b'}{(\zeta\omega_n + i\omega)^2 + \omega_n^2(1-\zeta^2)} = \frac{b'}{\omega_n^2 - \omega^2 + i2\zeta\omega_n\omega} \tag{3.7}$$

And the power spectrum:

$$S_x\,(\omega)|_{\varphi = k\pi} = |X(\omega)|^2\big|_{\varphi = k\pi} = \frac{b'^2}{(\omega_n^2 - \omega^2)^2 + 4\zeta^2\omega_n^2\omega^2} = \frac{b'^2}{\omega_n^4 + \omega^4 + 2\omega_n^2\omega^2(4\zeta^2 - 2)} \tag{3.8}$$

Where:

$$b' = b \cdot \omega_n\sqrt{1-\zeta^2} \tag{3.9}$$

Notice that the model doesn't include a window filter. This is based on the results from Potts and Tasche, 2010 and Coll, 2016, and the own experience of the Author. The main argument is the short length of the signals compared to the frequencies of interest. In this case, the small number of cycles gathered and the amplitudes of the exponentially damped sinusoids would be considerably perturbed by a window filter, modifying the results from the identification of the modes.

The next step is to calculate the first derivative of the Power Spectrum (equations 3.6 and 3.8), with respect to the angular frequency ω, searching for the frequencies of maximum amplitude and particularized for $\omega = \omega_0$, where ω_0 represents the resonance frequency:

$$\left.\frac{\partial S_x(\omega)}{\partial\omega}\right|_{\substack{\omega=\omega_0 \\ \phi\neq k\pi}} = b^2\left[\frac{2\omega_0(\omega_n^4 + \omega_0^4 + \omega_n^2\omega_0^2(4\zeta^2-2))}{(\omega_n^4 + \omega_0^4 + \omega_n^2\omega_0^2(4\zeta^2-2))^2} - \frac{(\omega_0^2+\alpha^2)(4\omega_0^3 + 2\omega_0\omega_n^2(4\zeta^2-2))}{(\omega_n^4 + \omega_0^4 + \omega_n^2\omega_0^2(4\zeta^2-2))^2}\right] = 0 \tag{3.10}$$

This equation can be simplified by removing the denominator, taking into account that it is a sum of positive numbers and cannot be zero, unless $\omega_n = \omega_0 = 0$, which means no vibration and lies out of our problem constraints.

$$(\omega_n^4 + \omega_0^4 + \omega_n^2\omega_0^2(4\zeta^2-2)) - (\omega_0^2+\alpha^2)(2\omega_0^2 + \omega_n^2(4\zeta^2-2)) = 0 \tag{3.11}$$

Notice that the particular case $\omega_0 = 0$ returns a trivial solution, which in this case can be demonstrated to be a minimum and therefore can be simplified in equation 3.11. The demonstration can be found in section A.6.

At this point we can solve for ω_0:

$$\omega_0^4 + 2\alpha^2\omega_0^2 + \alpha^2\omega_n^2(4\zeta^2 - 2) - \omega_n^4 = 0 \tag{3.12}$$

The solution to this equation is the following:

$$\omega_0 = \sqrt{-\alpha^2 + \sqrt{\alpha^4 - 4\zeta^2\alpha^2\omega_n^2 + 2\omega_n^2\alpha^2 + \omega_n^4}} \tag{3.13}$$

And replacing α from (3.3):

$$\omega_0 = \omega_n\sqrt{-\beta^2 + \sqrt{\beta^4 + 2(1 - 2\zeta^2\ )\ \beta^2 + 1}\ } = \omega_n\ \gamma \tag{3.14}$$

The factor β from equation 3.5 is a function of the phase angle and the damping factor, and is defined only if $\varphi \neq k\pi$. This implies that the resonance frequency ω_0 depends on the natural frequency ω_n, the damping factor ζ and the phase angle φ.

At this point we can calculate the dependency between the resonance frequency and the phase angle, as stated in the beginning of the section.

Please note here that β (see Equation (3.5)) depends on both the damping factor and the phase of the original signal. So, although the resonance frequency is proportional to the natural frequency of the damped signal, it will also depend on both the phase and the damping factor. This dependency makes difficult to directly estimate the natural frequency from the resonance frequency, as one might originally expect. To better understand the degree of dependency of γ with ζ and ϕ we will now study its range of variation.

In general, for underdamped signals we have that $0 \leq \zeta \leq 1$. Then $0 \leq \zeta^2 \leq 1$ and $1 \geq 1 - 2\zeta^2 \geq -1$. So, considering $1 - 2\zeta^2 \leq 1$ we can deduce that $\beta^4 + 2(1 - 2\zeta^2)\beta^2 + 1 \leq \beta^4 + 2\beta^2 + 1$. Taking this into consideration we can establish the upper limit to the value of ω_0:

$$\omega_0 \leq \omega_n\sqrt{-\beta^2 + \sqrt{\beta^4 + 2\ \beta^2 + 1}} = \omega_n \tag{3.15}$$

In this inequation, boundary solution $\omega_0 = \omega_n$ is achieved when $\beta = 0$. So, considering the definition of β given by Equation (3.5), this particular solution will be achieved in the case of $\phi = \phi_1 = -\arctan\sqrt{1 - \zeta^2}/\zeta$. Please, notice that this is true also when $\zeta = 0$ for any value of ϕ.

Now let us look for the lower limit of ω_0. We consider that $(1 - 2\zeta^2)^2 \leq 1$, and thus we can establish that $\beta^4 + 2(1 - 2\zeta^2)\beta^2 + 1 \geq \beta^4 + 2(1 - 2\zeta^2)\beta^2 + (1 - 2\zeta^2)^2$. So, taking again into consideration Equation(3.14) and simplifying we can establish that:

$$\omega_0 \geq \omega_n\sqrt{-\beta^2 + \sqrt{\beta^4 + 2(1 - 2\zeta^2\ )\ \beta^2 + (1 - 2\zeta^2\ )^2}} = \omega_n\sqrt{1 - 2\zeta^2} \tag{3.16}$$

As a conclusion of this demonstration, in general for underdamped signals the resonance angular frequency $\omega_0 \geq \omega_n\sqrt{1 - 2\zeta^2}$. That is, independently on the phase, the frequency of the maximum of the power spectrum will be greater than $\omega_n\sqrt{1 - 2\zeta^2}$. This limit case will be achieved for the particular case of $\phi = \phi_2 = k\pi$, $\forall k \in \mathbb{Z}$ which can be deducted from the maximization of Equation (3.8). In that particular case maximizing the power spectrum implies the minimization of the denominator, which after simplifying leads to $\omega_0^2 + \omega_n^2(1 - 2\zeta^2) = 0$. From this point it is easy to see that effectively the value $\omega_0 = \omega_n\sqrt{1 - 2\zeta^2}$ is the positive solution of this equation.

From these upper and lower limits of ω_0 we can deduce that the estimation of the natural angular frequency ω_n from the amplitude of the power spectrum is not straightforward as some might expect, since the value of the resonance frequency will also depend on the damping factor and on the phase of the signal.

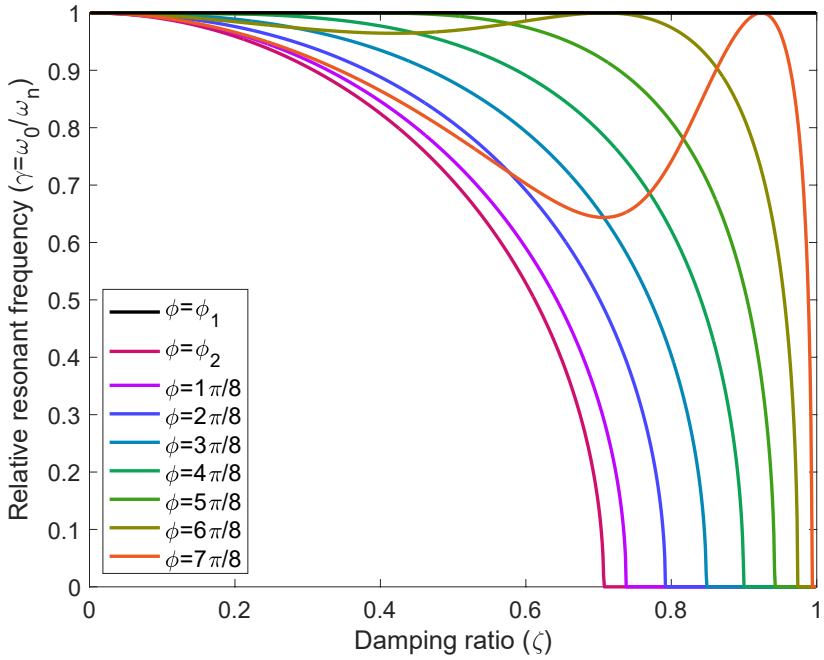

FIGURE 3.1: Relative resonant frequency ($\gamma = \omega_0/\omega_n$) of a single underdamped mode, with respect to the damping factor (ζ) for different phase values (φ).

To better understand these expressions, Fig. 3.1 shows the relationship between the relative resonant frequency ($\gamma = \omega_0/\omega_n$) of a single underdamped mode, and the damping factor (ζ) for different phase values (ϕ). As we can see, the two extreme values obtained with ϕ_1 and ϕ_2 represent both extremes of the curves. It's important to note the strong relationship between the phase angle and the resonance frequency in the power spectrum. This statement will be relevant in the upcoming sections.

3.2.2 Relationship of the bandwidth B with the phase angle φ

Another factor to consider is the 3dB bandwidth B. Ewins, 2000 proposed one method (Peak-Amplitude) to estimate frequencies and dampings from the bandwidth of the power spectrum, but this method doesn't consider the phase angle, and therefore induces quite an amount of error in the identification of the signal. However it is important to analyze the equations of the bandwidth related to the natural frequency, damping ratio and phase angle.

Combining equations 3.6 and 3.14 and simplifying, we reach the following equation for the amplitude of the power spectrum in the resonance frequency $\max\{|X(\omega)|^2\} = |X(\omega_0)|^2$:

$$|X(\omega_0)|^2 = b^2 \cdot \frac{\gamma^2 + \beta^2}{\omega_n^2(1-\gamma^2)^2 + 4\zeta^2\omega_n^2\gamma^2} \tag{3.17}$$

The definition of the 3dB bandwidth is the difference between the frequencies ω_1 and ω_2 corresponding to both sides of the the spectrum peak where the amplitude of these frequencies corresponds to $|X(\omega)|^2/|X(\omega_0)|^2 = 1/2$:

$$\frac{|X(\omega)|^2}{|X(\omega_0)|^2} = \frac{\frac{\omega^2+\omega_n^2\beta^2}{(\omega_n^2-\omega^2)^2+4\zeta^2\omega_n^2\omega^2}}{\frac{\gamma^2+\beta^2}{\omega_n^2(1-\gamma^2)^2+4\zeta^2\omega_n^2\gamma^2}} = \frac{1}{2} \tag{3.18}$$

Which simplifying and solving can be demonstrated to return the following equation:

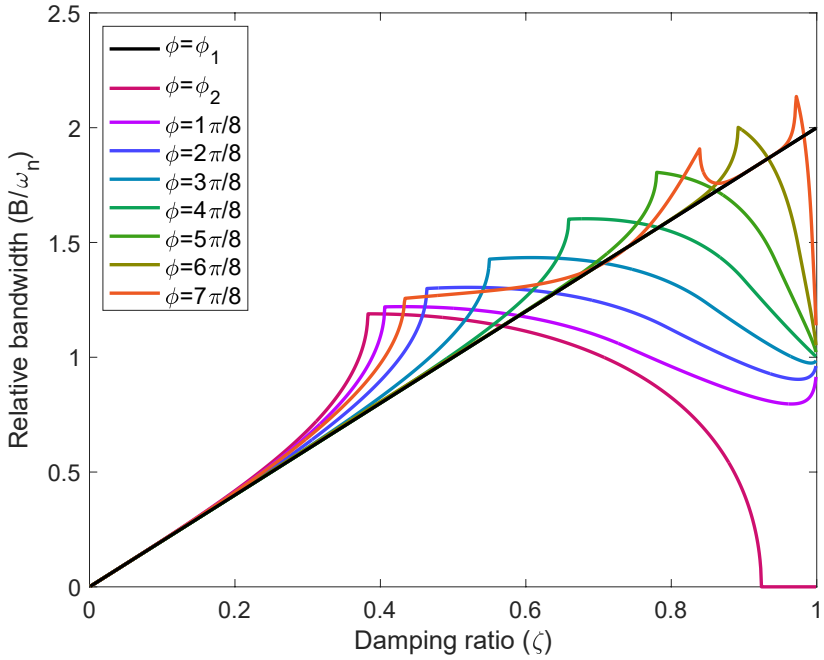

FIGURE 3.2: Relative bandwidth (B/ω_n) of a single underdamped mode, with respect to the damping factor (ζ) for different phase values (φ).

$$\omega^4/2 + g\omega_n^2\omega^2 + h\omega_n^4/2 = 0 \tag{3.19}$$

Where:

$$g = 2\zeta^2 - 1 - \frac{(1-\gamma^2)^2 + 4\zeta^2\gamma^2}{\gamma^2 + \beta^2} \tag{3.20}$$

$$h = 1 - \beta^2\frac{2(1-\gamma^2)^2 + 8\zeta^2\gamma^2}{\gamma^2 + \beta^2} \tag{3.21}$$

The solution of equation 3.19 returns the following values for ω_1 and ω_2:

$$\omega_{1,2} = \omega_n\sqrt{-g \pm \sqrt{g^2 - h}} \tag{3.22}$$

With the corresponding bandwidth B:

$$B = \omega_1 - \omega_2 = \omega_n\left(\sqrt{-g + \sqrt{g^2 - h}} - \sqrt{-g - \sqrt{g^2 - h}}\right) \tag{3.23}$$

That can be simplified as:

$$B = \omega_n\sqrt{2}\sqrt{-g - \sqrt{h}} \tag{3.24}$$

To see the relationship between the phase angle and the bandwidth, we will now consider two particular values for the phase angle:

$$\varphi = \varphi_1 = \arctan\left(-\frac{\sqrt{1-\zeta^2}}{\zeta}\right) \parallel \beta = 0 \implies \gamma = 1 \implies \omega_0 = \omega_n \tag{3.25}$$

$$\varphi = \varphi_2 = k\pi \;\; \| \;\; \omega_0 = \omega_n\sqrt{(1-2\zeta^2)} \tag{3.26}$$

When introducing φ_1 into equations 3.20, 3.21 and 3.24 we get the following expression:

$$B|_{\varphi_1} = \omega_n\sqrt{2}\sqrt{1+2\zeta^2-\sqrt{1}} = 2\zeta\omega_n \tag{3.27}$$

For φ_2 the approach is slightly different, since $\varphi_2 = k\pi$ and corresponds to a particular case of the spectrum. In this case, substituting φ_2 in equations 3.8, 3.20, 3.21 and 3.24, we can obtain the following equation:

$$B|_{\varphi_2} = \omega_n\sqrt{2}\sqrt{1-2\zeta^2-\sqrt{8\zeta^4-8\zeta^2+1}} \tag{3.28}$$

The equations 3.24, 3.27 and 3.28 are plotted in figure 3.2. The figure shows that the bandwidth estimation is not affected by the phase angle at low damping ratios. However as the damping ratio increases, the bandwidth is substantially affected by the phase angle values.

3.2.3 Conclusions of the phase angle impact on the signals identification

Before starting to draw conclusions, it is necessary to recall that the analysis has been performed on one single mode. The close interaction of two modes and the effect of the phase angle on the equations can disturb the estimations, and therefore the technique developed by Ewins, 2000 can not be relied upon as a trustworthy technique in a broad sense.

However, in case that the modes are sufficiently separated as to allow for a discrimination between the 3dB bandwidth of each mode, and the phase angle is small enough, the contribution of such errors is minimal. Under these conditions it is possible to employ this technique to perform a quick estimation of the natural frequency and damping ratio, allowing to use these values as seeds for more complex techniques like the PRESTO algorithm, which will be described in detail in section 3.5.

3.3 Data processing techniques description

The next step is to compare different data processing techniques to get the best processing technique. These techniques will be employed to process synthetically generated data by the model defined by equation 3.1 considering different levels of noise.

It is necessary to stress the importance of the damped sinusoid equation model in this development. Notice that even if the sampled data could be fitted by a different model with higher accuracy (for example an ARMA model), the damped sinusoid 3.1 is the model employed by airworthiness standards like MIL-A-8870C, 1993 and JSSG-2006, 1998, and hence it is necessary to adhere to such model in order to get results compatible with any airworthiness process.

3.3.1 Basic processing techniques

The first set of techniques are simple fitting processes. These techniques will compare processing by three different approximations, Time Series fitting, Complex Spectrum fitting and Power Spectrum fitting, and will follow the same algorithm as depicted in figure 3.3. The process is based upon the acquisition of a set of time series data points. These data can be pre-processed (calculating their Power Spectrum for example) or used as gathered in the form of a Time Series datasets. Then a parametric equation data model will be used to feed the optimization algorithm, which will produce a synthetic dataset. Both datasets, the synthetic and the acquired will feed the fitting function along with a randomly selected seed, which will return a metric of error between both

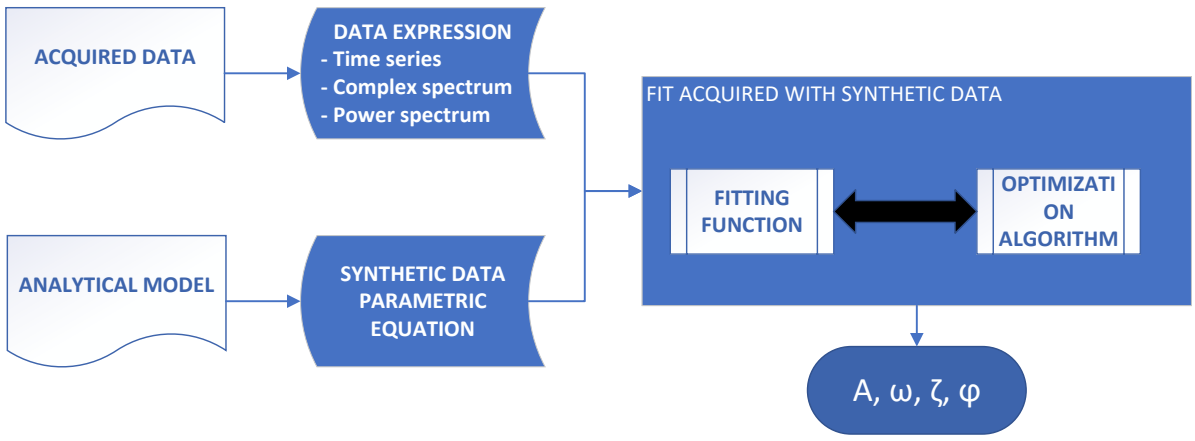

FIGURE 3.3: Data processing algorithm applicable to three different processing techniques, Time Series fitting, Complex Spectrum fitting and Power Spectrum fitting

signals that will also feed the optimization algorithm. The cycle will repeat until any of the stop criteria are met.

Optimization algorithm The optimization algorithm is responsible for selecting the set of solutions that minimize the fitting function. The optimization algorithm employed will be the Trust Region Algorithm, thoroughly described by Coleman and Li, 1996 and Yuan, 2000. It is a fast and robust algorithm that can be applied to ill-conditioned problems, and was selected after a preliminary comparison with other algorithms, say Levenberg-Marquardt and Genetic algorithms.

The Trust Region algorithm is a Quasi-Newton method, based on the assumption that the model function can be approximated to a local manifold in a region close to the seed. Under this assumption, we can define a "trust region" around the seed, typically a hypersphere of a given radius, under which we approximate the model function to a simpler model. Once the model is simpler in that region, we can employ regular Newton methods to calculate the optimum point in that region. In case that the optimum is found, the seed moves to that solution and shrinks the radius of the trust region. Otherwise the radius is expanded.

Fitting function The fitting function is a function that performs an operation on the acquired data and the signal model and returns a metric of error. The fitting function is necessary to feed the optimization algorithm, since the optimization algorithm will find the set of parameters that return the minimum error metric.

In this case the MSE (Minimum Squared Error) metric will be employed. The definition of MSE is as follows:

$$MSE = \frac{1}{N}\sum_{i=1}^{N}(\hat{x}_i - x_i)^2 \tag{3.29}$$

Where $\hat{x}_i$ is a given signal sample from the acquired data, x_i is the respective single point from the model data and N is the total number of points.

3.3.1.1 Time Processing algorithm

This is the most basic approximation. The basic parametric equation (3.1) feeds the optimization algorithm, where it generates a synthetic time series. This synthetic time series, along with the

sampled time series, feed the fitting function and the cycle is repeated until the desired stop criterion is reached. So, in the time domain, the mean square error is defined as $MSE_{time} = E\{(x(t) - \hat{x}(t))^2\}$.

The main disadvantage of this fitness function is that random seeds sometimes converge to local minima, so it is necessary to find an accurate estimator.

3.3.1.2 Complex Spectrum algorithm

As an alternative approach one standard possibility is the use of a fitness function defined in the frequency domain. In this case, the parametric function passed to the optimization algorithm is also equation (3.1). However, after reconstructing the synthetic time series it numerically calculates the complex spectrum and separates the real and imaginary parts. On the other hand, the sampled time series is transformed numerically into a frequency spectrum, also separating real and imaginary parts. The synthetic and sampled data are fed to the fitting function and the cycle is repeated until the stop criterion is reached. So, in this case the fitness function is defined as $MSE_{freq} = E\{|X(\omega) - \hat{X}(\omega)|^2\}$, where $\hat{X}(\omega)$ is the Fourier transform of the measured signal $\hat{x}(t)$ in the form stated above.

With this method convergence problems and local minima are still present. Although the use of frequency responses in which the energy of the signal is concentrated in less samples allows to reduce the amount of frequency terms, reducing the computational cost of the evaluation of the fitness function, the more complex process of extracting the Fourier transform of the signal compensates the increased speed.

3.3.1.3 Power Spectrum algorithm

The power spectrum approximation follows the same approach as the complex frequency approximation, but in this case the power spectrum is numerically calculated from the complex frequency, instead of having both real and imaginary parts separated. The fitting function to be optimized is evaluated from the power spectrum of the signals, $MSE_{spec} = E\{(|X(\omega)|^2 - |\hat{X}(\omega)|^2)^2\}$. This choice tends to reduce the convergence problems, but the solutions achieved sometimes imply a loss in performance with respect to the two first fitness functions.

In this case, as in the *Complex Frequency domain estimation*, it is possible to reduce the amount of frequency terms to be taken into consideration in order to reduce the computational cost of evaluating the fitness function without local minima problems, but the convergence tends to be very slow and requires multiple (usually more than six) runs to converge.

3.3.2 Peak-Amplitude algorithm

Ewins, 2000 described this technique as an extremely fast means to estimate the amplitude and frequency of a single damped sinusoid. However the accuracy of this technique is extremely limited.

It is based on the estimation of the natural frequency as the frequency corresponding to the maximum amplitude in the frequency domain, and the damping is estimated through the 3dB bandwidth of the frequency spectrum as described in section 3.2.2. In this thesis, the technique will be employed mainly to estimate the seeds for different techniques, and the process is as follows:

1. Estimate the natural frequency seed as the peak frequency in the power spectrum
2. Estimate the damping factor, with the 3dB bandwidth and the natural frequency known, solving from equation 3.27. Notice that the usual range of damping factors in real applications is not very different from this estimation

3. Since the phase term ϕ and amplitude a are unknown at this point, they are randomly initialized.

4. Run the Time based estimation with the seeds obtained from the steps above

The proposed estimation approach is sensibly faster than other methods, both classical and proposed by the paradigm, and the experimental results on synthetic data are really promising.

3.3.3 Matrix Pencil algorithm

The description of the Matrix Pencil algorithm was extensively described by Kiviaho, Jacobson, and Kennedy, 2019; Potts and Tasche, 2010; Almunif, Fan, and Miao, 2020 among others, while Barros-Rodriguez et al., 2015 described a very interesting application of the technique to this same problem.

In general the principle behind the technique is somehow similar to the Fourier series, considering that instead of decomposing the signal in sums of sinusoids, the signal is decomposed into sums of damped sinusoids with zero phase angle.

The algorithm is as follows:

- The signals are diagonalized by SVD (Support Vector Decomposition), which is a very efficient algorithm
- The eigenvalues are sorted from higher to lower
- The eigenvalues below a given threshold are filtered and substituted by zero
- The number of modes is reduced in order to get a signal with the number of modes required for our purposes, in this case two modes
- The signal is reconstructed, and from the resulting parameters it is possible to identify the natural frequencies and dampings of each individual mode

The modification introduced by Matrix Pencil over Prony is that instead of decomposing the signals in as many terms as possible, a given number of terms are selected (number of modes above), and the energy of the signal is forced to fit the constraint of such signals. This is performed by calculating the SVD (singular value decomposition) of the data when sorted in matrix form, and the lower energy terms are eliminated. The main drawback of this technique is that the signal terms of the damped sinusoids are forced to have zero phase, and as described in section 3.2 the expectations on this algorithm are limited.

3.3.4 Laplace Wavelet Matching Pursuit algorithm

The Laplace Wavelet Matching Pursuit algorithm has been successfully used by Freudinger, 1989 and Freudinger, Lind, and Brenner, 1997 on F-18 Sine Dwell data. The algorithm is based on a damped sinusoid wavelet atom without phase angle, although the time shift derived from the wavelet processing will account for it. In the case of the Laplace Wavelet Matching Pursuit, the approach followed to calculate the estimation is through Matching Pursuit, as described by Goodwin, 1997; Zhu, 2007. The following elements can be identified in this problem:

- Atom: The atoms are the damped sinusoid signal models, in this case without phase angle: $e^{-\zeta\omega_n(t-\tau)}sin\left(\omega_n(t-\tau)\right)$, where τ represents the time shift.
- Dictionary: The dictionary is the set of all the possible parameter combinations. Considering that the dictionary covers all the possible combinations and that a certain degree of accuracy is necessary, eight parameters as in the case of our problem return an extraordinary number of elements in the dictionary

- Error Metric: In the approach followed to produce the comparison of these methods, the scalar product between the acquired data and the wavelet is considered as the error metric, and the objective is to minimize the error metric to find the best estimation.

The Laplace Wavelet Matching Pursuit technique, as any based on Matching Pursuit, is a greedy technique which will undoubtedly find the optimum solution with the degree of accuracy desired. However the calculation time and computational memory are important limiting factors, and need to be taken into account as a major drawback of this technique.

3.3.5 Deep Learning based estimation

PRESTO and Laplace Wavelet are very similar processing techniques. They rely on the model described in the standards MIL-A-8870C, 1993; JSSG-2006, 1998 and returned a very accurate solution, as shown in the sections above. However the field of Machine Learning has been barely explored for these applications. To date, no study has looked specifically to the identification of flutter related parameters on flight test data.

Regarding the latest similar investigations, Wang and Wang, 2021 employs a method based on DNN to predict the flutter airspeed from the analysis phase (before the flights take place). Zheng et al., 2021 and Duan, Zheng, and Liu, 2019 take a closer approach to the objective of this thesis. They apply CNN models to data extracted from flight tests (in the papers they apply their method to data from wind tunnel tests, but the result is the same). However instead of employing the procedure to identify the parameters of the system, they employ it as a classifier for flutter/no flutter conditions during flight. Possibly Li, Kou, and Zhang, 2019 provides the closest approach to the aim of this thesis with his application of a DNN to flight test data. However again, in his case he employs the technique to model the global behavior of the structure instead of the actual identification of the flutter parameters.

The method proposed is focused on the accurate identification of the flutter parameters of the aeroelastic equations of motion applied to aeroelastic flutter. The main advantages of this method is that once trained, MLPs, DNNs and CNNs provide an almost immediate result with a low end personal computer, which would allow for effective real time results. Also, if the training set includes a range of the parameters broad enough, in theory it would be possible to return accurate flutter parameters not only for two different modes, but also for one or even three. The drawbacks of this method are that a good and accurate model is required in order to provide reliable data, since it is complicated to return accurate values of the parameters for real flight data, the real flight data are very limited in availability for the reasons described above and models with more modes or parameters require larger datasets and computational means to train the networks. That been said, the potential of this technique is colossal, and it is worth exploring in order to develop accurate trained networks with the advantages described above.

In the upcoming sections, three different kinds of deep learning algorithms will be developed:

- Multi-layer perceptrons
- Deep Neural Networks
- Convolutional Neural Networks

The characteristics of the networks will be described below.

3.3.5.1 Multi-Layer perceptrons

The Multi-layer perceptron networks (MLPs) consist on a set of one input layer, in our case with 140 samples, one hidden layer with a different number of perceptrons (neurons) for each network and one output layer, with 4 neurons. An example of these networks can be seen in figure 3.4.

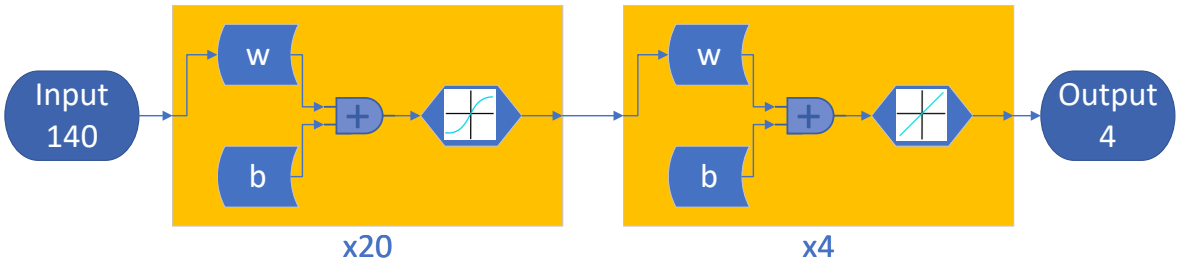

FIGURE 3.4: Multi Layer Perceptron sample network. In this case the MLP with 20 neurons is depicted.

Detailed description of MLPs are out of the scope of this thesis. However, for more information, the excellent book by Goodfellow, Bengio, and Courville, 2017 can be consulted.

3.3.5.2 Deep Neural Networks

The Deep Neural Networks (DNNs) are an extension of the MLP networks. In this case the network comprises more than one hidden layer, but will follow exactly the same approach as MLP networks in section 3.7.2 above. Also describing DNNs is out of the scope of this thesis. More information can be found in Goodfellow, Bengio, and Courville, 2017. An example of the structure of a DNN can be found in figure 3.5. As in the case of the MLPs, our application will also consider 140 input samples and 4 outputs, with a different number of hidden layers.

3.3.5.3 Convolutional Neural Networks

Convolutional Neural Networks (CNNs) are also similar to DNNs. A thorough description of CNNs is out of the scope of this thesis, but detailed information can be found in Goodfellow, Bengio, and Courville, 2017. Nevertheless, suffice to say that the main differences with DNNs are the way to calculate the output parameters, through a convolution between the input matrices and the different layer parameters matrices, instead of the composition of linear applications. The complete block diagram of a CNN with two hidden layers is depicted in figure 3.6. Although this model is not unique, this is the one that will be used in this thesis. In this example only two hidden layers are described, each layer including different steps. The complete process applied to our system is described below:

1. Input layer. The inputs are one matrix for each dataset. The data needs to be presented in the form of a matrix meaningful of a regular pattern. For example, an image.
2. Convolutional block. The convolutional blocks consist of a convolutional layer followed by a series of processes to improve the quality of the operation.
   (a) Convolutional layer. This layer performs the convolution operation on the input matrix with the weights matrix.
   (b) Normalization process. This step normalizes the outputs in order to control the range of the outputs and prevent saturation. A bias is added and a multiplier is applied to the output. These parameters are subjected to training as part of the training process.
   (c) Rectification process. The negative values are converted into zero.
   (d) Pooling process. The convolution matrices are downsampled by smaller windows.

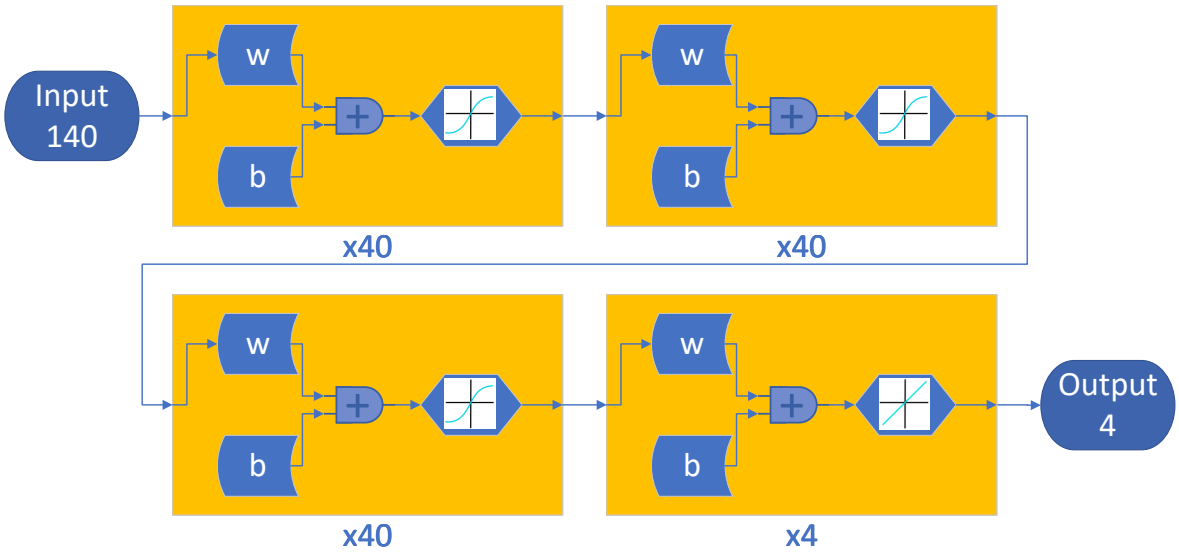

FIGURE 3.5: Deep Neural Network sample. In this case a DNN with one input layer, three hidden layers and one output layer is depicted. In this case each hidden layer has 40 neurons

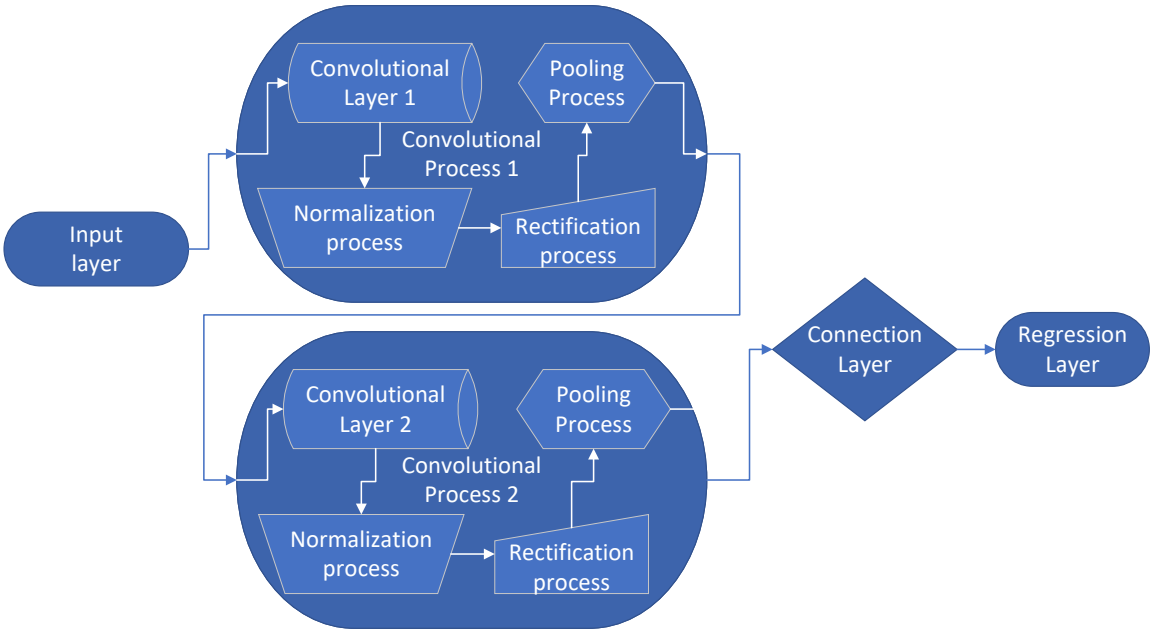

FIGURE 3.6: Convolutional Neural Network sample. In this case a CNN with one input layer, two convolutional layers, one connection layer and one regression layer is depicted. Each convolutional network has a different number of neurons in their convolutional layers (in each convolutional process) and a different number of convolutional processes.

3. Connection layer. In this layer, all the outputs from the last convolutional block are connected and reduced to the 4 output parameters described in section 3.7.1. This layer constitutes a classical perceptron layer, employed to gather the outputs from the convolutional layers and return an output to solve the regression problem.

4. Regression layer. Before returning the raw parameters it is necessary to include a regression layer.

In this example only two hidden convolutional blocks have been depicted. More (or less) blocks can be connected. In fact, in this thesis the trained CNNs employ 5 and 6 hidden layers for different networks.

3.4 Verification and comparison of the classical techniques with synthetic data

The comparison process will take into account separately the classical and the deep learning techniques. Note that the classical techniques have been already studied and analyzed, while the deep learning techniques are a novel application to this field, and therefore the approach to follow will be to compare separately the classical techniques and the deep learning processes. In fact, further on a processing technique will be proposed based, on the fact that the classical techniques allow some room for improvement. The best techniques will be compared further on among them.

Without further ado, we need to verify the different classical techniques presented above. To do so, we need data that is well identified with reliable parameters. Given that, as stated above, there is not any validated technique, we will employ synthetic data.

The synthetic datasets were generated from model equation 3.1 limited to two different modes:

$$x(t) = \sum_{j=1}^{K} a_j \cdot e^{-\zeta_j \omega_{nj} t} \sin\left(\omega_{dj} t + \varphi_j\right) + \nu(t) \tag{3.30}$$

And the following constraints:

- Algorithms:
  - Time Series algorithm
  - Complex Spectrum algorithm
  - Power Spectrum algorithm
  - Matrix Pencil algorithm
  - Laplace Wavelet Matching Pursuit Algorithm
  - Peak-Amplitude algorithm
- Metrics:
  - Average error (Frequency estimations)
  - Root Mean Square Error (Damping estimations)
  - Computational cost (processing time)
- Parameters:
  - Sampling Frequency: $f_s = 85\text{Hz}$
  - Signals length: $t = 5s$
  - Natural frequency: $3.0Hz \leq f_n \leq 6.0\text{Hz}$

  - Damping factor: $0.03 \leq \zeta \leq 0.20$
  - Phase angle: $0.00 \leq \varphi \leq 2 \cdot \pi$
  - Amplitude: $0.01 \leq a \leq 0.50$
  - White gaussian noise SNR: $0dB, 5dB$, 10dB
  - Number of signals: 10.000

- Stop criteria for Basic processing techniques (each run):
  - $MSE \leq 10^{-20}$
  - *Tolerance between consecutive* $MSE \leq 10^{-20}$
  - *Finish* 10 *runs with* 1000 *iterations each run*

The generation of signals with simulated data was performed assuming the interaction of two different modes, and considering different levels of noise, as described in the list above. The stop criteria for the basic processing techniques were (after 10 runs):

- $MSE \leq 10^{-20}$
- *Tolerance between consecutive* $MSE \leq 10^{-20}$
- *Finish* 10 *runs with* 1000 *iterations each run*

The seeds for the estimations were chosen randomly.

Regarding the Power Spectrum and Complex Frequency algorithms, the data were filtered removing frequencies above 14Hz

At last, for Matrix Pencil, Peak-Amplitude and Laplace Wavelet Matching Pursuit algorithms, given the nature of those processing, it was not necessary to perform 10 runs or 1000 iterations or selecting a stop criterium. Instead one single run was enough to finish the estimation, and for that reason the plots show one straight line where the other techniques show an evolution for each run.

Matrix Pencil algorithm was run with a selected order of 200 while the order was reduced by 196, leaving an order of 4 in the final estimation, similar to the calculations made by Almunif, Fan, and Miao, 2020; Potts and Tasche, 2010; Kiviaho, Jacobson, and Kennedy, 2019. Once obtained the estimations, in order to select the best match in frequency and damping it was necessary to select the best 2 modes estimated. One first attempt to filter by energy, as described by Patel et al., 2013, was attempted with unsatisfactory results. Given the error in the estimations, the closest match in frequency to the original values were selected from the estimated modes.

The Laplace Wavelet Matching Pursuit algorithm was selected given the extreme interest of the bibliography. Freudinger, Lind, and Brenner, 1997 developed the technique and validated it against real F-18 datasets from flutter flight tests.Given the greedy nature of the Matching Pursuit process, a reduced dictionary was employed, limiting the values to the range of parameters employed for the generation of signals. The time delay range was $[-5.0 \ +5.0]$ seconds.

The results are reflected in table 3.1

Results and discussion After running the estimation algorithm, the results can be seen in figures 3.7 and 3.8, while the numerical values are included into table 3.1. In these two cases the numerical results were obtained identifying synthetic datasets. The details of such analysis can be found in section 3.4 above. The plots show respectively the average relative error in the natural frequency estimation f_n, calculated as the mean of all the absolute errors between the real and estimated results deducting the worse 10% of the errors, and Root Mean Square Error (RMSE) in the damping factor ζ estimation for a SNR of 5dB, calculated as the RMSE between the real and estimated

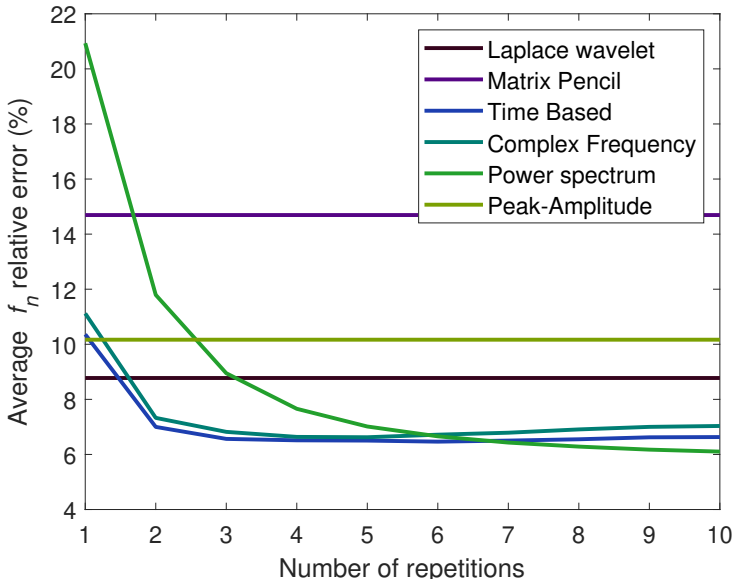

FIGURE 3.7: Plot depicting the estimated natural frequency average relative error in percentage. The data were produced with a SNR of 5dB removing the worst 10% estimations.

parameters of all the datasets, also deducting the worse 10% errors. The table shows the values of the errors described above, the processing time and also the number of runs for each estimation. The calculations were made using a single 2.5GHz CPU with 8 cores.

Analyzing the results from table 3.1 and figures 3.7 and 3.8 we can draw the following conclusions:

- Basic processing techniques: There are three basic processing techniques, say Time Series estimation, Complex Frequency estimation and Power Spectrum estimation.
  - Time Series estimation: This estimation can reach precise estimations after approximately 6 runs. The drawback is that it is prone to get stuck in local minima, reaching an asymptote after approximately six runs, and therefore it is necessary to get a precise estimation of the seeds before the initial kick is run. It is relatively fast, and in total the final estimation (after 6 runs) took an average of 4.1 seconds for each set of data, the fifth among seven, but still suitable for real time identification. With the lower levels of noise (10dB), the error estimation in frequency (4.08%) and damping (0.029 $RMSE$) were the second best out of seven estimations. However, as noise level increases up to 0dB the error increases as well, and the ranking reduces from the second position to the fourth in frequency (10.43%) and third in damping (0.061 $RMSE$), this last together with the peak-amplitude estimation. In general this is a fast technique with reasonably good results, but the estimation is very dependent on the quality of the signal, and the accuracy of the identification decreases as the noise increases.
  - Complex Frequency estimation: This technique is very similar in results to the Time Series estimation. In fact the estimation curves of error run parallel. It also took 6 runs to get accurate results with the same drawbacks, affinity for local minima, and the time employed is slightly higher than the Time Series estimation, 6.2 seconds and sixth in the ranking. As in the previous case, this entitles the technique for real time identification. The errors under the lower levels of noise (10dB) score the third position in damping estimation (0.030 $RMSE$) and fourth in frequency (4.21%). However, as in the previous

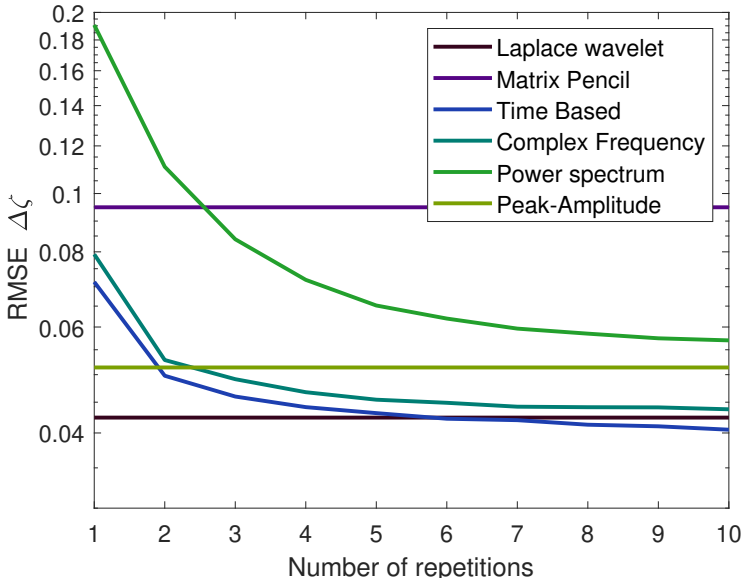

FIGURE 3.8: Plot depicting the estimated damping factor root mean square error (RMSE) in logarithmic scale. The data were produced with a SNR of 5dB removing the worst 10% estimations.

SNR	Time Series	Complex Freq.	Power Spec.	Matrix Pencil	Peak Amp.	Laplace Wav.
			Avg. Err. f_n			
10dB	4.08 %	4.21 %	4.10 %	14.69 %	10.12 %	8.75 %
5dB	6.41 %	6.78 %	6.16 %	14.69 %	10.17 %	8.78 %
0dB	10.43 %	11.10 %	9.27 %	14.69 %	10.76 %	8.82 %
			RMSE ζ			
10dB	0.029	0.030	0.042	0.095	0.049	0.042
5dB	0.042	0.044	0.057	0.098	0.051	0.042
0dB	0.061	0.067	0.078	0.095	0.061	0.043
			Time/set			
	$4.1{\cdot}10^{0}$ s	$6.2{\cdot}10^{0}$ s	$2.6{\cdot}10^{1}$ s	$1.0{\cdot}10^{-2}$ s	$5.0 \cdot 10^{-5}$ s	$6.0{\cdot}10^{-2}$ s
			Number of runs			
	6	6	10	1	1	1

TABLE 3.1: Results of running different estimation algorithms over synthetic datasets. The metrics are: Time required to estimate each set of data, Natural frequency average error (in percentage) and damping factor Root Mean Square Error deducting the worse 10% errors.

case the estimation gets worse as the noise level increases. In the higher levels of noise (0dB) the ranking lowers to the fifth in frequency (11.10%) and damping (0.067 $RMSE$). As in the previous case, the estimation is very sensitive to noise, although it is fast and allows for real time signal identifications.

– Power Spectrum estimation: This estimation is sensibly different to the previous two estimations. In this case the technique is somehow insensitive to local minima. The convergence to the global minimum is slow but steady. In this case the simulation was stopped after 10 runs due to the high amount of time required, 25.6 seconds in average for each set of data, but the trend showed a slow convergence. Under low noise (a SNR of 10dB) the results ranked the third best score in frequency estimation (4.10%) and fourth in damping (0.042 $RMSE$). These results improved slightly for high levels of noise (0dB) in the case of the frequency estimation, ranking the third out of seven with a relative error of 9.27%, but sensibly worse for the damping estimation ranking sixth out of seven (0.078 $RMSE$). The only advantage of this technique is the resilience before local minima, although the long time required bars it from real time identification.

- Matrix Pencil estimation: This estimation returns very bad results both in frequency and damping identification. In fact is the worse of all the estimations regardless of the levels of noise. It is necessary to indicate that the technique had to be adjusted several times in order to get a level of error compatible with the rest of the techniques, but even after multiple attempts the error levels were an outlier compared to the others, reaching the best results with 200 modes and filtering 196 signals (keeping 4 signals for the reconstruction and choosing the best match among them). The advantages are the fast speed, second best among the seven estimations with 0.01 seconds and repeatability of results regardless of the level of noise.

- Peak-Amplitude estimation: This is an extremely fast and basic technique, and surprisingly the results are very good considering the short time required to reach them. The time required is 3 orders of magnitude faster than the next fastest technique ($5 \cdot 10^{-5}$ seconds). Under high SNR (10dB) the frequency and damping errors are bad compared to the other techniques. Sixth in frequency (with 10.10% relative error) and damping (with 0.049 $RMSE$), but the technique is insensitive to noise, keeping steady values of frequency error under low SNR (0dB), with a relative error of 10.76% staying in the sixth position, and rising to the third position in damping estimation (0.061 SNR). These results are bad compared to the others, but considering the short time required to reach them and the insensitivity to noise factors, it may be used to seed other more complex techniques.

- Laplace Wavelet Matching Pursuit estimation: This is a very important technique to consider. Freudinger, 1989 validated this technique on real F-18 data, which is the same source as the data available for this study. Regarding the time required in this case, even though the results are very good compared to the others with 0.06 seconds, the technique had a very reduced dictionary matching the exact conditions employed to generate the data, given the limitations in memory of the computers available to run the simulation, considering all the atoms in a broad dictionary. Under simulated data and low noise (10dB SNR), the results ranked the fifth in frequency relative error (8.75%) and fourth in damping (0.042 $RMSE$). However, the technique is extremely insensitive to noise, getting almost the same results for high noise conditions (0dB SNR), and reaching the second best match in frequency estimation (8.82% relative error) and the best match in damping (0.043 $RMSE$). Even thought the system has time and computational limitations under unknown conditions, it is possible to estimate the parameters with other techniques to reduce the dictionary or improve the means of calculation, if computer clusters are available.

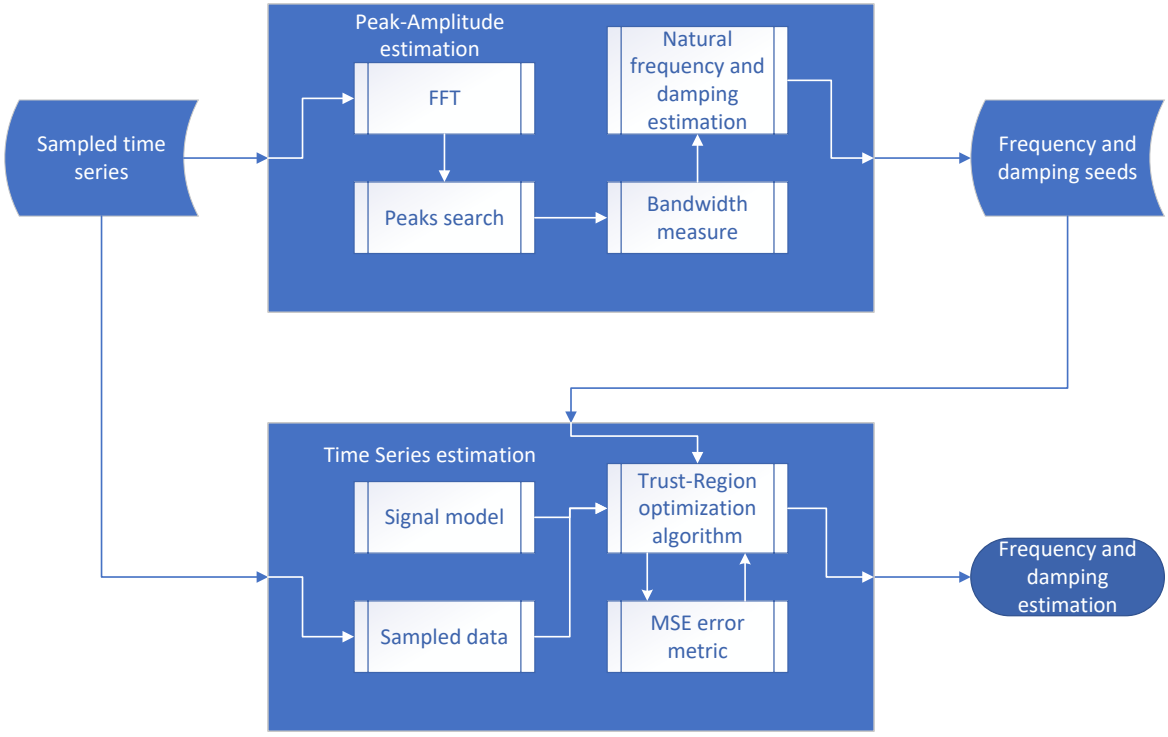

FIGURE 3.9: PRESTO block diagram

3.5 Proposed Data Processing algorithm. PRESTO algorithm

The PRESTO algorithm has been developed taking into account the strong points and problems derived from the previous techniques as will be seen in section 3.9. The PRESTO algorithm stands for Power Spectrum Short Time Optimization.

The Time Series algorithm (and similarly the Complex Spectrum) demonstrates to be very sensitive to initial conditions, due to the tendency to converge on local minima, although it shows a very fast pace of convergence. On the other hand, the Power Spectrum algorithm tends to a very slow convergence, but is more insensitive to local minima.

The algorithm is as follows:

- The Peak-Amplitude algorithm 3.3.2 will be employed to find the seeds of the initial kick
- The Time Processing algorithm 3.3.1.1 will be employed to calculate the actual optimum values from the seeds in the step below
- In case of considering to use several runs, the results from the previous step will be used to seed the next run

This algorithm is summarized in the diagram 3.9

The sampled data is processed through the Peak-Amplitude algorithm (as described in section 3.3.2) to get the seeds of the frequencies and amplitudes of interest. This step is paramount for the analysis that follows, since the tendency of the Time Series estimation to get stuck in local minima requires a good approach to the final solution. Once the seeds are obtained they feed the Time Series estimation as described in 3.3.1.1. The signal model employed is 3.1 assuming only two

different modes, and the optimization algorithm the Trust Region algorithm, described in section 3.3.1. The fitting function employed is the Mean Square Error, as described in section 3.3.1.

The assumption of two different modes is important. The interaction between two different modes (classically bending-torsion for wing flutter) is what favors the apparition of the flutter phenomenon. Although in real operations the deformations are not usually so clear as bending-torsion deformations, flutter in real operations most commonly appears as the interaction of two orthogonal modes, either in modal or physical coordinates. Another point to consider is that two modes allow to indistinctly model the system as structural or viscous damping as described in section 2.3.2.2, and therefore the damping model is not a factor of controversy.

3.5.1 PRESTO vs. Laplace Wavelet Matching Pursuit

When comparing the Laplace Wavelet Matching Pursuit to the PRESTO algorithm it is clear that both models are equivalent. We can develop the equations with one degree of freedom for simplicity in equation 3.31, but the results can be easily extrapolated to multiple degrees of freedom (multiple natural modes):

$$Ae^{\omega_n 2\pi(t-\tau)}sin(\omega_d 2\pi(t-\tau)) = Ae^{\omega_n 2\pi t-\omega_n 2\pi\tau)}sin(\omega_d 2\pi t-\omega_d 2\pi\tau) = Be^{\omega_n 2\pi t}sin(\omega_d 2\pi t-\varphi) \tag{3.31}$$

The reason why both fitting algorithms are different relies in the way to calculate the estimations. The PRESTO algorithm solves an optimization problem by getting through an optimum path to the solution. However, the Laplace Wavelet Matching Pursuit algorithm uses Matching Pursuit to reach the solution. This solving technique is a greedy algorithm, meaning that it evaluates all the possible combinations of parameters to reach the optimum solution. This fact is important because each mode has a set of 4 different parameters to optimize, and therefore adding new modes increases the number of combinations as a power of four. So, assuming a very broad estimation with an average resolution of 10 different points for each parameter, applying the Laplace Wavelet Matching Pursuit to one single mode results in the evaluation of 10^4 different sets of parameters, but two modes imply 10^8 evaluations, which starts to be close to the edge of a manageable number of evaluations with a regular computer for real time evaluations. A reasonable estimation would require an average of 100 different points per parameter, meaning that one mode would require 10^8 evaluations and two modes 10^16 evaluations, this last option being totally out of reach for a regular computer to provide an assessment in real time.

For this reason the Laplace Wavelet Matching Pursuit evaluates the modes one by one, while the PRESTO algorithm evaluates several modes at the same time, both requiring a similar amount of time to process data in real time under those conditions.

The difference of evaluating the modes one by one or both at the same time is important. In the case of the Laplace Wavelet Matching Pursuit the first mode can be calculated with very good accuracy, but the residual of the original signal without the first mode includes the contribution of the second mode plus the proportional contribution of noise from the first mode as demonstrated by Abou-Kebeh LLano, 2013, and therefore contributing to a worse estimation of the second mode. However, the PRESTO algorithm reaches the optimum solution considering the contribution of both modes at the same time, and hence reducing the residual error between the reconstructed and the original signals.

This fact explains that signals where the contribution of one single mode is larger than the second get much better accuracy with Laplace Wavelet Matching Pursuit than PRESTO, while signals where clearly two modes are involved get better accuracy with PRESTO.

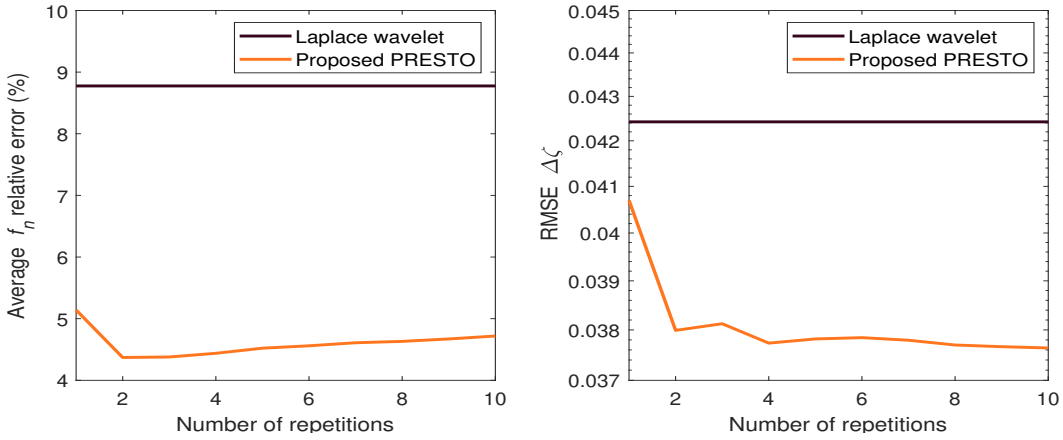

FIGURE 3.10: Plot depicting the estimated natural frequency average relative error in percentage and the Root Mean Square Error (RMSE), comparing the Laplace Wavelet and the PRESTO techniques. The data were produced with a SNR of 5dB removing the worst 10% estimations.

3.6 Verification of the PRESTO algorithm with synthetic data and comparison with Laplace Wavelet Matching Pursuit

We will now compare the results from both techniques, PRESTO and Laplace Wavelet on synthetic datasets. As stated above, the Laplace Wavelet Matching Pursuit is an already validated technique with the same set of data as the ones available to the Author. This fact alone entitles the technique for comparison with the proposed technique. Also, from the results of table 3.1, even though there are techniques that may perform better under 5dB SNR conditions, the great advantage of the Laplace Wavelet is its stability under different noise conditions.

These results indicate a better accuracy of the PRESTO estimation both in natural frequency and in damping when data were generated at 5dB SNR. Figures 3.10 left and right show a comparison of both techniques. Note that the PRESTO estimation was running for the full 10 runs, and in particular the minimum is reached after 2 repetitions for the frequency estimation. Even though the damping reached a better estimation after 10 runs, the difference between 2 runs and 10 runs is absolutely minimum (one order of magnitude smaller than the expected damping resolution), and therefore it is recommended to limit the total number of runs to only 2, since the frequency estimation can get worse, the damping estimation will not suffer an appreciable improvement and the computation time will be greatly improved.

Table 3.2 shows a comparison of the results for both techniques at different SNR values. Notice that the Laplace Wavelet results show a good resilience and almost no variation at different SNRs, and this statement is applicable to both frequency and damping estimations. However, the PRESTO estimation is very sensitive to noise. The results at 10dB SNR show a 4% better accuracy than at 0dB SNR in the frequency estimation. May seem a small difference anyways, but note that when estimating at 0dB SNR signals, the estimation has only a 2% difference with the Laplace Wavelet estimation. The case of the damping is still more interesting. At 5dB and 10dB SNR, the error in damping for the PRESTO estimation is sensibly better than the Laplace wavelet. However the estimation at 0dB SNR turns the tides. The PRESTO estimation is worse than the Laplace Wavelet.

These conclusions from the data processed support the statement above. The Laplace Wavelet technique is more robust (at least insensitive to noise) than PRESTO, although depending on the SNR of the signals involved, the estimation in PRESTO may be better.

SNR	Laplace Wav.	PRESTO
	Avg. Err. f_n	
10dB	8.75 %	2.84 %
5dB	8.78 %	4.37 %
0dB	8.82 %	6.82 %
	RMSE ζ	
10dB	0.042	0.026
5dB	0.042	0.038
0dB	0.043	0.055
	Time/set	
	0.06 s	0.06 s
	Number of runs	
	1	2

TABLE 3.2: Results of running Laplace Wavelet and PRESTO algorithms over synthetic datasets. The metrics are: Time required to estimate each set of data, Natural frequency average error (in percentage) and damping factor Root Mean Square Error.

Regarding the time employed to run both methods, both took a very similar time. However it is important to remark that the Laplace Wavelet is a greedy algorithm, and therefore it was necessary to limit the search dictionary to the same range of the parameters employed for the training set, given the memory limitations of the means available for running the algorithm. For this reason, the times are not representatives of the actual workload of the Laplace Wavelet algorithm. In a real case where it would be necessary to run a broader set of parameters, it is complicate to estimate if the technique would take longer or shorter to run, since the range of parameters undoubtedly should have to be increased, but also the computing power should be increased. However it is safe to say that under the same conditions, range of parameters and computing power available, the PRESTO algorithm would most likely be substantially faster than the Laplace Wavelet algorithm, since the search subspace would be in the order of N^8 (where N is the average number of points for all the parameters) for the Laplace Wavelet algorithm, while for the PRESTO algorithm, assuming a pessimistic scenario, the number of steps would probably increase in the order of 10^3 in absolute number of steps.

3.7 Verification and comparison of the Deep Learning techniques with synthetic data

The current section will describe the process followed to train the different networks employing synthetic data.

3.7.1 Design data and feature extraction

The training datasets were based on the following equation 3.1:

$$x(t) = \sum_{j=1}^{K} a_j \cdot e^{-\zeta_j \omega_{nj} t} \sin\left(\omega_{dj} t + \varphi_j\right) + \nu(t) \tag{3.32}$$

For this training set only two different modes have been employed with the following parameters:

- Sampling Frequency: $f_s = 85$Hz
- Signals length: $t = 5s$
- Natural frequency: 3.0Hz$\leq f_n \leq$ 6.0Hz
- Damping factor: $0.03 \leq \zeta \leq 0.20$
- Phase angle: $0.00 \leq \varphi \leq 2 \cdot \pi$
- Amplitude: $0.01 \leq a \leq 0.50$
- White gaussian noise SNR: 0dB, 5dB, 10dB
- Number of design signals: 300.000 (considering the three levels of noise, 100.000 signals each)
- Training set: 80% of the total number of design signals
- Validation set: 20% of the total number of design signals
- Cutout samples (frequency domain): 70 samples (14Hz)
- Scale factor for damping: $x15$

The input parameters will be discussed for each network independently. However the output parameters are the same for all the networks.

- Mode 1 natural frequency [Hz]
- Mode 2 natural frequency [Hz]
- Mode 1 damping factor [Hz] (scaled $x15$ to balance with frequencies)
- Mode 2 damping factor [Hz] (scaled $x15$ to balance with frequencies)

The training was performed with the "Universidad de Alcalá, Teoría de la Señal y Comunicaciones" department investigation workstation, a low end workstation but powerful enough to perform the training of the networks described below in a reasonable amount of time. Given the limited resources, it was not possible to increase the number of output parameters or the number of signals to be considered. For example, the range of frequencies is limited to only 6Hz. It would have be interesting to increase the range of frequencies to at least 10Hz, to cover the actual range of cases expected with real data, and the dampings to include the value of 1 for the damping factor, to effectively account for one single signal (although the approximation with damping 0.2 is probably close enough). The extension of such data ranges can be subject for further investigations. Also note that the amplitude and phase angle are not calculated in these networks. The reason is the same as above. Including these two extra parameters would mean to increase from 4 to 8 the number of parameters in the output layer, and this would require a much larger dataset than reasonably available for the means (computational power) available. This factor can also be subject for further investigations.

For the error metrics, as in the case of the classical processing techniques, the estimation of the natural frequency f_n was calculated measuring the average absolute error (%) between the real and returned parameters. The estimation of the damping factor ζ was performed by calculating the Root Mean Square Error (RMSE) between the real ans synthetic data. The error was calculated by removing the worst 10% result on the validation dataset.

SNR	MLP 20	MLP 40	MLP 60	MLP 80	MLP 100
			Avg. Err. f_n		
10dB	5.94 %	5.04 %	4.58 %	4.34 %	4.28 %
5dB	6.17 %	5.34 %	4.93 %	4.71 %	4.71 %
0dB	6.90 %	6.25 %	5.97 %	5.82 %	5.85 %
			RMSE ζ		
10dB	0.029	0.026	0.026	0.025	0.024
5dB	0.030	0.027	0.027	0.026	0.026
0dB	0.032	0.030	0.029	0.029	0.029
			Time/set		
	0.011 ms	0.012 ms	0.015 ms	0.018 ms	0.022 ms

TABLE 3.3: Summary table of MLP trained networks. Each column indicates the type of network (MLP) and the quantity of neurons in the hidden layer.

3.7.2 Multi-layer perceptron training process and results

The 140 samples of the input layer are constructed similarly to the Complex Spectrum processing algorithm 3.3.1.2 with slight differences:

1. Cut the original time series signal to 5 seconds samples, or zero-pad until 5 seconds of signal are reached.
2. Calculate the DFT of the time series signal.
3. Separate the real and imaginary parts of the signal spectrum into two different sequences, S_R and S_I.
4. Cut each of these sequences for the first 70 samples in the positive part of the spectrum ($S_r = S_R[2:71]$, $S_i = S_I[2:71]$, first sample removed to prevent zero frequency outliers).
5. Construct one final signal with the previous sequences ($S_f = [S_r, S_i]$).
6. Process the final signal S_f into the input layer.

The output layer will return 4 different outputs as indicated in section 3.7.1 above:

1. Mode 1 natural frequency
2. Mode 2 natural frequency
3. Mode 1 damping factor
4. Mode 2 damping factor

These outputs will be compared with the true values employed to generate the training dataset, and trained through back-propagation algorithms with a Levenberg-Marquardt optimization algorithm.

A total of 5 different MLPs have been trained, with 20, 40, 60, 80 and 100 neurons each, with the results shown in table 3.3 and figure 3.11:

The results indicate that the MLP with 100 neurons in the hidden layer has the lowest error, although all the MLP networks have a similar level of error. That been said, comparing the 80 and 100 neurons networks errors there is almost no difference between both, and is possible that the results might be reversed (in terms of errors) with a different training or validation set. It is

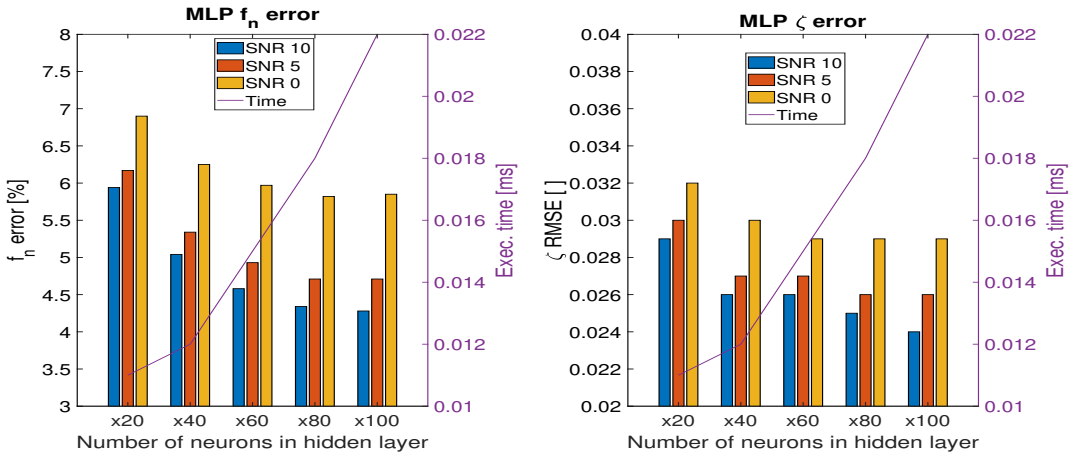

FIGURE 3.11: Plot depicting the estimated natural frequency average relative error in percentage [%] and the Root Mean Square Error (RMSE) in absolute value, comparing MLP networks composed of different number of neurons. The secondary "y" axis plots the execution time required for each network in [ms]. The networks were trained with 0dB, 5dB and 10dB SNR data, removing the worst 10% estimations on the validation dataset.

interesting to note also that the results of the damping error are heavily resilient to noise. Regardless of the SNR level, the results are very similar in terms of error relative to the true training values. Note that the amplitude or the phase angle have not been calculated. The reason not to is described in section 3.7.1.

At last, the calculation times for each dataset are extremely fast, as expected for this kind of processes. However we must return to the comparison between the 80 and 100 neurons networks. In this case the execution time for both networks is different, being the 80 neurons noticeably lower than the execution time of the 100 neurons network. From this point of view, it is worth considering the 80 neurons network as the fittest MLP candidate.

3.7.3 Deep Neural Network training process and results

These networks offer more accuracy than the MLP networks, although they are also more complicated to train (either more computational power or more training time). As described in section 3.7.1 some parameters are left aside, in particular the phase angle and the amplitude.

The input data is generated in the same way as in section 3.7.2, with 140 samples introduced in the input layer and reproduced here for clarity:

1. Cut the original time series signal to 5 seconds samples, or zero-pad until 5 seconds of signal are reached.
2. Calculate the DFT of the time series signal.
3. Separate the real and imaginary parts of the signal spectrum into two different sequences, S_R and S_I.
4. Cut each of these sequences for the first 70 samples in the positive part of the spectrum ($S_r = S_R[2:71]$, $S_i = S_I[2:71]$, first sample removed to prevent zero frequency outliers).
5. Construct one final signal with the previous sequences ($S_f = [S_r, S_i]$).
6. Process the final signal S_f into the input layer.

SNR	DNN 2x(20)	DNN 2x(40)	DNN 2x(60)	DNN 2x(80)	DNN 2x(100)
			Avg. Err. f_n		
10dB	3.92 %	3.17 %	3.00 %	2.96 %	3.08 %
5dB	4.27 %	3.62 %	3.50 %	3.50 %	3.66 %
0dB	5.32 %	4.81 %	4.74 %	4.78 %	4.95 %
			RMSE ζ		
10dB	0.025	0.022	0.021	0.021	0.021
5dB	0.026	0.023	0.022	0.023	0.023
0dB	0.028	0.027	0.027	0.027	0.028
			Time/set		
	0.010 ms	0.014 ms	0.015 ms	0.018 ms	0.021 ms

TABLE 3.4: Summary table of DNN trained networks with two hidden layers and one output layer. Each column indicates the type of network (DNN) and the quantity of neurons in each hidden layer.

The output layer will return 4 different outputs also, as indicated in section 3.7.1 above:

1. Mode 1 natural frequency
2. Mode 2 natural frequency
3. Mode 1 damping factor
4. Mode 2 damping factor

The system was fed with the validation dataset, and the outputs were be compared to the input data. Back-propagation algorithms were used to train the networks with a Levenberg-Marquardt optimization algorithm.

In this case two different sets of networks have been trained, with two hidden layers plus one output layers, and with three hidden layers plus one output layer. In all the cases the hidden layers have the same number of neurons, and the results are compiled in tables 3.4 and 3.5, supported by figures 3.12 and 3.13.

Table 3.4 shows the results for DNNs trained with two hidden layers, each with 20, 40, 60, 80 and 100 neurons. Unlike the MLP networks, the higher number of neurons doesn't necessarily correlate with a better fit. In this case (2 hidden layers DNN), under noisy conditions (0dB) the best fit is reached with a DNN 2x(60). The fact that the 80 and 100 neurons layers perform worse is most probably due to overfitting during the training process.

Note that there is also an important reduction in the execution time. With more than 60 neurons, the execution time experiences a noticeable increase, which contributes to support the statement of choosing the 60 neurons network as the most suitable candidate.

Comparing the results between MLPs and 80 neurons, and DNNs with 2 hidden layers and 60 neurons per hidden layer, the DNN produces substantially better results than the MLP, both in frequency and damping estimation. However, the damping estimation is not so critically increased in the estimation accuracy. Also, the processing time is approximately slightly faster in the MLP than the DNN.

Table 3.5 shows results for DNNs with three hidden layers, like in the previous case each with 20, 40, 60, 80 and 100 neurons. The comparison between them returns similar conclusions as with the two hidden layers DNNs, there is not a correlation between number of neurons and accuracy in the results. In this case the network with three layers and $3x(40)$ neurons each layer shows the best results and lower error under noisy conditions (0dB). Also, as in the previous case, this is not conclusive since the results are very similar between the five networks.

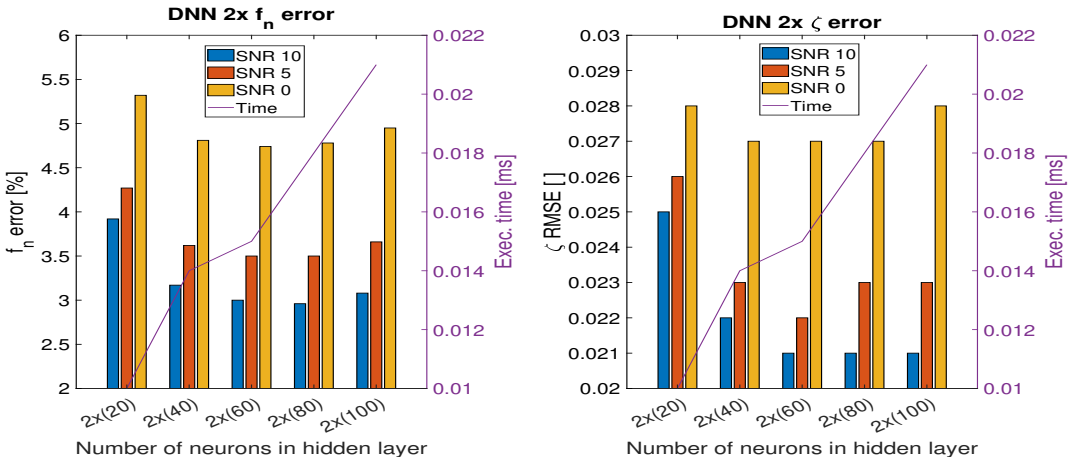

FIGURE 3.12: Plot depicting the estimated natural frequency average relative error in percentage [%] and the Root Mean Square Error (RMSE) in absolute value, comparing DNN networks with 2 layers and composed of different number of neurons on each layer. The secondary "y" axis plots the execution time required for each network in [ms]. The networks were trained with 0dB, 5dB and 10dB SNR data, removing the worst 10% estimations on the validation dataset.

SNR	DNN 3x(20)	DNN 3x(40)	DNN 3x(60)	DNN 3x(80)	DNN 3x(100)
			Avg. Err. f_n		
10dB	3.38 %	2.94 %	2.84 %	2.74 %	2.78 %
5dB	3.76 %	3.40 %	3.40 %	3.31 %	3.41 %
0dB	4.81 %	4.56 %	4.68 %	4.64 %	4.80 %
			RMSE ζ		
10dB	0.022	0.020	0.020	0.020	0.020
5dB	0.024	0.022	0.022	0.022	0.023
0dB	0.027	0.026	0.027	0.027	0.028
			Time/set		
	0.009 ms	0.017 ms	0.022 ms	0.025 ms	0.031 ms

TABLE 3.5: Summary table of DNN trained networks with three hidden layers and one output layer. Each column indicates the type of network (DNN) and the quantity of neurons in each hidden layer.

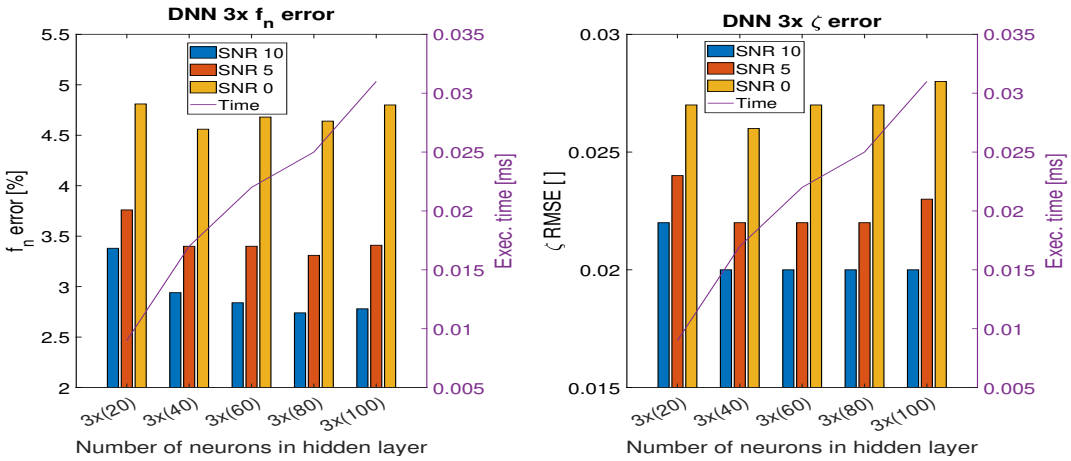

FIGURE 3.13: Plot depicting the estimated natural frequency average relative error in percentage [%] and the Root Mean Square Error (RMSE) in absolute value, comparing DNN networks with 3 layers and composed of different number of neurons on each layer. The secondary "y" axis plots the execution time required for each network in [ms]. The networks were trained with 0dB, 5dB and 10dB SNR data, removing the worst 10% estimations on the validation data.

The analysis and conclusion of the low variability in the results between different networks, might be a consequence of the training process. Notice that even with 100.000 datasets for each level of noise, the training population is relatively small, and there is expected to be some variability in the training process, which might impact in the results shown here, although it also might be a consequence of underfitting with the higher neurons networks or overfitting with the lower number networks. It is complicated to say with such small number of datasets.

Comparing the results between tables 3.4 and 3.5, globally speaking there is a slight improvement in the employment of an extra hidden layer for DNNs. In all the networks explored, the extension of one extra layer resulted in a clear improvement in all the trained networks. In this case, comparing the best candidates from both network types, the 3x(40) network performs better in frequency and damping than the MLP x100 and the DNN 2x(60). However the time is slightly (2ms) higher in the case of the 3x(40) than the 2x(60).

3.7.4 Convolutional Neural Network training process and results

Before describing the structure of the convolutional network employed in this application, we need to describe the structure of the input matrices.

The data recorded is a time series, and in order to convert it into a 2D matrix we need to perform the following preprocessing operations:

1. Define a list of projection unitary imaginary vectors. These vectors will be defined by a real and imaginary part, and will be used to obtain redundant information from each frequency datapoint. In this application 14 unitary vectors (plus the real part and the imaginary part, in total 16 vectors) will be defined, equally spread around the 2π circumference.

2. Cut the original time series signal to 5 seconds samples, or zero-pad until 5 seconds of signal are reached.

3. Calculate the DFT of the time series. A list of vectors (real and imaginary parts for each point) will be obtained for each time series (now frequency values).

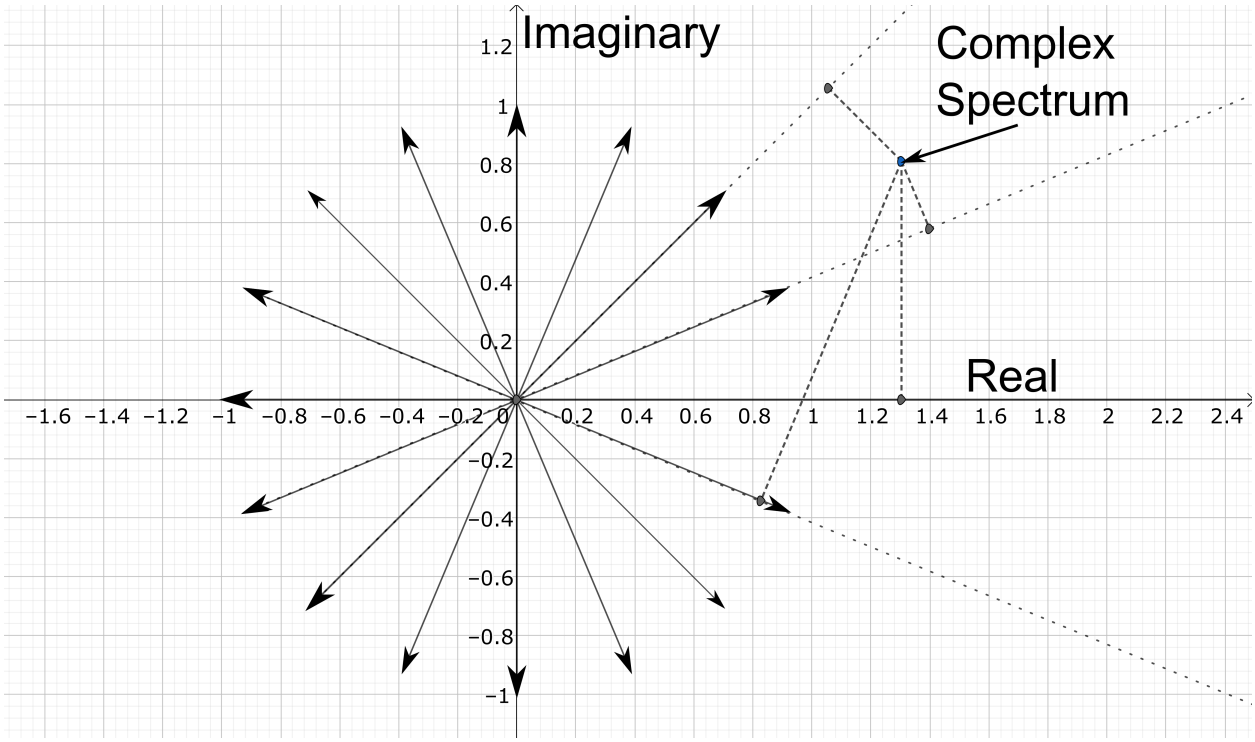

FIGURE 3.14: Construction of the data matrix to feed the CNN. Once the time series dataset is transformed into a frequency spectrum (real and imaginary parts), each dataset of the CNN feed matrix will distribute the frequencies in columns and the projection of each frequency value on different determined vectors in rows.

4. Select the first 70 datapoints. We need to limit the inputs to only the relevant frequencies. In this case approximately 14Hz. These 70 datapoints will constitute the columns of the input matrix.

5. Project each frequency vector on each unitary vector defined in step 1 above. The projection values will be used as redundant information, and the 18 projection values will constitute the rows of the input matrix. Figure 3.14 shows a description of the intent of this step.

Even though the information incorporated into the input matrix is redundant (can be interpreted as a zero padding to reach more resolution in frequency), it is convenient to obtain a 2D matrix and hence feed the CNN.

The structure of the CNNs employed in this application is based on a multi-step process for each convolutional layer, and the architecture is described as follows (and depicted in figure 3.6):

1. Input layer. The inputs are one matrix for each dataset. The dimensions are 70 columns (each frequency) times 16 rows (each redundant projection value).

2. Convolutional block. The convolutional blocks consist of a convolutional layer followed by a series of processes to improve the quality of the operation. In this application two kinds of convolutional networks have been trained, CNNs with 5 hidden convolutional layers (actually convolutional processes) and CNNs with 6 convolutional layers (processes also).

   (a) Convolutional layer. This layer performs the convolution operation on the input matrix. In this application each convolutional layer has the same number of neurons, say 20, 40, 60, 80 and 100 neurons.

SNR	CNN 5x(20)	CNN 5x(40)	CNN 5x(60)	CNN 5x(80)	CNN 5x(100)
			Avg. Err. f_n		
10dB	2.42 %	2.14 %	2.13 %	2.15 %	2.18 %
5dB	3.02 %	2.83 %	2.89 %	2.95 %	2.98 %
0dB	4.28 %	4.18 %	4.31 %	4.39 %	4.41 %
			RMSE ζ		
10dB	0.018	0.016	0.016	0.017	0.017
5dB	0.020	0.020	0.021	0.021	0.021
0dB	0.025	0.025	0.026	0.027	0.027
			Time/set		
	0.822 ms	1.024 ms	1.091 ms	1.126 ms	1.235 ms

TABLE 3.6: Summary table of CNN trained networks with five hidden layers and one output layer. Each column indicates the type of network (CNN) and the quantity of neurons in each hidden layer.

(b) Normalization process. This step normalizes the outputs in order to control the range of the outputs and prevent saturation. A bias is added and a multiplier is applied to the output. These parameters are subjected to training as part of the training process.

(c) Rectification process. The negative values are converted into zero.

(d) Pooling process. The downsampling is made by windows of $2x2$, with a stride also of $2x2$, which means that the windows don't overlap.

3. Connection layer. In this layer, all the outputs from the last convolutional block are connected and reduced to the 4 output parameters described in section 3.7.1. This layer constitutes a classical perceptron layer, employed to gather the outputs from the convolutional layers and return an output to solve the regression problem.

4. Regression layer. Before returning the raw parameters it is necessary to include a regression layer.

Regarding the analysis of results in both kinds of networks, the results are depicted in tables 3.6 and 3.7, supported by figures 3.15 and 3.16 respectively.

The analysis comparing 5 and 6 layers, shows that the best results were obtained with a 40 neurons network in both configurations. Like in the previous cases, the increased number of neurons doesn't necessarily imply a lower error. However, unlike the DNN case, the difference between 5 and 6 layers is minimum, and even though the improvement under noisy conditions (0dB) is noticeable, all the cases analyzed fall under the same order of error, and it is possible that with a larger training dataset the results are different. Note that the processing time for the 5 hidden layers network is very similar to the 6 hidden layers network. Please take into account that these values are not exact. There is a large variability in processing time after successive calculations of the same network and data, starting with a high calculation time (discarding the first estimation to account for the start up of the cluster processing) and asymptotically oscillating around a stable value (indicated in the tables). The most reasonable reason for that is that the workstation employs local cache to calculate the results, and hence the large variability in time after successive runs.

Table 3.6 compares CNNs with 5 hidden layers networks. These outputs throw very similar results among them, although the best estimation comes from the 40 neurons network. The calculation time is very small also compared to the rest of the networks.

Regarding the 6 hidden layers networks, the estimations are also very similar. The times are slightly higher than in the previous case, but also into the same order of magnitude. The best fit is

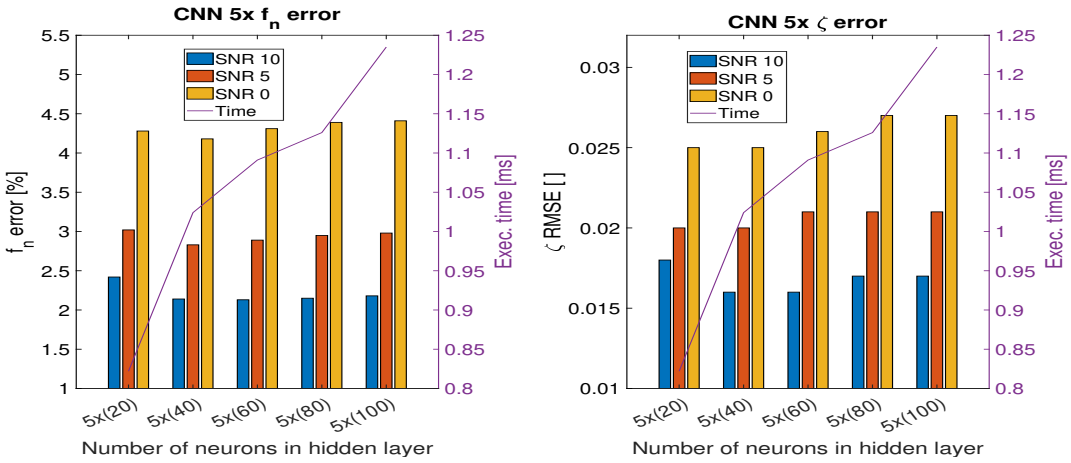

FIGURE 3.15: Plot depicting the estimated natural frequency average relative error in percentage [%] and the Root Mean Square Error (RMSE) in absolute value, comparing CNN networks with 5 layers and composed of different number of neurons on each layer. The secondary "y" axis plots the execution time required for each network in [ms]. The networks were trained with 0dB, 5dB and 10dB SNR data, removing the worst 10% estimations on the validation data.

SNR	CNN 6x(20)	CNN 6x(40)	CNN 6x(60)	CNN 6x(80)	CNN 6x(100)
			Avg. Err. f_n		
10dB	2.29 %	2.12 %	2.06 %	2.06 %	2.06 %
5dB	2.90 %	2.80 %	2.81 %	2.83 %	2.83 %
0dB	4.17 %	4.14 %	4.19 %	4.23 %	4.27 %
			RMSE ζ		
10dB	0.017	0.016	0.016	0.016	0.017
5dB	0.020	0.019	0.020	0.021	0.021
0dB	0.025	0.024	0.025	0.026	0.026
			Time/set		
	0.831 ms	1.035 ms	1.096 ms	1.284 ms	1.489 ms

TABLE 3.7: Summary table of CNN trained networks with six hidden layers and one output layer. Each column indicates the type of network (CNN) and the quantity of neurons in eacg hidden layer.

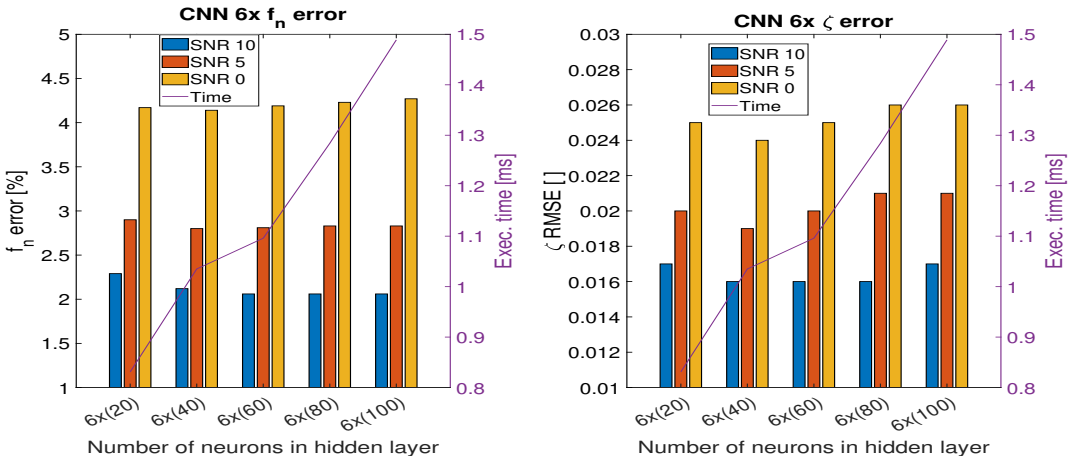

FIGURE 3.16: Plot depicting the estimated natural frequency average relative error in percentage [%] and the Root Mean Square Error (RMSE) in absolute value, comparing CNN networks with 6 layers and composed of different number of neurons on each layer. The secondary "y" axis plots the execution time required for each network in [ms]. The networks were trained with 0dB, 5dB and 10dB SNR data, removing the worst 10% estimations on the validation data.

reached on the 40 neurons network, and also the issue with the 100 neurons network calculation time is present.

As stated above, the comparison between the 5 and 6 hidden layers networks is very similar, and the times also fall under the same order of magnitude. Note however that comparing the CNNs with the DNNs, the processing time is substantially higher in the case of the former. The CNNs take approximately 2 orders of magnitude more time to compute than the DNNs, although still within the real time range for experiments, around 1ms each dataset processing. Comparing the 3x(40) DNN with the CNN with 40 neurons and 6 hidden layers, the results throw a substantial improvement in the estimation in the CNN considering the range of error of all the networks. However note that the estimation time is 2 orders of magnitude higher. Nevertheless, this factor would only need to be considered in case of batch processing a large amount of datasets.

3.8 Comparison of synthetic data analysis results and performance between PRESTO, Laplace Wavelet and Deep Learning techniques

At this stage there is enough information as to compare the three best processing candidates for reducing Sine-Dwell aeroelastic data.

- Laplace Wavelet Matching Pursuit. This technique has been validated with real Flight Test data from the same aircraft that the dataset available for the current thesis. The technique is very similar to PRESTO, with one important difference. The processing considers only one mode at a time. Apart from that, the results are very resilient to noise and guarantee a very good and accurate result when only one mode is participating in the mechanism, disregarding overfitting. The main drawback is that the technique requires a very large dictionary to provide good results which increment largely the processing time, and under certain circumstances it is possible that the technique cannot be used for real time applications.

- PRESTO. This technique is very similar to Laplace wavelet. It is reasonably quick, which may entitle it for real time applications and as said, very similar to Laplace Wavelet, although in this case the two modes are considered at the same time. The advantages are a quick and

SNR	Laplace Wav.	PRESTO	CNN 6x(40)
		Avg. Err. f_n	
10dB	8.75 %	2.84 %	2.12%
5dB	8.78 %	4.37 %	2.80%
0dB	8.82 %	6.82 %	4.14%
		RMSE ζ	
10dB	0.042	0.026	0.016
5dB	0.042	0.038	0.019
0dB	0.043	0.055	0.024
		Time/set	
	60 ms	60 ms	1.0 ms
		Number of runs	
	1	2	1

TABLE 3.8: Results of running Laplace Wavelet, PRESTO and CNN 6x(40) algorithms over synthetic datasets. The metrics are: Time required to estimate each set of data, Natural frequency average error (in percentage) and damping factor Root Mean Square Error.

accurate estimation, improving the results from Laplace on synthetic data, although when only one mode is considered the technique will try to fit two, leading to possible spurious modes or, worst case scenario, to large errors in the estimation due to reaching a solution with two modes instead of one.

- Convolutional Neural Networks. This technique has thrown impressive results on synthetic data. The technique has very good estimation errors and a very good processing time, which entitles it for real time analysis. The only drawback is that it is very dependent on the size of the training dataset as related to the range that it can eventually match, so increasing the range of parameters means increasing the number of training datasets, possibly increasing the size of the network and at last unfailingly increasing the time to train the network or increasing the hardware resources needed.

Table 3.8 and figure 3.17 show the comparison between the three techniques, Laplace Wavelet, PRESTO and a CNN with 6 hidden layers and 40 neurons each layer. The data processed was comprised of 10.000 synthetic datasets of known parameters in the case of PRESTO and Laplace, and the validation dataset (20.000 datasets) in the case of the CNN. The results show a substantial difference between the three techniques, being consistent in the relative ranking between them both in natural frequency and damping estimation. The Laplace Wavelet returned the highest error. In this case the estimation returned an error close to 9% in the frequency estimation consistent for all the SNRs considered and a damping error close to 0.042, also consistent for all the SNRs considered. This indicates that although the technique throws a high error, the estimation is the most robust and resilient to noise. The drawback is that even though the time returned is very similar to the PRESTO estimation, in case of considering a realistic dictionary the time taken would be much longer, in occasions unfit for real time applications. The PRESTO estimation returned a substantially better identification than the Laplace wavelet, with the characteristic that the processing time is accurate under real conditions. In the case of the frequency estimation, the error returned is very sensitive to the SNR, although even in the case of low SNR, the results are still better than the Laplace Wavelet estimation. However, in the case of damping error the results differ. The low SNR case (0dB) returns a substantially worse approximation than the Laplace Wavelet, although in the rest of SNRs the estimation is substantially better. The analysis show that the most effective

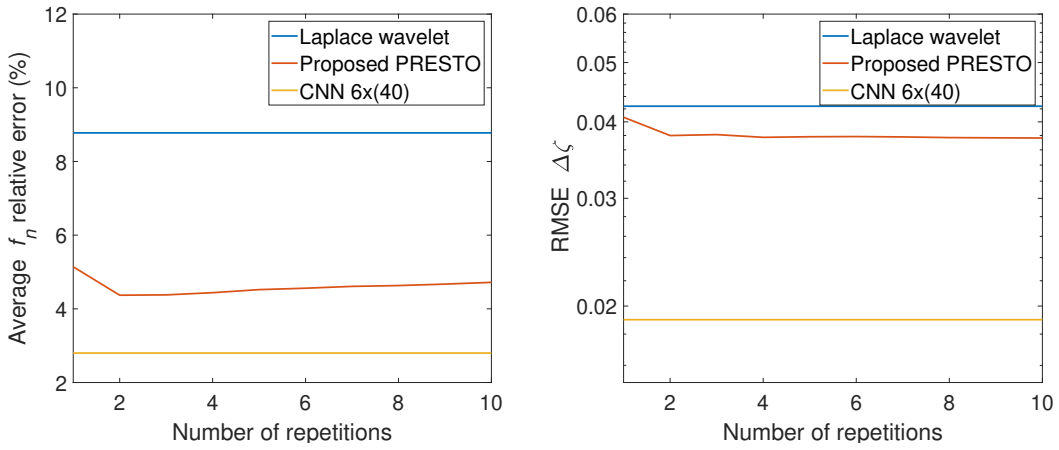

FIGURE 3.17: Plot depicting the estimated natural frequency average relative error in percentage [%] and the Root Mean Square Error (RMSE) in absolute value, comparing Laplace Wavelet, PRESTO and a 6x(40) CNN network. The data compared was generated synthetically by known parameters (10.000 datasets), in the case of the CNN the validation dataset (20.000 datasets) with a SNR of 5dB. In all three cases the 10% worse estimations were removed.

analysis is returned after running two cycles of the PRESTO estimation, as can be seen in figure 3.17. At last, the CNN analyzed returned the best identification parameters compared to the other techniques. The results show a moderate resiliency to noise, better than PRESTO but worse than Laplace, but in all cases substantially better than the previous techniques, both for frequency and damping. The technique is also one order of magnitude faster than the previous ones, and even though the technique has been trained with a reduced dataset (200.000 synthetic signals), the results are very promising.

3.9 Experimental results

This section will show the results from experiments performed on real datasets.

- The real datasets were acquired from real flutter tests flight data from Spanish Air Force F-18 aircraft. The datasets will be processed with only two algorithms, and the data has the following constraints:
  - Algorithms:
    - Laplace Wavelet Matching Pursuit algorithm
    - PRESTO algorithm
    - Convolutional Neural Network 40 neurons per hidden layer x 6 hidden layers
  - Metrics:
    - Linear regression between the real and estimated data (slope and y-intercept)
    - R-Squared coefficient
    - Computational cost (processing time)
  - Conditions:
    - Sampling frequency: $f_s = 85$Hz
    - Length: $t = 5s$

- Range considered:
  - Laplace Wavelet:
    - Natural frequency: $3.0Hz \leq f_n \leq 6.0$Hz
    - Damping factor: $0.03 \leq \zeta \leq 0.20$
    - Phase angle: $0.00 \leq \varphi \leq 2 \cdot \pi$
    - Amplitude: $0.01 \leq a \leq 0.50$
  - CNN:
    - Natural frequency: $3.0\text{Hz} \leq f_n \leq 6.0$Hz
    - Damping factor: $0.03 \leq \zeta \leq 0.20$
    - Phase angle: $0.00 \leq \varphi \leq 2 \cdot \pi$
    - Amplitude: $0.01 \leq a \leq 0.50$

The objective is to compare the three techniques between each other, considering the accuracy of the fit between the real and estimated signals. Note that the Laplace Wavelet and the CNN have a limited dictionary (a limited training range in the case of the CNN) due to limitations to the HW available for reducing data. This will produce a bias in the results, since a larger range or training boundaries might improve the results, and therefore the comparison here cannot be considered conclusive.

Section 3.8 provided a means of comparing the accuracy of the different estimation techniques. From these techniques, it was decided to select three different techniques, Laplace Wavelet Matching Pursuit, PRESTO and a Convolutional Neural Network of 40 neurons per hidden layer and 6 hidden layers to validate against real Flutter Flight Test data.

The reconstruction of the signals for Laplace Wavelet Matching Pursuit and PRESTO were performed from the estimated parameters. The techniques returned all the parameters required to reconstruct the signal (but for the noise of course). However in the case of the Convolutional Neural Network it was not possible to reconstruct the signal from the parameters only, since the amplitudes and phases were not estimated for the reasons described in section 3.7.1. Instead, the signals were reconstructed following a Matching Pursuit procedure to estimate the phases and amplitudes, with the results of natural frequencies and dampings from the CNN results.

3.9.1 Data acquisition

The data were acquired from real Flutter Flight Tests performed on Spanish Air Force F-18A/B. The aircraft incorporates extensometers in different parts of the wing, say root, hinge (mid cord) and wingtip, both in left and right hand sides, as described in figure 3.18. The extensometers appear as red circles on the wing, and in those positions both bending and torsion extensometers are placed. The disposition of those extensometers is so in order to provide a good measure of the vibrational data of the wing, in order to replicate the deformation and vibration characteristics.

The excitation was provided through the Flight Control Excitation Unit (FECU). This element is a Programmable Controller that injects vibrational signals into the flight controls. Once a given program is selected in the FECU, the flaperons start to vibrate according to the programmed pattern. In our case, the signals of interest were Sine Dwells, short duration (4 seconds) vibrations at a given frequency, as described in section 2.7.1. The data is extracted immediately after the excitation stops. The decay signal is analyzed in order to estimate the frequency and damping of the natural modes involved in a given flight condition. The data are sent by telemetry to the Control Room, where a team of Engineers monitors and directs the flight in real time, commanding the pilot to proceed to the next test point or stop. In case that a dangerous situation is inferred or reached, the Test Director commands the pilot to stop the test by pulling the control stick and cutting the engine power, in order to gain altitude and reduce airspeed (reduce the dynamic pressure on the wing) to reach safe flight conditions.

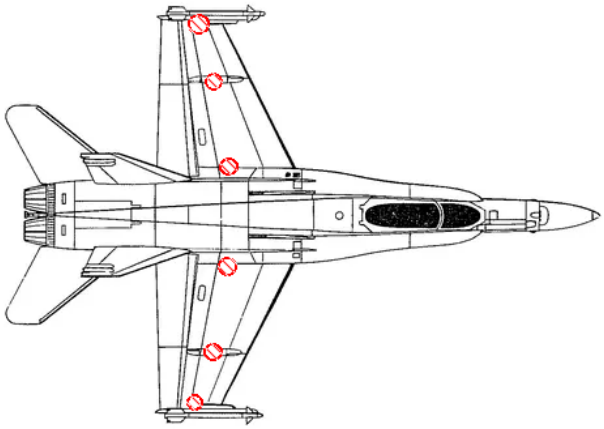

FIGURE 3.18: Disposition of extensometers in the Spanish Air Force F-18A/B employed to perform flutter tests

In case of emergency it is possible to jettison the stores and return to a baseline F-18 configuration, with already known flight envelope. It is necessary to indicate that the inclusion of underwing stores will never increase the flight envelope of the aircraft relative to the baseline configuration. However at this stage of the integration the jettison of the stores has not been validated (not even tested) yet, and therefore it is necessary to stress that this is a last failsafe emergency resource, since the jettison of the stores into an unknown envelope might result in an impact of the stores with the own jet. For this reason, this procedure must be only considered when the integrity of the jet or the life of the pilot is compromised beyond any doubt.

The test was performed with the most critical configurations of the selected stores, and the stop criterion was selected to match a low damping ratio as estimated by the Test Director. It is necessary to remark that during the test campaign, the Test Director didn't have available any real time estimation capability, and therefore the data were analyzed manually by logarithmic decrements, as described by Ewins, 2000, during postprocessing. During the tests, the Test Director and Test Conductors had available tables of decay time on the signals for the frequencies of interest. In particular the Test Team was expecting the signals to reach half of the maximum amplitude in a given number of seconds. Since the expected natural frequency is known (or at least close to a known frequency, since the excitation phase would excite that frequency), the damping ratio was assumed to be 0.03 as defined by JSSG-2006, 1998 and MIL-A-8870C, 1993 and the ratio of amplitudes is defined to be 0.5, it is possible to create a table of expected frequencies from the excitation frequencies and time of decay. The Test Team would expect the excitation stop signal and count mentally the number of seconds until the amplitude reaches half of the maximum amplitude. If it is below the expected value it is safe to continue the test. However, if the decay time is longer (or even close to) the expected time, it is mandatory to stop the test.

The data were acquired at a sampling frequency of 85Hz, and the data selected for processing was 4 seconds long. In the case of shorter signals, the remaining data points were zero padded.

There was a total of 640 datasets, considering 10 extensometers and 8 different excitation runs for each test point (8 test points). Two of the extensometers, the ones located in the right wingtip, were dead and therefore were dismissed. From this point of view, it is expected that only 1/8 to 3/8 of the signals could return good data, since those are the test runs close to the expected natural frequencies. This will impact this analysis expecting only as much as between $80 - 240$ good data estimations, since those will be the points that can theoretically match our model pattern. From those points it is also necessary to remove bad data, like turbulences, pilot involuntary inputs, etc.

Linear regression equation		$y = Mx + N$		
		Laplace Wavelet	PRESTO	CNN 6x(40)
M	Upper bound	0.7766	0.9426	0.7988
	Nominal value	0.7724	0.9390	0.7944
	Lower bound	0.7682	0.9354	0.7900
N	Upper bound	-0.0020	-0.0012	-0.0024
	Nominal value	-0.0029	-0.0019	-0.0033
	Lower bound	-0.0038	-0.0027	-0.0043
R^2		0.6860	0.8157	0.6717

TABLE 3.9: Linear regression over sampled data vs. reconstructed data, considering the Laplace Wavelet Matching Pursuit, PRESTO and a Convolutional Neural Network 6x(40).

3.9.2 Analysis of results

Given that currently there is not any validated method to process data, it is necessary to compare the three techniques, the Laplace Wavelet Matching Pursuit, the PRESTO estimation and the CNN 6x(40) among them with real data. However not having any reference makes hard to find any even breaker between all the techniques.

In this case, the original data points were represented against the reconstructed signals from the results of each technique. Afterwards, a regression fit was applied to the datapoints to compare numerically the results of each technique against the others. Also the MAE (Mean Absolute Error) was calculated on the signal reconstructions from both techniques in order to compare them. The MAE was was chosen to select an error metric independent from all the techniques. Laplace Wavelet Matching Pursuit used as fitting function the maximum dot product between both signals (the projection of one signal on the other is maximum), while PRESTO and the CNN employed the minimization of the MSE as the preferred fitting function.

In all cases, CNN, PRESTO and Laplace, the error signals were processed and normalized by the following operations (in order):

- Limit to 4 seconds data series.
  - Zero pad shorter signals.
  - Cut longer signals.
- Normalize the real signals by the maximum amplitude of the signals in absolute value.
- Identify the signals by the appropriate method (PRESTO, Laplace or CNN)
- Reconstruct the synthetic signals.
- Normalize the synthetic signals by the maximum amplitude of the signals in absolute value.
- Where the real signals have an amplitude of exactly zero (forced by zero padding), force the synthetic signals to be zero also. This way there won´t be an introduction of spurious error by the differences in the tails of the signals when the signals are shorter than 4 seconds.
- Normalize the error metric by the number of samples different to zero. This way there won´t be a bias in the error produced by the length of the signals.

Figure 3.19 represents the plots of the real vs. the synthetic data and the regression line. The fit is representative of a very good match of the data comparing the signals reconstruction and the original signals. The closest the slope is to 45 deg the better the match. This can be assessed by the

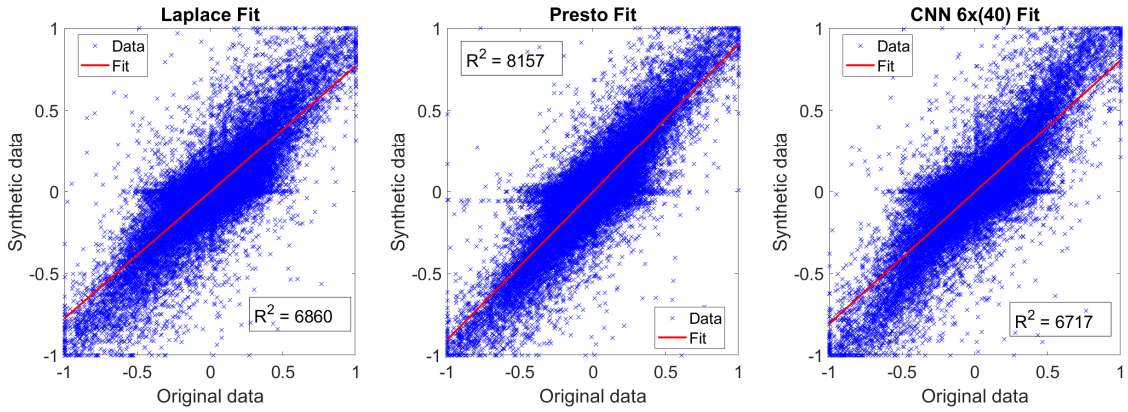

FIGURE 3.19: Data plot between real and synthetic data processed by Laplace Wavelet Matching Pursuit, PRESTO and a Convolutional Neural Network of 6 hidden layers and 40 neurons per layer. The 150 best matching signals out of a complete dataset of 640 were employed. The red line represents the linear regression of the dataplots.

slope of the regression line, described in table 3.9 as M. The closest the slope to 1 the better the fit. Also the dispersion plays an important role. The smaller the dispersion in the data, the better the fit. This can be assessed by the R^2 value. The closest to 1 the smaller the dispersion. At last, the $Y - intercept$ also plays a minor role, indicated by N in table 3.9. A $Y - intercept$ diverging from 0 indicates a bias in the data.

The analysis was performed on 600 real flutter flight test datasets, but only the best 150 were employed for the regression analysis. The amount 150 for the datasets was chosen heuristically following the *Elbow Rule* from figure 3.20. The 150 datasets chosen were different for each estimation depending on the error resulting from each process. For example, the best 3 identifications (lower MSE) for PRESTO were samples 5, 77 and 578, and therefore these three will be the first of the 150 datasets chosen. However for Laplace Wavelet the best 3 identifications were datasets number 48, 353 and 467, and therefore in the Laplace Wavelet plots and calculations, the first 150 datasets chosen will be these last, and will be the ones that will contribute to the regression and final error.

Figure 3.20 shows a comparison of the error between 600 samples from the full dataset. In this case the MAE error metric was chosen to prevent bias between the different processing techniques, taking into account that the Laplace Wavelet Matching Pursuit employed the dot product as an inverse error metric, while PRESTO and the CNN employed MSE. It can be argued that the MAE might benefit a particular technique before others. The dot product, MSE and MAE error metrics, were all tested to compare the original data with the synthetic reconstructions from the three techniques, and the results are coherent among them, following the same pattern as figure 3.20.

Regarding the results, PRESTO returned a very good estimation (the best of all three indeed), which can be assessed by the slope of the linear fit $M = 0.94$, very close to unity, and the Y-intercept $N = -0.002$, which indicates that the fit is at least symmetric in the fit. On the other hand, the R-squared coefficient is $R^2 = 0.82$. Note that a perfect fit would return a R-squared coefficient of 1, and therefore it is indicative of small dispersion in the data, alas a good estimation.

Comparing the results with the Laplace Wavelet Matching Pursuit, figure 3.19 shows a very good fit also. In this case the results are similar although slightly worse. Notice that in table 3.9, the slope $M = 0.77$ is also very close to unity, although slightly worse than PRESTO, and the Y-intercept $N = -0.003$ also indicates an unbiased solution. At last, the R-squared coefficient shows more dispersion than PRESTO, being a value of $R^2 = 0.69$.These results indicate that the fit is reasonably good, although slightly worse than the PRESTO estimation.

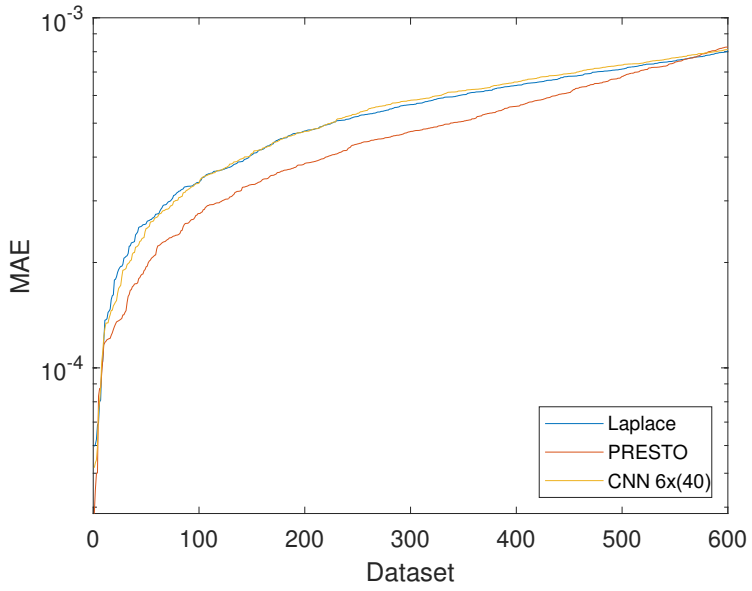

FIGURE 3.20: Mean Absolute Error (MAE) plot between the PRESTO and Laplace Wavelet Matching Pursuit analyzed data. 640 signals were employed to get the error plot.

The last comparison to be performed is the CNN estimation, in this case with 6 hidden layers, 1 input layer and 1 output layer, and 40 neurons on each hidden layer. The results are very similar to Laplace Wavelet. The slope $M = 0.79$ is also very close to unity, with also an unbiased approximation with a Y-intercept of $N = -0.003$. The R-squared value is $R^2 = 0.67$, which indicates also a very good approximation, very similar to Laplace Wavelet. However the important point to remark here is that, even though the results might seem to throw the worse approximation, it is important to remark that the network was not trained to its full capability. Several points to remark:

- The network was trained with a very limited number of datasets.
- The network didn't calculate phase angle or amplitude. These values were calculated afterwards following a Matching Pursuit procedure.
- The network was trained with a very reduced range of frequency and damping parameters, and according to the Frequency Spectrum of the original data (figure 3.23) many signals fall out of the training dataset.

Figures 3.21, 3.22 and 3.23 shows the average spectrum of all the real datasets available in the first figure (duplicated to facilitate the comparison). There are several things to remark:

- There is a strong contribution of low frequency modes (below 2Hz). That contribution will most likely represents the rigid body modes of the aircraft.
- There are two clear modes between 4 and 6 Hz. Those are the main modes of the system whose contribution we need to identify, and are within the training range of the CNN and the Laplace Wavelet.
- There is another mode between 8 and 10Hz. This mode is unaccounted for Laplace Wavelet and CNN.

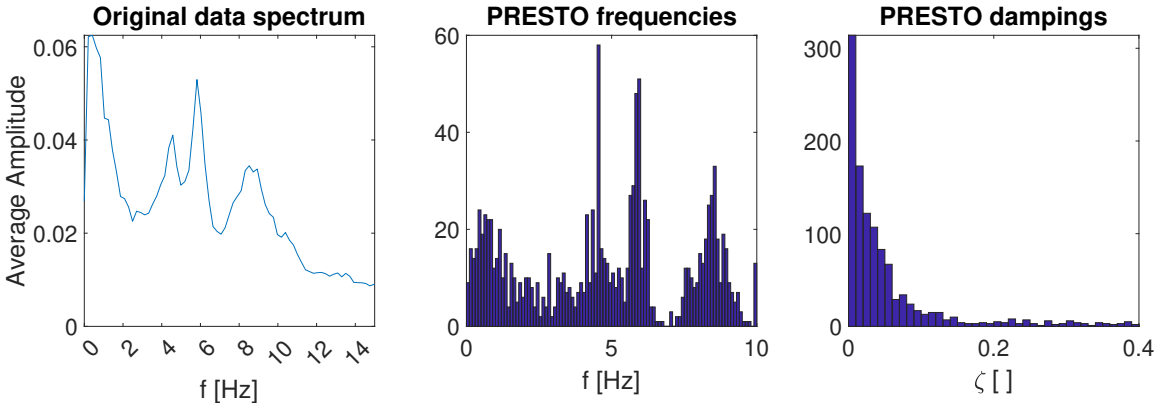

FIGURE 3.21: Average Frequency Spectrum of real data. The first figure shows the frequency spectrum of all the original datasets, the second shows the histogram of frequencies estimated by PRESTO on the original datasets. The third shows the histogram of the dampings estimated by PRESTO on the original datasets.

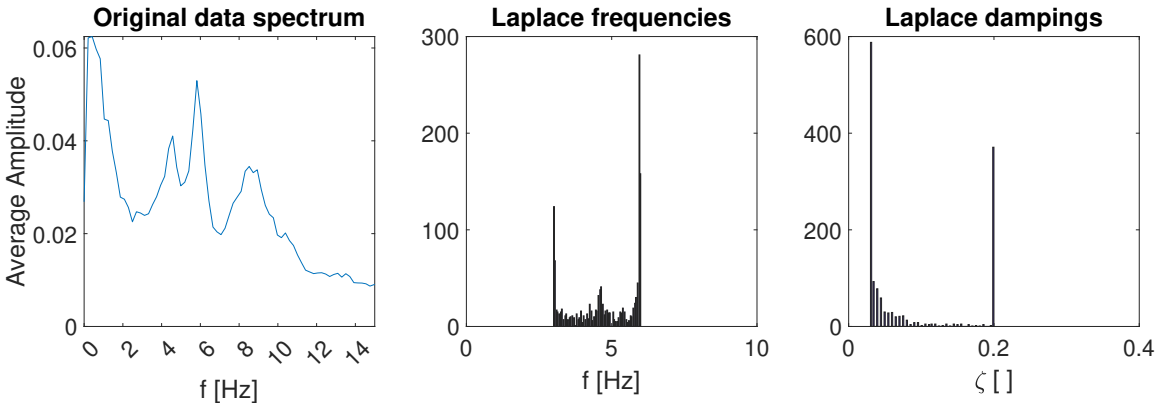

FIGURE 3.22: Average Frequency Spectrum of real data. The first figure shows the frequency spectrum of all the original datasets, the second shows the histogram of frequencies estimated by the Laplace Wavelet on the original datasets. The third shows the histogram of the dampings estimated by the Laplace Wavelet on the original datasets.

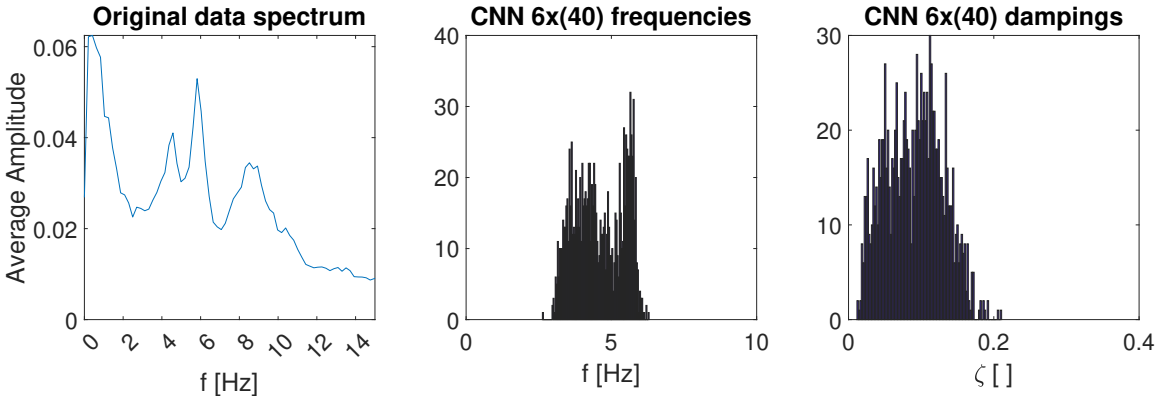

FIGURE 3.23: Average Frequency Spectrum of real data. The first figure shows the frequency spectrum of all the original datasets, the second shows the histogram of frequencies estimated by a CNN 6x(40) on the original datasets. The third shows the histogram of the dampings estimated by a CNN 6x(40) on the original datasets.

Figure 3.21 incorporates the histogram estimation from PRESTO on dampings and natural frequencies. These plots show the number of identified datasets with such parameters. Even though there are modes with a contribution out of the training range of the CNN and the dictionary of the Laplace Wavelet, note that the histogram of dampings show that more than half of the identified dampings fall within the training range and dictionary of the aforementioned techniques ($0.03 \leq \zeta \leq 0.20$), and the same can be said about frequencies ($3.0Hz \leq f_n \leq 6.0Hz$). Note that as indicated in section 3.9.1, only $1/8$ to $3/8$ of the signals will be useful. In fact, only the best $2/8$ of the original signals have been employed. From this perspective, we can have a reasonable level of confidence that the best signals identified fall within those 150 datasets. Figure 3.22 show the histogram of natural frequencies and dampings estimated by the Laplace Wavelet. It is blatant the deficiencies due to the limited dictionary employed, along with the granularity associated to the damping resolution. The frequencies show outliers in the boundaries of the frequencies range, and even though the modes between 4Hz and 5Hz, and between 5Hz and 6Hz seem to have been identified, the boundary outliers take a preponderant position. Something similar happens with the dampings. There are also boundary outliers in the edges of the dictionaries, and also even though the dampings of interest seem to be identified, it is clearly necessary to expand the dictionary to reach successful results. As a side note, Even though the author was aware of this limitation and the implications associated, the limitations in the hardware available imposed a necessity to reduce the dictionary. Also there is a factor to consider in the granularity of the damping identification. This is also a consequence of the limitations on the dictionary size. However, take into account that the outlier in the right edge damping is most likely due to the signals where only one mode is contributing. This can be modeled (and probably the algorithm followed this approach) by increasing enormously the damping factor. A damping above 0.2 will fade out so quickly as to model accurately one single mode in the signal (remember that the model always identifies two different modes). The last plot, figure 3.23, shows the results from a Convolutional Neural Network with 6 hidden layers and 40 neurons per layer. In this case also the limitations from the small training range are blatant. No reports appear above 6Hz or 0.2 damping factor, which obviously implies a necessary failure in the matching of a percentage of the signals. However, as indicated above, the number of signals employed for these histograms include all the datasets, while the scatter plots 3.19 only incorporate the best 150 matches. Note that the network identified a considerable number of signals between 4Hz and 6Hz, with prevalence of the 6Hz modes, which corresponds to reality, even though the assessment is more qualitative than quantitative.

That been said, it is necessary to caveat the results from the current section. Confidence doesn't

mean certainty. Considering the fast processing time for the CNNs and accuracy, it is necessary to reconsider the potential of a CNN with the characteristics of the ones analyzed in this thesis. Even though the PRESTO estimation has demonstrated a superior result in terms of accuracy, the lack of resources to provide a better estimation with the rest of the techniques.

Chapter 4

Conclusions and future lines of work

4.1 Conclusions of the results

This thesis has intended to present, verify and validate new robust and fast techniques to process Flutter Flight Test data.

To achieve such objective, it can be decomposed in the following areas:

1. Introduction and overview of Aeroelasticity and envelope expansion testing. This section provides an overview of the concept of aeroelasticity, flutter, flight envelope and describes the process to perform an envelope expansion from the technical perspective (1.2).

2. Review of the State of the Art (1.3). This section describes the state of the art related to two different areas:

   - The mathematical basis of aeroelasticity, focusing on the equations modeling the phenomenon and the latest procedures related to testing aeroelastic structures.
   - The latest development related to aeroelastic data processing.

3. Ancillary information related to the thesis

   - Scope and limitations of the thesis (1.4).
   - Description of the challenges of the task (1.5).
   - Hypotheses and assumptions that will support the thesis (1.6).
   - Methodology of investigation (1.7).

4. Derivation of the Flutter equations, considering the basic flutter equation as a second order linear differential equation, and the combination of different forces to construct it (2.1).

   - Inertial forces (2.2).
   - Dissipative forces, focused on damping and different damping models (2.3).
   - Elastic forces (2.4).
   - Aerodynamic equations 2.5). We will decompose this section in two parts:
     - Steady aerodynamics (2.5.1), where a brief introduction to fluid dynamics, and potential flow theory will be introduced. This section will eventually derive the forces (lift) and moments (aerodynamic moment) produced by steady aerodynamic forces, and is necessary to understand the unsteady aerodynamics.
     - Unsteady aerodynamics (2.5.2), where the equations of the forces and moments contributing to the flutter mechanism (unsteady lift for bending and unsteady aerodynamic moment for torsion) will be described.
   - Development of the flutter mechanism from the interaction between the previous forces (2.6).

5. Description of the particularities of the flutter vibration signals (2.7). Here will be discussed the particular problems that are faced when identifying these kind of signals.

6. Development of the investigation (3). This constitutes the main chapter of this thesis, and the following tasks will be carried out:

    - A theoretical landmark for constraining the different techniques and solutions will be described (3.2).
    - Different data processing techniques will be analyzed and verified against synthetic data, and then validated against real flutter flight test data.
        - Description of different data processing techniques(3.3), including classical techniques and deep learning techniques.
        - Verification of those techniques against synthetic data (classical techniques, 3.4, and deep learning techniques, 3.7).
        - Development (3.5) and verification (3.6) of a new robust classical data processing technique, the PRESTO algorithm, based on the experience from the verification of different classical data processing techniques.
        - Comparison and selection of the best three techniques, one classical technique (Laplace Wavelet), one deep learning technique (Convolutional Neural Network with 6 hidden layers and 40 neurons per hidden layer) and the developed technique (PRESTO) (3.8).
        - Validation of the three selected techniques against real flutter flight test data (3.9).

7. Summary, conclusions and future lines of work, the current chapter (4).

The main innovations presented can be listed as follows:

1. Importance of the phase angle in the aeroelastic data identification. It has been demonstrated the dependency between the phase angle and the estimation of frequency and damping in a given aeroelastic flutter signal (3.2.1). The importance of this development resides in the application for the development of the PRESTO technique.

2. Relationship between the Power Spectrum bandwidth and the aeroelastic data identification considering the phase angle. The equations of the bandwidth as a function of the natural frequency f_n, the damping factor ζ and the phase angle φ have been described (3.2.2). Same as above, the importance of this techniques resides in the development of the PRESTO technique.

3. Presentation, verification and validation of the PRESTO estimation for processing Flutter Flight Test data on F-18 legacy aircraft. The PRESTO processing technique has been presented. It has also been verified against synthetic signals and compared to different data processing techniques, and lastly it has been validated with real Flutter Flight test data extracted from the Spanish Air Force F-18A/B aircraft. The PRESTO technique has been also compared to a mainframe state of the art technique, the Laplace Wavelet Matching Pursuit technique, and a Deep Learning technique, a Convolutional Neural Network with 6 hidden layers and 40 neurons per hidden layer (3.5).

4. Training with synthetic aeroelastic data and validation against real Flutter Flight Test data of a Convolutional Neural Network with 6 hidden layers and 40 neurons per hidden layer (3.7). It is important to indicate that the use of Deep Learning techniques for Flutter Data Processing is a novel undocumented procedure. All the studies with Deep Learning applied to aeroelasticity focus on the prediction or assessment of flutter conditions, but not the identification of flutter signals parameters.

5. Validation of the PRESTO, Laplace Wavelet Matching Pursuit and a Convolutional Neural Network with real flutter flight test data and comparison among all three techniques (3.9).

4.2 Conclusions

In this section we will summarize the main conclusions from the thesis, with focus on the comparison between the three techniques.

When comparing PRESTO with the other high end validated processing technique, Laplace Wavelet Matching Pursuit, there are some advantages and disadvantages.

The correlations between real and reconstructed data are very similar in both techniques, although Laplace Wavelet shows a slight higher dispersion, probably due to the causes explained in section 3.5.1, mainly that the Laplace Wavelet Matching Pursuit calculates one mode at a time while PRESTO calculates both modes at the same time. Another factor is the performance of both techniques. Laplace Wavelet Matching Pursuit is described as a greedy technique, and requires extensive computational power to return results when the granularity of the atoms is low and the range of the parameters high. In the examples employed for this thesis, the atoms range was limited to the ones of already known conditions and the granularity was high. This was done to return results comparable to the ones achieved by PRESTO, but in a real scenario a thinner granularity would be required, and hence it would be complicated to get results in real time if such conditions were to be fulfilled. From this perspective, PRESTO allows undoubtedly under any condition for real time estimations, while Laplace Wavelet Matching Pursuit would require a mid size cluster in order to get real time results. The Laplace Wavelet technique shows higher insensitivity to noise than PRESTO and is less prone to overfitting when only one mode is considered. However PRESTO is mode accurate when clearly two modes participate in the vibration mechanism.

As a general conclusion, both techniques are suitable for processing real data. Laplace Wavelet Matching Pursuit is less prone to overfitting when only one mode is considered and also will estimate better signals with high levels of noise However, PRESTO will process better signals with two clear modes and allow for real time processing under any condition of sensitivity.

The other technique, Deep Learning, was successfully employed by training different Multi-Layer perceptrons, Deep Neural Networks and Convolutional Neural Networks. Eventually a Convolutional Neural Network was chosen as the best fit to identify flutter flight test signals, with satisfactory results. Even though this network was not trained with the whole range of frequencies and dampings that comprised the real analysis signals, the results are similar to the ones reached with the other techniques, which entitles the technique as a perfect candidate for a future line of investigation.

4.3 Future lines of work

Several open threads were identified during the effort of this PhD process, which entitle for future lines of work.

- Validation of the PRESTO estimation:

  The PRESTO estimation was validated against real F-18A/B flutter flight test data. However it was not validated against another kind of aircraft data. It will most likely work just as fine, but the statement cannot be made without a previous effort of validation against other platforms.

- Overfitting when only one mode is present:

The PRESTO estimation shows tendency to overfitting when only one mode is present. This tendency needs to be properly addressed, and therefore it would be necessary to incorporate steps in the algorithm to prevent overfitting and return a robust solution. For example, by incorporating a preprocessing algorithm to account for the number of modes present in the signal.

- Time Series tendency to get stuck in local minima:

  The Time Series estimation has a tendency to get stuck in local minima. This tendency has not been identified in PRESTO with the Peak-Algorithm seeding process, but it may not be discarded on a different platform or different sets of data. For this reason it is necessary to improve the robustness of the technique by improving the resilience against local minima issues.

- Convolutional Neural Networks as candidates for flutter data processing

  The CNNs have demonstrated to be a very good candidate for a flutter data processing technique. On top of that, Deep Learning is an unexplored technique in this area of investigation with a great potential. It is a procedure robust against noise and one order of magnitude faster than PRESTO or Laplace Wavelet. There are several areas that can be explored:

  - CNN trained with a different number of layers and neurons. Several were explored for his thesis, but it is possible to expand the investigation to more models.
  - CNN trained with a larger number of samples. The number of training datasets employed was relatively small for the networks trained for this thesis. Also, in case of expanding the number of neurons or layer it is necessary to expand the training and validation dataset.
  - In section 3.9.2 it was identified a secondary mechanism of identification in the comparison of dampings, when comparing the CNN with the PRESTO or Laplace Wavelet techniques. It was not possible to identify the reason behind this secondary mechanism, so it is worth investigating.
  - Validation of the CNN with a dataset different to F-18A/B flutter flight test data. Following the same reasoning as with the PRESTO technique, the CNN was validated against real data from a particular aerial platform. However it would be necessary to validate the technique with different aircraft.
  - Overfitting when only one mode is present. Also as in the PRESTO case, the network needs to be trained with datasets including only one signal. For that task it is possible to include in the training data samples with damping of the secondary mode equal to unity or zero amplitude.
  - CNN model with more output parameters. The CNN employed in this thesis included only 4 different output parameters, natural frequencies of modes 1 and 2 and dampings of modes 1 and 2. As demonstrated in section 3.2, the importance of the phase angle is paramount, and even though there are techniques to return the accurate values of the phase angle and amplitude (as described in this thesis), it is worth training a network that returned all the involved parameters or even more modes, although it is unlikely to get that kind of network trained without the capabilities of a supercomputer.

4.4 List of publications

The present thesis yielded two different published works (one journal publication and one international symposium proceedings) and one unpublished journal paper, under preparation.

The first publication corresponds to an initial heuristic development of the investigation. During that time the effort was focused on the identification of flutter parameters by analyzing the frequency spectrum, and even though the results were promising, the reconstruction of the signal was missing one key factor, the influence of the phase angle. The contribution of Dr. Gil Pita was crucial to unlock the problem and reach satisfactory results.

First publication

Title: *Stochastic approach to flutter data processing and application to real F-18 A / B flight test data*

Authors:

- *Sami Abou-Kebeh LLano*
- *Roberto Gil Pita*
- *Manuel Rosa Zurera*

Book: *Proceedings of the Society of Flight Test Engineers, European Chapter (SFTE-EC)*

- Year: 2015
- City: Seville
- Symposium: 26
- Pages: 24

The second publication compiles the core of the PRESTO technique development, verification with synthetic data, validation with real data and comparison to the Laplace Wavelet Matching Pursuit, along with the mathematical justification for the development of the technique. This paper represents a landmark for the investigation, since the inclusion of the phase angle in the equations yielded extraordinary results, considering that the technique was compared to the Laplace Wavelet Matching Pursuit, technique validated with real sets of data, and generated by F/18A/B flutter flight tests, the same aircraft that the real data available for the author of the present thesis.

Second publication

Title: *Multimodal Estimation of Sine Dwell Vibrational Responses from Aeroelastic Flutter Flight Tests*

Authors:

- *Sami Abou-Kebeh LLano*
- *Roberto Gil Pita*
- *Manuel Rosa Zurera*

Journal: *Aerospace*

- Year: 2021
- Volume: 8
- Issue: 11
- Pages: 325
- ISSN: 2226-4310
- D.O.I.: 10.3390/AEROSPACE8110325

The third paper (under development) focuses on the use of a Convolutional Neural Network to process aeroelastic flutter vibrational data. The use of Machine Learning techniques, in particular Deep Learning, is novel for the described application. Different papers focus on the employment of such techniques to identify the flutter point in real time or predict the upcoming flutter conditions, but up to date no published papers exist related to the identification of the flutter parameters.

It is important to remark the importance of this publication given the potential of the technique. The Convolutional Neural Network investigated yielded very similar results to the previous two techniques, with the consideration that the technique can return results in real time (in the order of tenths of millisecond for each signal analyzed, with a low end workstation), with the potential to increase enormously the Situational Awareness of the Test Director during tests, and hence directly impacting the security and the potential rate of survival of the pilot and aircraft during these tests.

Third publication

Title: *Application of Convolutional Neural Networks to identify Flutter Flight Testing signals parameters*

Authors:

- *Sami Abou-Kebeh LLano*
- *Roberto Gil Pita*
- *Manuel Rosa Zurera*

Journal: *Unpublished work. Under elaboration.*

Appendix A

Generic demonstrations

A.1 Demonstration of the aerodynamic velocity potential

We will start defining the velocity circulation Γ around a closed curve c in a velocity field $\mathbf{v}$ and applying Green's theorem:

$$\Gamma = \oint_c \mathbf{v} \cdot d\mathbf{l} = \int_s (\nabla \times \mathbf{v}) \cdot \mathbf{n}\, d\sigma \tag{A.1}$$

Where $d\mathbf{l}$ is a differential of line element from a closed curve c, $d\sigma$ the differential surface element of the surface s enclosed by the curve c, and $\mathbf{n}$ the normal vector to the surface s, as the as depicted in figure A.2.

In order for the velocity to derive from a Potential function, it is necessary that the vorticity of the velocity (circulation) is zero inside the curve c.

According to Meseguer Ruiz and Sanz Andrés, 2010 we can apply **Bjerknes-Kelvin's theorem**, which states that *if the fluid has negligible viscosity, the inertial forces derive from a potential function and the fluid keeps a barotropy relationship (all those premises can be derived from assumptions 4 and 8), the variation with time of the circulation is zero*:

$$\frac{d\Gamma}{dt} = 0 \tag{A.2}$$

Also consider that according to assumption 6, the vorticity of the velocity is zero upwaters, and hence we can fairly assume that the circulation:

$$\Gamma = 0 \tag{A.3}$$

With these two premises into account, we can infer that equation A.1 equals zero, and hence:

$$\nabla \times \mathbf{v} = 0 \iff \mathbf{v} = \nabla \Phi \tag{A.4}$$

And therefore the velocity field $\mathbf{v}$ derives from a velocity potential field Φ

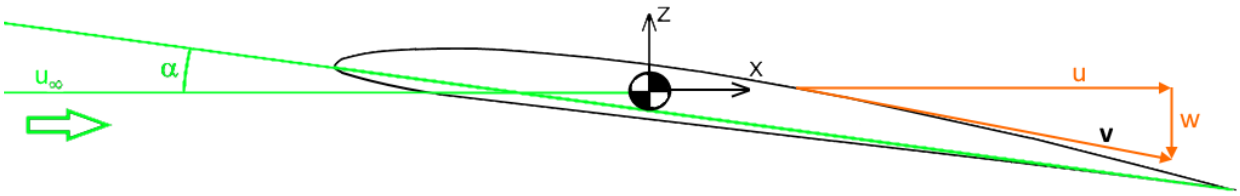

FIGURE A.1: Sign convention and nomenclature

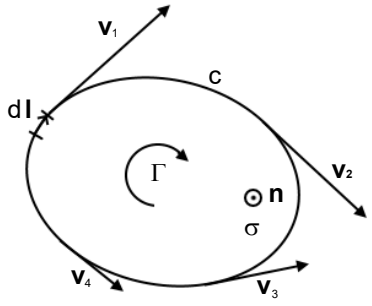

FIGURE A.2: Velocity circulation around a closed curve. Figure 2.2 reproduced here for clarity.

A.2 Calculation of pressure coefficient terms in unsteady aerodynamics from the velocity potential and thermodynamic relationships

In this case we will calculate the pressure coefficient C_p and integrate to know the lift and moment distributions. The pressure coefficient C_p is defined as equation 2.55 (reproduced here for clarity):

$$C_p(\zeta) = \frac{p(\zeta) - p_\infty}{\frac{1}{2}\rho_\infty u_\infty^2} \tag{A.5}$$

Since the undisturbed velocity u_∞, density ρ_∞ and pressure p_∞ are known, the only unknown is the pressure field $p(\zeta)$, which can be calculated from the generalized Bernouilli equation 2.52:

$$\frac{\partial \Phi}{\partial t} + \frac{1}{2}|\nabla \Phi|^2 + \int \frac{dp}{\rho} = C_1(t) \tag{A.6}$$

We need to derive all the terms in Bernouilli's equation. For that we will define the speed of sound a as follows (the demonstration can be found in appendix A.3);

$$a^2 = \gamma \frac{p}{\rho} \tag{A.7}$$

Where a is the local speed of sound, γ the adiabatic expansion coefficient (usually 1.4 for dry air in standard atmosphere) and ρ the air density. The terms on Φ can be derived from equation 2.84:

$$\begin{cases} \frac{\partial \Phi}{\partial t} = \epsilon_1 \frac{\partial \varphi_1}{\partial t} \\ \nabla \Phi = (u_\infty + \epsilon_0 \frac{\partial \varphi_0}{\partial x} + \epsilon_1 \frac{\partial \varphi_1}{\partial x} \ , \ \epsilon_0 \frac{\partial \varphi_1}{\partial z} + \epsilon_1 \frac{\partial \varphi_1}{\partial z}) \\ (\nabla \Phi)^2 = u_\infty^2 + 2u_\infty \frac{\partial \varphi_0}{\partial x}\epsilon_0 + 2u_\infty \frac{\partial \varphi_1}{\partial x}\epsilon_1 \end{cases} \tag{A.8}$$

For the terms related to p and ρ, we need to recall the equation for adiabatic processes:

$$\frac{p}{\rho^\gamma} = \frac{p_\infty}{\rho_\infty^\gamma} \tag{A.9}$$

Where p indicates the air static pressure of a specific fluid particle, ρ indicates the air density of a specific fluid particle, γ is the adiabatic expansion coefficient and the $_\infty$ subindexes indicate undisturbed air conditions.

When combining equations A.7 and A.9 with the term $\int \frac{dp}{\rho}$, yields:

$$\int \frac{dp}{\rho} = \frac{p_\infty}{\rho_\infty}\frac{\gamma}{\gamma-1}\left(\frac{p}{p_\infty}\right)^{\frac{\gamma-1}{\gamma}} = \frac{a_\infty^2}{\gamma-1}\left(\frac{p}{p_\infty}\right)^{\frac{\gamma-1}{\gamma}} \tag{A.10}$$

Substituting equations A.8, A.10 and A.7 into equation 2.52 (particularizing $C_1(t)$ in equation 2.52 to infinite conditions) yields:

$$\begin{aligned}\frac{p}{p_\infty} = \left\{1 + \frac{\gamma-1}{a_\infty^2}[-u_\infty\frac{\partial\varphi_0}{\partial x}\epsilon_0 - (\frac{\partial\varphi_1}{\partial t} + u_\infty\frac{\partial\varphi_1}{\partial x})\epsilon_1]\right\}^{\frac{\gamma}{\gamma-1}} \approx \\ 1 - \frac{\gamma}{a_\infty^2}[u_\infty\frac{\partial\varphi_0}{\partial x}\epsilon_0 + (\frac{\partial\varphi_1}{\partial t} + u_\infty\frac{\partial\varphi_1}{\partial x})\epsilon_1]\end{aligned} \tag{A.11}$$

In equation A.11, to make the approximation we expanded the binomial through the *Newton's generalized binomial theorem* and kept the first two terms, disregarding the terms of order 2 and above.

Now, substituting equation A.11 into the pressure coefficient equation 2.55, yields:

$$\begin{aligned}C_p = \frac{p-p_\infty}{\frac{1}{2}\rho_\infty u_\infty^2} = \frac{\frac{p-p_\infty}{p_\infty}}{\frac{\frac{1}{2}\rho_\infty u_\infty^2}{p_\infty}} = \frac{\frac{p-p_\infty}{p_\infty}}{\frac{1}{2}\gamma\frac{u_\infty^2}{a_\infty^2}} \implies \\ \implies C_p = -\frac{2}{u_\infty^2}[u_\infty\frac{\partial\varphi_0}{\partial x}\epsilon_0 + (\frac{\partial\varphi_1}{\partial t} + u_\infty\frac{\partial\varphi_1}{\partial x})\epsilon_1]\end{aligned} \tag{A.12}$$

Which itself can be decomposed into two different contributions, the stationary ϵ_0 and non stationary ϵ_1:

$$\begin{cases}C_{p,0} = -\frac{2}{u_\infty^2}\frac{\partial\varphi_0}{\partial x}(x,0) \\ C_{p,1} = -\frac{2}{u_\infty^2}[\frac{\partial\varphi_1}{\partial t}(x,0,t) + u_\infty\frac{\partial\varphi_1}{\partial x}(x,0,t)]\end{cases} \tag{A.13}$$

A.3 Velocity of sound demonstration

In this chapter we will demonstrate the equation for the speed of sound in terms of thermodynamic properties. This demonstration is extracted from White, 2016.

In figure A.3 the thermodynamic properties are described with the density ρ, pressure p, temperature T, surface element A and wave speed c. Note that it's accurate to say that in this case the wave speed c (on the left) can be considered the airspeed (U), with a change in airspeed Δc behind the wave.

Now we will apply the continuity equation at both sides of the pressure wave:

$$\rho Ac = (\rho + \Delta\rho)\cdot A\cdot(c - \Delta U) \iff \Delta U = c\cdot\frac{\Delta\rho}{\rho+\Delta\rho} \tag{A.14}$$

Note that the change in density in a sound wave is minimum, and therefore the change in airspeed in equation A.14 is also minimum. However in this equation we have two unknowns, the density increase $\Delta\rho$ and the airspeed in crease ΔU. We need to calculate the density increase, and for that we will apply the conservation of momentum equation at both sides of the wave:

$$pA - (p+\Delta p)A = (\rho Ac)\cdot(c - \Delta U - c) \implies \Delta p = \rho c\Delta U \tag{A.15}$$

Combining equations A.15 and A.14, we get the speed of sound equation:

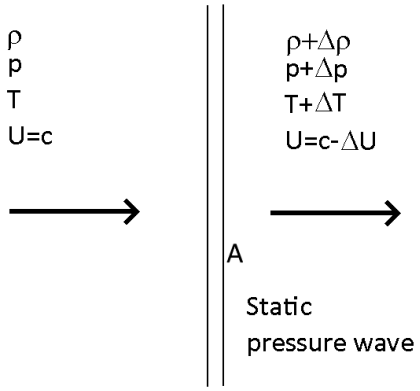

FIGURE A.3: Control volume including a static pressure wave. Note that the control volume is moving with the pressure wave to prevent dependency on time.

$$c^2 = \frac{\Delta p}{\Delta \rho}\left(1 + \frac{\Delta p}{\rho}\right) \tag{A.16}$$

And in the limit, where the density increase is infinitesimal: $\Delta\rho \to o$

$$a^2 = \frac{\partial p}{\partial \rho} \tag{A.17}$$

Where a is the speed of sound.

As a last step, to calculate the derivative it is necessary to model appropriately the thermodynamic model of the sound wave. Take into account that the sound wave is expected to be very weak, and therefore we can state the assumption of the thermodynamic evolution to be isentropic recalling equation A.9 and calculating equation A.17:

$$a^2 = \gamma RT = \gamma \frac{p}{\rho} \tag{A.18}$$

QED

A.4 Calculation of the circulation of the vortices sheet under unsteady aerodynamics

In order to calculate the vortices distribution, first of all we need to calculate the velocity field induced by the vortices on the airfoil sheet and wake models:

$$\frac{\partial \varphi_1}{\partial z}(x, 0, t) = -\frac{1}{2\pi} VP\left[\int_{-B}^{B} \frac{\gamma_a(\zeta, t)}{x - \zeta} d\zeta + \int_{B}^{\infty} \frac{\gamma_w(\zeta, t)}{x - \zeta} d\zeta\right] \tag{A.19}$$

Where VP indicates the Cauchy's principal value of the integral, γ_a represent the contribution of the vortices in the airfoil position and γ_w represent the contribution of the vortices in the wake. Also note that in this case ζ not only represents a mute integration variable, but also the position of the differential vortex element whose contribution we want to calculate.

Introducing equations 2.90 into A.19, we can rewrite the potential derivative in terms of the harmonic functions as defined in 2.90:

$$\overline{\frac{\partial \varphi_1}{\partial z}}(x,0,\omega) = -\frac{1}{2\pi} VP\left[\int_{-B}^{B} \frac{\overline{\gamma_a}(\zeta,\omega)}{x-\zeta} d\zeta + \int_{B}^{\infty} \frac{\overline{\gamma_w}(\zeta,\omega)}{x-\zeta} d\zeta\right] \tag{A.20}$$

Remember from 6 that according to Kelvin's Theorem the contribution along the time of the airfoil circulation and wake vorticity along the length of the wake must be the same. Also, from Kutta condition 2.5.1.9 the vortices created by the circulation are transported to the wake through the trailing edge detached vortex, meaning that the rate of production of vortices in the trailing edge is the same as the vortices along the length of the wake per length unit (of course assuming a stationary regime, the wake is steady):

$$\frac{d\Gamma(t)}{dt} dt - \gamma_w(B,t) dx = 0 \iff \frac{d\Gamma(t)}{dt} - \gamma_w(B,t)\frac{dx}{dt} = 0 \tag{A.21}$$

In equation A.21 the term $\frac{dx}{dt}$ represents the velocity at which the vortices are detached from the trailing edge, meaning the wake velocity. In this case we can assume the wake to be moving at velocity u_∞ (Even though we will not demnsrtate this fact, this is coherent with observation. From an external observer the wake remains static in the atmosphere while the aircraft moves. In a first approximation we will assume that the wake moves with u_∞ relative to the airfoil), therefore we can rewrite equation A.21 as follows:

$$\gamma_w(B,t) = -\frac{1}{u_\infty}\frac{d\Gamma(t)}{dt} \tag{A.22}$$

Now notice that equation A.22 is particularized to the trailing edge B. If we want to to calculate the vortex in the wake at a time t and position ζ, it was detached from the trailing edge at a time t_0:

$$t_0 = t - \frac{\zeta - B}{u_\infty} \tag{A.23}$$

And therefore the equation for a particular time t and position ζ is:

$$\gamma_w(\zeta,t) = -\frac{1}{u_\infty} \left.\frac{d\Gamma(t)}{dt}\right|_{t=t_0} \tag{A.24}$$

We can rewrite this equation considering the harmonic movement as expressed in equations 2.90:

$$\overline{\gamma_w}(\zeta,\omega)e^{i\omega t} = -\frac{1}{u_\infty} i\omega\overline{\Gamma}(\omega) e^{i\omega\left(t-\frac{\zeta-B}{u_\infty}\right)} \iff \overline{\gamma_w}(\zeta,\omega) = -\frac{i\omega\overline{\Gamma}(\omega)}{u_\infty} e^{\frac{i\omega B}{u_\infty}} e^{-\frac{i\omega\zeta}{u_\infty}} \tag{A.25}$$

Equation 2.89 introduced one non-dimensional variable that needs to be employed here, the reduced frequency $k = \frac{\omega B}{u_\infty}$ (we will omit the tilde ˆ here since it is a standard adimensional number), and we will introduce other new non-dimensional variables:

$$\begin{aligned}
\hat{\varphi_z}(\hat{x},0,k) &= \frac{\overline{\varphi_z}(x,0,\omega)}{u_\infty} \\
\hat{\gamma}(\hat{\zeta},k) &= \frac{\overline{\gamma}(\zeta,\omega)}{u_\infty B} \\
\hat{\Gamma}(k) &= \frac{\overline{\Gamma}(\omega)}{u_\infty B^2} \\
\hat{x} = \frac{x}{B},\ \hat{\zeta} &= \frac{\zeta}{B}
\end{aligned} \tag{A.26}$$

The non dimensional potential derivative, vortex distribution, circulation and distances respectively. This way, combining equations A.20 and A.25 can be rewritten in adimensional form with the defined relations as follows:

$$\frac{\partial\hat{\varphi}_1}{\partial z}(\hat{x},0,k) = -\frac{1}{2\pi}VP\left[\int_{-1}^{1}\frac{\hat{\gamma}_a(\hat{\zeta},k)}{\hat{x}-\hat{\zeta}}d\hat{\zeta} - ik\hat{\Gamma}(k)e^{ik}\int_{1}^{\infty}\frac{e^{-ik\hat{\zeta}}}{(\hat{x}-\hat{\zeta})}d\hat{\zeta}\right] \tag{A.27}$$

Equation A.27 has only one unknown, $\hat{\gamma}(\hat{\zeta},k)$. since $\hat{\Gamma}(k) = \int_{-1}^{1}\hat{\gamma}_a(\hat{\zeta},k)d\hat{\zeta}$ and $\frac{\partial\hat{\varphi}_1}{\partial z}$ is related to equations 2.89 by equations 2.87, taking into account that the stream velocity on the airfoil is the same as the airfoil movement as described above.

Recapping so far, expression A.27 relates the velocity potential derived with respect to z (the airfoil vertical component of the velocity, known as a harmonic function) to the airfoil vortices distribution (unknown) in the form of an integral equation.

Now it is necessary to invert equation A.27 to solve $\hat{\gamma}_w$. We will follow Goldstein's method (also Sohngen's method), described by Söhngen, 1939 and applied to this problem by Goldstein and Ward, 1950 without further demonstration:

$$\hat{\gamma}_a(\hat{x},k) = \frac{2}{\pi}\sqrt{\frac{1-\hat{x}}{1+\hat{x}}}VP\left[\int_{-1}^{1}\sqrt{\frac{1+\hat{\zeta}}{1-\hat{\zeta}}}\frac{\frac{\partial\hat{\varphi}_1}{\partial z}(\hat{\zeta},0,k)}{\hat{x}-\hat{\zeta}}d\hat{\zeta} + \frac{ik\hat{\Gamma}(k)e^{ik}}{2}\int_{1}^{\infty}\frac{e^{-ik\hat{\zeta}}}{\hat{x}-\hat{\zeta}}\sqrt{\frac{\hat{\zeta}+1}{\hat{\zeta}-1}}d\hat{\zeta}\right] \tag{A.28}$$

In equation A.28 there is an implicit relationship between $\hat{\gamma}_a$ and $\hat{\Gamma}$. To solve it we will integrate equation A.28 between -1 and 1, meaning between the trailing and the leading edge of the airfoil, to get the global circulation produced by the airfoil as a function of the reduced frequency:

$$\begin{aligned}
&\int_{-1}^{1}\hat{\gamma}_a(\hat{x},k)d\hat{x} = \hat{\Gamma}(k) = \\
&= \frac{2}{\pi}VP\int_{-1}^{1}\sqrt{\frac{1-\hat{x}}{1+\hat{x}}}\int_{-1}^{1}\sqrt{\frac{1+\hat{\zeta}}{1-\hat{\zeta}}}\frac{\frac{\partial\hat{\varphi}_1}{\partial z}(\hat{\zeta},0,k)}{\hat{x}-\hat{\zeta}}d\hat{\zeta}d\hat{x} + \\
&+ \frac{2}{\pi}\frac{ik\hat{\Gamma}(k)e^{ik}}{2}VP\int_{-1}^{1}\sqrt{\frac{1-\hat{x}}{1+\hat{x}}}\int_{1}^{\infty}\frac{e^{-ik\hat{\zeta}}}{\hat{x}-\hat{\zeta}}\sqrt{\frac{\hat{\zeta}+1}{\hat{\zeta}-1}}d\hat{\zeta}d\hat{x}
\end{aligned} \tag{A.29}$$

Equation A.28 can be partially integrated reordering the integration factors, and eventually it leads to:

$$\hat{\Gamma}(k) = -2VP\int_{-1}^{1}\sqrt{\frac{1+\hat{\zeta}}{1-\hat{\zeta}}}\frac{\partial\hat{\varphi}_1}{\partial z}(\hat{\zeta},0,k)d\hat{\zeta} - ik\hat{\Gamma}(k)e^{ik}VP\int_{1}^{\infty}e^{-ik\hat{\zeta}}\left(\sqrt{\frac{\hat{\zeta}+1}{\hat{\zeta}-1}}-1\right)d\hat{\zeta} \tag{A.30}$$

Note that the circulation $\hat{\Gamma}(k)$ can be expressed in terms of the Hankel functions $H_0^{(2)}$ and $H_1^{(2)}$ through the following procedure:

$$\begin{cases}
H_0^{(2)}(k) = \frac{2i}{\pi}\int_{1}^{\infty}\frac{e^{-ik\zeta}}{\sqrt{\zeta^2-1}}d\zeta \\
H_1^{(2)}(k) = \frac{-2i}{\pi k}\int_{1}^{\infty}\frac{e^{-ik\zeta}}{\sqrt{(\zeta^2-1)^3}}d\zeta
\end{cases} \tag{A.31}$$

We can rewrite the second term of the right hand term of equation A.30 as follows:

$$\int_1^\infty e^{-ik\hat{\zeta}}\left(\sqrt{\frac{\hat{\zeta}+1}{\hat{\zeta}-1}}-1\right)d\hat{\zeta} = -\frac{\pi}{2}(H_1^{(2)}(k)+iH_0^{(2)}(k)) - \frac{e^{-ik}}{ik} \tag{A.32}$$

And therefore solving equation A.30 for $\hat{\Gamma}$ yields:

$$\hat{\Gamma} = \frac{2VP\int_{-1}^{1}\sqrt{\frac{1+\hat{\zeta}}{1-\hat{\zeta}}}\frac{\partial\hat{\varphi_1}}{\partial z}(\hat{\zeta},0,k)d\hat{\zeta}}{ike^{ik\frac{\pi}{2}}(H_1^{(2)}(k)+iH_0^{(2)}(k))} \tag{A.33}$$

Now it is possible to substitute equation A.33 into equation A.28, reaching the solution for the vortex distribution along the airfoil:

$$\begin{cases}\hat{\gamma_a}(\hat{x},k) = \frac{2}{\pi}\sqrt{\frac{1-\hat{x}}{1+\hat{x}}}VP\left[\int_{-1}^{1}\sqrt{\frac{1+\hat{\zeta}}{1-\hat{\zeta}}}\frac{\frac{\partial\hat{\varphi_1}}{\partial z}(\hat{\zeta},0,k)}{\hat{x}-\hat{\zeta}}d\hat{\zeta} + \frac{ik\hat{\Gamma}e^{ik}}{2}\int_1^\infty\frac{e^{-ik\hat{\zeta}}}{\hat{x}-\hat{\zeta}}\sqrt{\frac{\hat{\zeta}+1}{\hat{\zeta}-1}}d\hat{\zeta}\right] \\ \hat{\Gamma} = \frac{2VP\int_{-1}^{1}\sqrt{\frac{1+\hat{\zeta}}{1-\hat{\zeta}}}\frac{\partial\hat{\varphi_1}}{\partial z}(\hat{\zeta},0,k)d\hat{\zeta}}{ike^{ik\frac{\pi}{2}}(H_1^{(2)}(k)+iH_0^{(2)}(k))}\end{cases} \tag{A.34}$$

Note that this equation is dependent on the vertical velocity of the airfoil $\frac{\partial\hat{\varphi_1}}{\partial z}$. In equations 2.89 we gave the two characteristic examples of airfoil movement, and hence this parameter is known.

A.5 Calculation of the unsteady pressure coefficient

The pressure coefficient C_p is defined in equation 2.88. We will calculate the difference of pressure coefficient between the upper and lower sides of the airfoil.

$$\Delta C_{p,1}(x,0,t) = C_{p,1}^L(x,0,t) - C_{p,1}^U(x,0,t) \tag{A.35}$$

And from equation 2.88:

$$C_{p,1}(x,0,t) = -\frac{2}{u_\infty^2}[\frac{\partial\varphi_1}{\partial t}(x,0,t) + u_\infty\frac{\partial\varphi_1}{\partial x}(x,0,t)] \tag{A.36}$$

Notice the following relation:

$$\varphi_1 = \overline{\varphi_1}(x,0,\omega)e^{i\omega t} \implies \frac{\partial\varphi_1}{\partial t} = i\omega\overline{\varphi_1}(x,0,\omega)e^{i\omega t} \tag{A.37}$$

Therefore in non-dimensional variables we have:

$$\Delta\hat{C_p}(\hat{x},k) = 2\left\{ik\left[\hat{\varphi_1}(\hat{x},k)^U - \hat{\varphi_1}(\hat{x},k)^L\right] + \frac{\partial\hat{\varphi_1}(\hat{x},k)}{\partial x}^U - \frac{\partial\hat{\varphi_1}(\hat{x},k)}{\partial x}^L\right\} \tag{A.38}$$

However, by the definition of circulation (limited to the airfoil) we have:

$$\hat{\gamma_a}(\hat{x},k) = \frac{\partial\hat{\varphi_1}(\hat{x},k)}{\partial x}^U - \frac{\partial\hat{\varphi_1}(\hat{x},k)}{\partial x}^L \iff$$
$$\int_{-1}^{\hat{x}}\hat{\gamma_a}(\hat{\zeta},k)d\hat{\zeta} = \hat{\varphi_1}^U(\hat{x},k) - \hat{\varphi_1}^L(\hat{x},k) \tag{A.39}$$

Therefore we can write the pressure coefficient difference:

$$\Delta\hat{C}_p(\hat{x},k) = 2\left[\hat{\gamma}_a(\hat{x},k) + ik\int_{-1}^{\hat{x}}\hat{\gamma}_a(\hat{\zeta},k)d\hat{\zeta}\right] \tag{A.40}$$

Now, from the calculated value of γ_a in equation 2.91:

$$\Delta\hat{C}_p(\hat{x},k) = \frac{4}{\pi}VP\int_{-1}^{+1}\frac{\partial\hat{\varphi}_1}{\partial z}(\hat{\zeta},k)\left[\sqrt{\frac{1-\hat{x}}{1+\hat{x}}}\sqrt{\frac{1+\hat{\zeta}}{1-\hat{\zeta}}}\frac{1}{\hat{x}-\hat{\zeta}} - ik\Lambda(\hat{x},\hat{\zeta})\right]d\hat{\zeta} + \\ + \frac{4}{\pi}[1-C(k)]\sqrt{\frac{1-\hat{x}}{1+\hat{x}}}\int_{-1}^{+1}\sqrt{\frac{1+\hat{\zeta}}{1-\hat{\zeta}}}\frac{\partial\hat{\varphi}_1}{\partial z}(\hat{\zeta},k)d\hat{\zeta} \tag{A.41}$$

Where:

$$\Lambda(\hat{x},\hat{\zeta}) = \frac{1}{2}Ln\left[\frac{1-\hat{x}\hat{\zeta}+\sqrt{1-\hat{\zeta}^2}\sqrt{1-\hat{x}^2}}{1-\hat{x}\hat{\zeta}-\sqrt{1-\hat{\zeta}^2}\sqrt{1-\hat{x}^2}}\right] \tag{A.42}$$

And $C(k)$ is known as the Theodorsen function:

$$C(k) = \frac{H_1^{(2)}(k)}{H_1^{(2)}(k)+iH_0^{(2)}(k)} \tag{A.43}$$

A.6 Demonstration of the case $\omega_0 = 0$ in equation 3.11

The derivative 3.10 shows that there is an extremal where $\omega_0 = 0$.
$\omega_0 = 0$ happens if and only if:

$$2(1-2\zeta^2)\beta^2 + 1 = 0 \tag{A.44}$$

This means that depending on the phase there will be a damping ratio over which the extremal of the spectrum is located in zero frequency. To analyze those cases, substituting the definition of β from equation (3.5) in (A.44), yields:

$$\tan(\varphi) = \pm\frac{2(1-2\zeta^2)\sqrt{1-\zeta^2}}{\pm\sqrt{2(1-2\zeta^2)}-\zeta} \tag{A.45}$$

In this case we must consider two different situations:

1. Denominator = 0 $\implies$ $\varphi = \pm\frac{\pi}{2}$

$$\zeta = \sqrt{2(1-2\zeta^2)} => \zeta = \sqrt{\frac{2}{5}} \approx 0.63 \tag{A.46}$$

2. Complex roots
   This particular case involves two equations, $\sqrt{1-\zeta^2}$ and $\sqrt{2\cdot(1-2\zeta^2)}$. The first case simply implies that $\zeta \leq 1$, which is already covered by the condition of subcritical damping. The second case however, is derived as:

$$\sqrt{2\cdot(1-2\zeta^2)} \geq 0 \implies \zeta \leq \sqrt{\frac{1}{2}} \approx 0.71 \tag{A.47}$$

Up to this point we have set an upper limit for damping $\zeta \leq \sqrt{\frac{1}{2}}$, below the required $\zeta \leq 1$ required for the subcritical damping condition.
Now we will demonstrate that this limit is incompatible with the maximal condition. To do that we must calculate the second derivative of the power spectrum expressed in equation (3.6) and particularize for the case $\omega_0 = 0$. The intention is to apply a "reductio ad absurdum" demonstration, on which we will impose $\frac{\partial^2 S_x(\omega)}{\partial \omega^2}\Big|_{\omega=\omega_0=0} < 0$ and try to get to a contradiction:

$$\begin{aligned} &\frac{\partial^2 S_x(\omega)}{\partial \omega^2}\Big|_{\omega=\omega_0=0} = \\ =&2\omega_n^4 \sin^2(\varphi) - \alpha^2 \cdot 2\omega_n^2(4\zeta^2 - 2) < 0 \end{aligned} \tag{A.48}$$

Substituting α from equation (3.3) above and simplifying yields:

$$(\sqrt{1-\zeta^2} + \zeta \tan(\varphi))^2 \cdot (4\zeta^2 - 2) > \tan^2(\varphi) \tag{A.49}$$

In this case we must notice that $(\sqrt{1-\zeta^2} + \zeta \tan(\varphi))^2$ and $\tan^2(\varphi)$ are always positive, so one condition for this to be true is that $4\zeta^2 - 2 > 0$

$$4\zeta^2 - 2 > 0 \implies \zeta > \sqrt{\frac{1}{2}} \approx 0.71 \tag{A.50}$$

According to the condition for the roots to be real expressed in equation (A.47), $\zeta \leq \sqrt{\frac{1}{2}}$, but the condition for the extremal to be a maximum demonstrated in equation (A.50) is $\zeta > \sqrt{\frac{1}{2}}$, which is a contradiction and therefore the extremal must be either a minimum or an inflexion point QED.

Bibliography

Abou-Kebeh LLano, Sami (2013). *Aeroelastic Data Processing Via Matching Pursuit Method*. Universidad de Alcala de Henares, p. 167.

Abou-Kebeh LLano, Sami and Agustin Vaquero Gomez (2016). "Flutter testing at Spanish Air Force". In: *In Proceedings of the 27th symposium of the Society of Flight Test Engineers, European Chapter*. Nuremberg, Germany, p. 18.

Adhikari, Sondipon (2000). "Damping models for structural vibration". PhD thesis. Cambridge University, p. 228. DOI: 10.1006/jsvi.1998.1709.

Almunif, Anas, Lingling Fan, and Zhixin Miao (2020). "A tutorial on data-driven eigenvalue identification: Prony analysis, matrix pencil, and eigensystem realization algorithm". In: *International Transactions on Electrical Energy Systems* 30.4, pp. 1–17. ISSN: 20507038. DOI: 10.1002/2050-7038.12283.

Anderson, John D. (2007). *Fundamentals of aerodynamics*. McGraw Hill, p. 1106. ISBN: 978-0073398105.

Bairstow, L. and A. Fage (1916). "Oscillations of the tail plane and body of an aeroplane in flight". In: *Technical report of the advisory committee for aeronautics* 2.

Barros-Rodriguez, Jose et al. (2015). "Frequency and damping identification in flutter flight testing using singular value decomposition and QR factorization". In: *Proceedings of the Institution of Mechanical Engineers. Part G, journal of aerospace engineering* 229.2, pp. 323–332. ISSN: 20413025. DOI: 10.1177/0954410014533100.

Bishop, Christopher (2021). *Pattern Recognition and Machine Learning*. Springer, pp. 105–144. ISBN: 978-1-4939-3843-8.

Bisplinghoff, R. L., H. Ashley, and Martin Goland (1963). *Principles of Aeroelasticity*. Vol. 30. 1. Dover, p. 160. ISBN: 0486783162. DOI: 10.1115/1.3630096.

Bisplinghoff, Raymond L., Holt Ashley, and Robert L. Halfman (1983). *Aeroelasticity*. Dover Publications. ISBN: 978-0-486-69189-3.

Boyce, William e. and Richard C. Diprima (n.d.). *Ecuaciones diferenciales y problemas con valores ne la frontera*. 4th ed. Willey.

Chajec, Wojciech C. (2018). "Methods of Modern Aircraft Aeroelastic Analyses in the Institute of Aviation". In: *44th International Scientific Congress on Powertrain and Transport Means*. 44th International Scientific Congress on Powertrain and Transport Means. Czestochowa, Poland.

Coleman, Robert P (1940). *NACA TN 751. Damping formulas and experimental values of damping in flutter models*. Tech. rep. Washington: NACA.

Coleman, Thomas F. and Yuying Li (July 1996). "An interior trust region approach for nonlinear minimization subject to bounds". In: *SIAM Journal on Optimization* 6.2, pp. 418–445. ISSN: 10526234. DOI: 10.1137/0806023.

Coll, Francisca (2016). "JFlutter. Real Time Flutter Analysis in Flight Test". In: *SFTE-EC*. SFTE. Nuremberg: SFTE.

Collar, A R (1946). "THE EXPANDING DOMAIN OF AEROELASTICITY". In: *The Royal Aeronautical Society*, pp. 613–636.

Duan, Shiqiang, Hua Zheng, and Junhao Liu (2019). "A Novel Classification Method for Flutter Signals Based on the CNN and STFT". In: DOI: 10.1155/2019/9375437.

Ewins, D J (2000). *"Modal Testing: Theory, Practice and application"*. 2nd ed. Research Studies Press, p. 562. ISBN: 0863802184.

French, A. P. (1971). *Vibrations and waves*. Nelson, p. 316. ISBN: 0177710772.

Freudinger, Lawrence C. (1989). *Flutter Clearance Of The F-18 High-Angle-Of-Attack Research Vehicle With Experimental Wingtip Instrumentation Pods*. Tech. rep. NASA.

Freudinger, Lawrence C., Rick Lind, and Martin J. Brenner (1997). *Correlation Filtering of Modal Dynamics using the Laplace Wavelet*. Tech. rep. NASA Dryden Flight Research Center, pp. 868–877.

Fung, Y. C. (Yuan-cheng) (2008). *An introduction to the theory of aeroelasticity*. Dover Publications, p. 498. ISBN: 0486469360.

García-fogeda, Pablo and Félix Arévalo-Lozano (2015). *Introducción a la Aeroelasticidad*. 1st ed. Garceta. ISBN: 978-8416228379.

Garrick, I E and Wilmer H Reed (1981). "Historical Development of Aircraft Flutter". In: *Journal of Aircraft* 18.11.

Gere, J. (2009). *Timoshenko, Resistencia de Materiales*. Paraninfo, pp. 1–948. ISBN: 8497320654.

Goldstein, S. and G. N. Ward (1950). *The linearised theory of conical fields in supersonic flow, with applications to plane aerofoils*. Vol. 2. 1, pp. 39–84. ISBN: 0001925900000. DOI: 10.1017/s0001925900000330.

Goodfellow, Ian, Yoshua Bengio, and Aaron Courville (2017). *Deep Learning*. 1-2. The MIT Press, p. 800. ISBN: 0262035618.

Goodwin, M. (1997). "Matching pursuit with damped sinusoids". In: *1997 IEEE International Conference on Acoustics, Speech, and Signal Processing*. Vol. 3. IEEE Comput. Soc. Press, pp. 2037–2040. ISBN: 0-8186-7919-0. DOI: 10.1109/ICASSP.1997.599345.

Hidalgo Martinez, Manuel (2010). *Teoria de Vibraciones*. Universidad de Cordoba.

Hill, G. T. R. (1951). "ADVANCES IN AIRCRAFT STRUCTURAL DESIGN". In: *Third Anglo-American Aeronautical Conference*. DOI: 10.1111/j.1559-3584.1952.tb02964.x.

J. Norton, William (1990). *AFFTC-TIH-90-001. Structures Flight Test Handbook*. Tech. rep. November. USAF Test Pilot School.

JSSG-2006 (1998). *Joint Service Specification Guide. Aircraft Structures*. Tech. rep. DoD.

Kijewski, T. and A. Kareem (2000). "Reliability of Random Decrement Technique For Estimates of Structural Damping". In: *8th ASCE Specialty Conference on Probabilistic Mechanics and Structural Reliability* 1, pp. 1–6.

Kiviaho, Jan F., Kevin E. Jacobson, and Graeme J. Kennedy (2019). "Flutter boundary identification from time-domain simulations using the matrix pencil method". In: *AIAA Journal* 57.8, pp. 3639–3640. ISSN: 00011452. DOI: 10.2514/1.J058072.

Lanchester, F. W. (1916). "Torsional vibrations of the tail of an aeroplane". In: *Technical report of the advisory committee for aeronautics* 2.

Li, Kai, Jiaqing Kou, and Weiwei Zhang (2019). "Deep neural network for unsteady aerodynamic and aeroelastic modeling across multiple Mach numbers". In: *Nonlinear Dynamics* 96.3, pp. 2157–2177. ISSN: 1573269X. DOI: 10.1007/s11071-019-04915-9.

Meirovitch, Leonard (2000). "*Fundamentals of Vibrations* ". 1st ed. McGraw-Hill. ISBN: 0070413452.

Meseguer Ruiz, José and Ángel Sanz Andrés (2010). *Aerodinámica Básica*. 2nd. Garceta. ISBN: 978-84-9281-271-4.

MIL-A-8870C (1993). *Military Specification: Airplane Strength and Rigidity. Vibration, Flutter and Divergence*. Tech. rep. March. DoD, p. 52.

MIL-HDBK-516C (2014). *Airworthiness Certification Criteria*. Tech. rep. December. DoD.

MIL-STD-882E (2012). *Department of Defence, Standard Practice - System Safety - (MIL-STD-882E)*. Tech. rep. February 2000. Wright Patterson AFB, Ohio, US: DoD, p. 104.

MSC. Software (1994). *MSC Nastran Version 68 Aeroelastic Analysis User's Guide*. ISBN: 0369111222.

Oppenheim, Alan V and Ronald W Schafer (2009). *Discrete Time Signal Processing*. Pearson, p. 1120. ISBN: 0137549202.

Patel, V. S. et al. (2013). "Energy-sorted Prony analysis for identification of dominant low frequency oscillations". In: *2013 3rd Australian Control Conference, AUCC 2013* 1.December, pp. 85–90. DOI: 10.1109/AUCC.2013.6697252.

Peeters, Bart and Herman Van des Auweraer (2005). "PolyMAX A Revolution in Modal Parameter Estimation". In: *Proceedings of the 1st international Operational Modal Analysis Conference*. Copenhagen, pp. 26–27.

Peeters, Bart et al. (2009). "Modern Solutions for Ground Vibration Testing of Large Aircraft". In: *Sound and vibration*. Vol. 1. ISBN: 9781605600666. DOI: 10.4271/2008-01-2270.

Piazzoli, G (1970). *AGARD-R-573-70 Aeroelastic Test Methods Experimental Techniques*. Tech. rep. AGARD.

Potts, Daniel and Manfred Tasche (2010). "Parameter estimation for exponential sums by approximate Prony method". In: *Signal Processing* 90.5, pp. 1631–1642. ISSN: 01651684. DOI: 10.1016/j.sigpro.2009.11.012.

Rand, Richard H (2005). *Lecture Notes on Nonlinear Vibrations*. Tech. rep. Cornell University, Dept. of Theoretical and Applied Mechanics, p. 111.

Shabana, A. A. (1996). *"Theory of Vibration"*. Mechanical Engineering Series. New York, NY: Springer New York. ISBN: 978-1-4612-8456-7. DOI: 10.1007/978-1-4612-3976-5.

Söhngen, Heinz (Dec. 1939). "Die Lösungen der Integralgleichung und deren Anwendung in der Tragflügeltheorie". In: *Mathematische Zeitschrift 1939 45:1* 45.1, pp. 245–264. ISSN: 1432-1823. DOI: 10.1007/BF01580284.

Soroka, Walter (1949). "Note on the Relations Between Viscous and Structural Damping Coefficients". In: *Journal of the Aeronautical Sciences* 16.7, pp. 409–410. DOI: 10.2514/8.11822.

Stoliker, F.N. (1995). *AGARD-AG-300 vol. 14. Introduction to Flight Test Engineering*. Tech. rep. AGARD, p. 452.

Theodorsen, Theodore (1935). *NACA report 496. General theory of aerodynamic instability and the mechanism of flutter*. Tech. rep. No. 496. NACA, p. 21. DOI: 10.1017/CBO9781107415324.004.

Tian, Wei et al. (2016). "Aeroelastic Tailoring of a Composite Forward-Swept Wing Using a Novel Hybrid Pattern Search Method". In: *Journal of Aerospace Engineering* 29.6, p. 04016056. ISSN: 0893-1321. DOI: 10.1061/(asce)as.1943-5525.0000652.

Wang, Yi Ren and Yi Jyun Wang (2021). "Flutter speed prediction by using deep learning". In: *Advances in Mechanical Engineering* 13.11, pp. 1–15. ISSN: 16878140. DOI: 10.1177/16878140211062275.

Wazwaz, Abdul-Majid (2011). *Linear and Nonlinear Integral Equations*. Springer Berlin Heidelberg. DOI: 10.1007/978-3-642-21449-3.

White, Frank (2016). *Fluid Mechanics*. 8th ed. McGraw Hill. ISBN: 978-9814720175.

Wright, Jan Robert and Jonathan E Edward Cooper (2008). *Introduction to aircraft aeroelasticity and loads*. Johwn Wiley & Sons, p. 488. ISBN: 978-0470-85840-0.

Yuan, Ya-xiang (2000). "A Review of Trust Region Algorithms for Optimization". In: *Iciam*, pp. 271–282.

Zheng, Hua et al. (2021). "Feature Extracted Method for Flutter Test Based on EMD and CNN". In: *International Journal of Aerospace Engineering* 2021, p. 10. DOI: 10.1155/2021/6620368.

Zhu, T. X. (2007). "Detection and characterization of oscillatory transients using matching pursuits with a damped sinusoidal dictionary". In: *IEEE Transactions on Power Delivery* 22.2, pp. 1093–1099. ISSN: 08858977. DOI: 10.1109/TPWRD.2007.893451.

Zimmerman, N. H. and J. T. Weissenburger (1964). "Prediction of Flutter Onset Speed based on fligh subcritical speeds." In: *Journal of Aircraft* 1.4.

Zona Technology (2017). *ZAERO Theoretical Manual V. 9.2*. 3rd ed. Zona Technology INC., p. 323.